UNIVERSITY OF OKLAHOMA

GRADUATE COLLEGE

UNDERSTANDING THE FUNDAMENTAL DRIVE MECHANISMS FOR HUFF-N-PUFF ENHANCED OIL RECOVERY IN TIGHT FORMATIONS

A DISSERTATION

SUBMITTED TO THE GRADUATE FACULTY

in partial fulfillment of the requirements for the

Degree of

DOCTOR OF PHILOSOPHY

By

SON T DANG
Norman, Oklahoma
2019

UNDERSTANDING THE FUNDAMENTAL DRIVE MECHANISMS FOR HUFF-N-PUFF ENAHNCED OIL RECOVERY IN TIGHT FORMATIONS

A DISSERTATION APPROVED FOR THE
MEWBOURNE SCHOOL OF PETROLEUM AND GEOLOGICAL ENGINEERING

BY THE COMMITTEE CONSISTING OF

Dr. Carl H. Sondergeld, Chair

Dr. Chandra S. Rai, Co-chair

Dr. Deepak Devegowda

Dr. Rouzbeh G. Moghanloo

Dr. Adam S. Duerfeldt

Dr. Nicholas Drenzek

To my beloved families, extended family, friends, and colleagues

Acknowledgements

Firstly, I want to thank my advisors, Dr. Carl H. Sondergeld and Dr. Chandra S. Rai, for their tremendous support, patience, guidance and kindness. This work would be impossible without their help. I have worked with them for nearly 10 years (yes, a decade), but I still have a lot to learn from them, not only academically, but also in life. They both have the great combination of academic excellence and kindness. They have brought me the opportunities to work on and challenge myself in different research topics, taught me to think independently, to pursue excellence and to learn to enjoy the journey even if it can be challenging. They convey inspiration of hard work and persistence that I always look up to. Both realized my potential, believed in and encouraged me even when I had so little faith in myself. I am very grateful to have such amazing advisors.

Secondly, I want to thank my family, my grandma, dad, mom, my sister and brother for their supports and unconditional love. Graduate school journey has never been easy, but they have always had faith in me. As an international student, I am also thankful for my extended family here in Oklahoma, who has been cheering for and encouraging me every step of my academic career. You all inspire and keep remind me to look at the bright side, be positive and keep moving forward, even when things are unfavorable. Words cannot express my gratitude for having such a wonderful family, even though we all don't speak a same language. They are the luckiest thing that has ever happened to my life, and they will always be.

I also want to acknowledge Dr. Devegowda, Dr. Moghanloo, Dr. Duerfeldt and Dr. Drenzek for their advices for my research. Additionally, all these works cannot happen without the help from my colleagues, Dr. Tinni, Dr. Curtis, Bruce Spears, Gary Stowe, Abhinav Mittal, Micaela Langevin, and Jeremy Jernigen.

I want to thank all my friends that have always been by my side in the hard moments and shared with me wonderful life and work experiences: Nhung, Huong, Uyen, Yen, and my IC^3 family: Abhinav, Aravinda, Ankita, Jack/John, Juan, Sanchay, Sidi, Byeungju, Aditya, Pritesh, Heyleem, Jing … They have brought a lot of love, laugh (and off course hardship) to my life, making my life in OU enjoyable and memorable. I also appreciate great supports from OU-MPGE with their guidance and generosity: professors, Sonya, Danika, Frances, and multiple Petrobowl team members.

Finally, I thank ENCANA, and Unconventional Shale Consortium members for their technical recommendations and financial supports for all my researches.

Table of Contents

List of Tables

List of Figures

Abstract

Unconventional oil and gas resources have recently become the major source of produced hydrocarbons in the US. The change in the energy landscape follows nearly two decades of technological breakthroughs including horizontal drilling and hydraulic fracturing. These technologies make the production from tight formations economic. The U.S. used to import more than half of its oil, nowadays it has become the world leading crude producer and net imports have dropped to 11% of total consumption, the lowest percentage since 1957 (EIA). While primary production in conventional reservoirs recovers 20-35% of original volume in place, recovery from tight formations is nominally less than 10% (Hoffman and Evan, 2016). The economic value of hydrocarbons (HCs) left behind in tight formations, including shales, is obvious.

Since 2000, many investigations on Enhanced Oil Recovery (EOR) for tight formations have been attempted in both field pilot tests and laboratory studies. Recent successes of EOR programs from different independent companies confirm the potential of additional HC recovery from tight formations with proper stimulation strategies. Unlike conventional reservoirs, the break-even point for every barrel of oil produced from tight formations is relatively high; therefore, to make EOR in unconventional reservoirs possible, it is essential to optimize every step of the stimulation, including the selection of reservoir candidates, suitable EOR methods, and the optimal operational implementation for the selected methods.

In this study, we introduced a workflow to evaluate EOR potential of a play, including three phases: phase 1 – rock and fluid characterization, which provides the foundational knowledge for phase 2 - EOR feasibility screening and phase 3 - fundamental understanding, which helps to define key factors governing the success of EOR huff-n-puff in shales. The EOR potential of a play strongly relies on how much is removable HCs would be left behind in a formation after

primary production. Therefore, *in situ* fluid compositional analyses and rock petrophysical measurement needed to be performed. Critical measurements include SARA (Saturates-Aromatics-Resins-Asphaltenes) analysis, maturity assessment (for fluid understanding); porosity and saturation (for storage mechanism); permeability, pore throat-pore size distribution, and pore-type partitioning (for transport mechanism); SEM imaging (for microstructure observation.)

Phase 2 consists of screening tests allow engineers quickly adjust field parameters, such as injection pressure, volume of injected gases, injectate composition, injection time, or production time. Phase 2 includes two major set of experiments performed simultaneously: one with oil samples, from which minimum miscibility pressure (MMP), oil swelling, and oil-gas diffusivity can be extracted; another set of experiments focus on huff-n-puff tests on crushed rock samples, from which the impact of field parameters can be classified. The results from phase 2 studies highlight the great influences of injection pressure, especially above MMP and injection gas composition on huff-n-puff recovery.

Phase 3 includes carefully designed experiments, to address the fundamental drive mechanisms of huff-n-puff processes in tight formations. It requires the review the relative contribution in mass transport between advection and diffusion for nanoporous media. The major findings highlight the importance of diffusion in the overall mass transport mechanisms, not only for enhanced recovery, but also in primary production. Three major parameters governing the diffusion rate between *in situ* oil and injection gas was identified and includes: mutual oil-gas diffusivity, nano-matrix tortuosity,$(\frac{L_{actual}}{L_{apparent}})^2$ and internal surface area or crack density. While nano-matrix tortuosity is not an adjustable parameter, oil-gas diffusivity can be elevated by proper choice of injection pressure and injectate; similarly, surface area/ crack density can be enhanced by injection pressure.

Obviously, since injection pressure plays a very important role in EOR success, reservoir containment during gas injection needs to be evaluated.

Given the complicated nature of tight reservoir matrix properties and fluid properties, this study also introduced newly designed experiments to measure matrix tortuosity and diffusivity between reservoir fluids and injection gas at high pressure and temperature conditions. Both parameters importantly control the diffusion of injected gases into rock matrix but have not been intensively studied in tight formations.

Introduction

Tight resources are defined as low porosity (less than 10 p.u.)-low permeability (nanodarcy – microdarcy scale) formations, from which natural primary production is minimal and stimulation methods are required to attain economic value. Horizontal drilling and hydraulic fracturing are two major innovations responsible for unlocking tight reservoirs. Although these resources greatly contribute to the U.S. crude production, their productivities tend to decline very fast. In fact, primary (stimulated) recovery factors typically range from 3 to 10 percent of original oil/gas in place (Hoffman and Evan, 2016). Therefore, along with new exploration programs, Enhanced Oil Recovery (EOR) is considered as an essential next step to maintain American energy independence. The following forecast of crude production from different shale plays shows the importance of EOR in maintaining crude output.

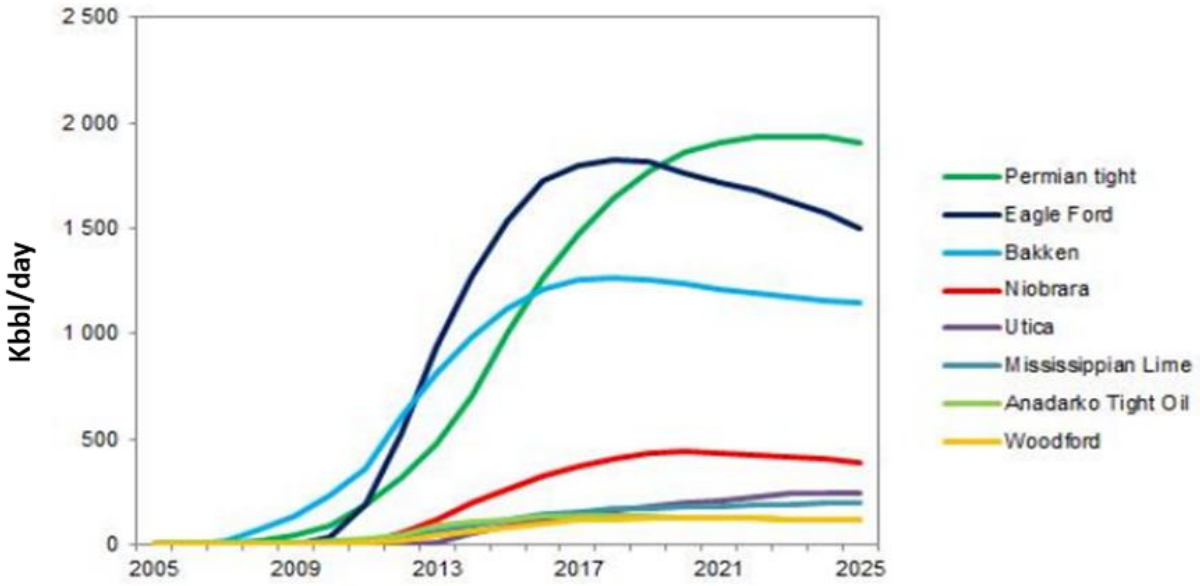

Figure 1. Crude production forecast through years from the top producing tight plays in the U.S (Rystad Energy, 2014). Note since 2017, production rates from overdeveloped fields, such as Eagle Ford and Bakken, start to decline. This makes them potential target for EOR.

Enhanced Oil Recovery (EOR) is not a new concept for conventional reservoirs; these stimulation techniques would be applied to improve formation productivity after primary and secondary recoveries, usually when the recovery is more than 30-35% of Estimated Ultimate Recovery (EUR). However, EOR in unconventional tight formations is a relatively new concept, due not only to technical challenges but also financial constraints. EOR in shale has been investigated in academia (with both experimental and simulation works) since the 1990s, and the earliest EOR pilot test in shale was implemented in 2008 (Wang et al., 2017).

Table 1. Modified summary of EOR pilot tests with different techniques (Wang et al., 2017). The pilots were implemented in the Bakken and Eagle Ford shales. In terms of economic value, only huff-n-puff with natural gas in the Eagle Ford shale has positive results.

No	Operator	Formation	State	Year	Fluid	Type
1	EOG	Bakken	ND, US	2008	CO_2	Huff-n-puff
2	–	Bakken	MT, US	2009	CO_2	Huff-n-puff
3	EOG	Bakken	ND, US	2012	Water	Huff-n-puff
4	EOG	Bakken	ND, US	2012–2013	Water	Flooding
5	EOG	Bakken	ND, US	2014	Natural gas	Flooding
6	Whiting	Bakken	ND, US	2014	CO_2	Huff-n-puff vertical well
7	–	Bakken	MT, US	2014	Water	Flooding
8	Lightstream Resources	Bakken	SK, CA	2011	Natural gas	Flooding
9	Crescent Point Energy	Bakken	SK, CA	2006–2011	Water	Flooding
10	EOG	Eagle Ford	TX, US	2013–2015	Natural gas	Flooding

Both laboratory experiments (Kovscek et al., 2008; USGS, 2013; Wan, 2015; Sheng and Chen, 2014; Sheng, 2015; Hawthorne et al., 2013) and dynamic reservoir simulations (Tovar et al., 2014; Sun et al., 2016; Hawthorne et al., 2013; Yu et al., 2018) showed the potential of EOR in tight formations. However, until 2016, there was no major successful EOR program being publicly reported (Hoffman and Evans, 2016). Most pilot tests have been implemented in Bakken formation with CO_2 or water as injected fluids. Although CO_2 has been demonstrated to be an effective injected fluid, its limited availability is a severe limitation.

The breakthrough in applying EOR in shales comes from successful pilot tests in Eagle Ford with natural gas huff-n-puff experiments. From EOG reports in 2016, the process can recover 30 to 70 percent of original EUR (Hoffman, 2018.) **Figure 2** shows the positive result of a pilot lease with 4 wells being injected. One major component leading to the success of this project is the use of natural gas (more than 90-95% of methane, and 5-10% of C2+), with the injection rate up to 15MMscf/day.

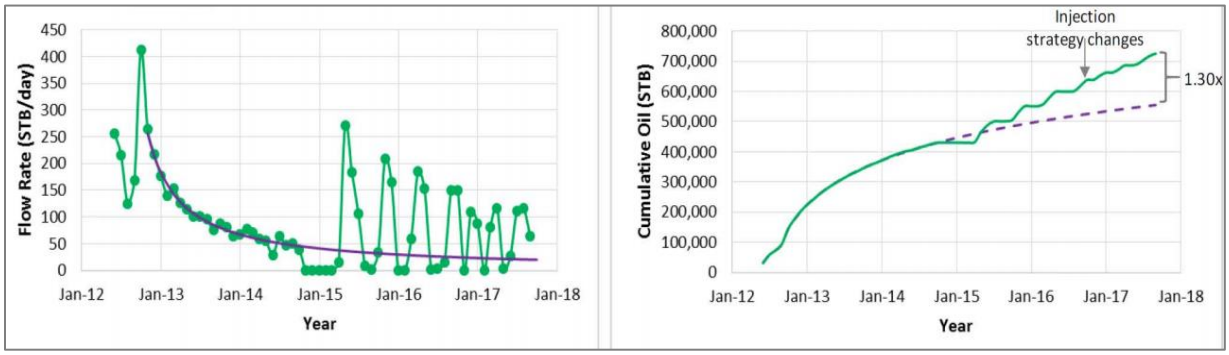

Figure 2. Incremental production and cumulative production for an EOR pilot in the Eagle Ford shale (Hoffman, 2018). The current cumulative production shows 30% improvement, compared to forecasted up-to-date primary production.

With the positive results from field pilot tests in the Eagle Ford formation, the potential of EOR gas injection for tight formations is economically attractive. However, it is also important to mention the unsuccessful EOR programs in Bakken formation, even though laboratory results show positive recoveries in both cases. Moreover, shale operators have financial challenges with long-term investments in EOR, including the cost of compressors, injection gases, and production loss during choking time. Even with the encouraging early results in Eagle Ford, the operational processes require optimization to make EOR in shales economic. Therefore, studying and strategically ranking the prominence of different injection parameters become essential. At the same time, fundamental recovery mechanisms for gas injection in shales need to be investigated

to efficiently select reservoir candidates determine injection-production strategies, forecast the productivity, as well as develop or expand EOR programs. This also helps to minimize the involvement in costly field pilot tests.

In this study, the results for different developing phases of an EOR project will be presented. Phase 1, or the characterization phase, includes basic petrophysical measurements on both rock specimens and fluid samples believed to be important for both primary production and EOR process. Phase 2, or the screening phase, laboratory includes injection experiments with recovery estimation, while changing different controlling parameters. These tests are performed on crushed samples as an accelerated screening process, which allows engineers to quickly classify the prominence of injection parameters on recovery. Phase 3, or fundamental understanding phase, includes newly designed experiments to define the mechanisms of gas injection into nanodarcy rock matrix, and measure key petrophysical parameters governing these mechanisms. The understandings from phase 3, allows upscaling of results or observations from phase 2, which were limited to small sample size. **Figure 3** represents the flow chart of major tests performed, according to three proposed phases of this study.

i.

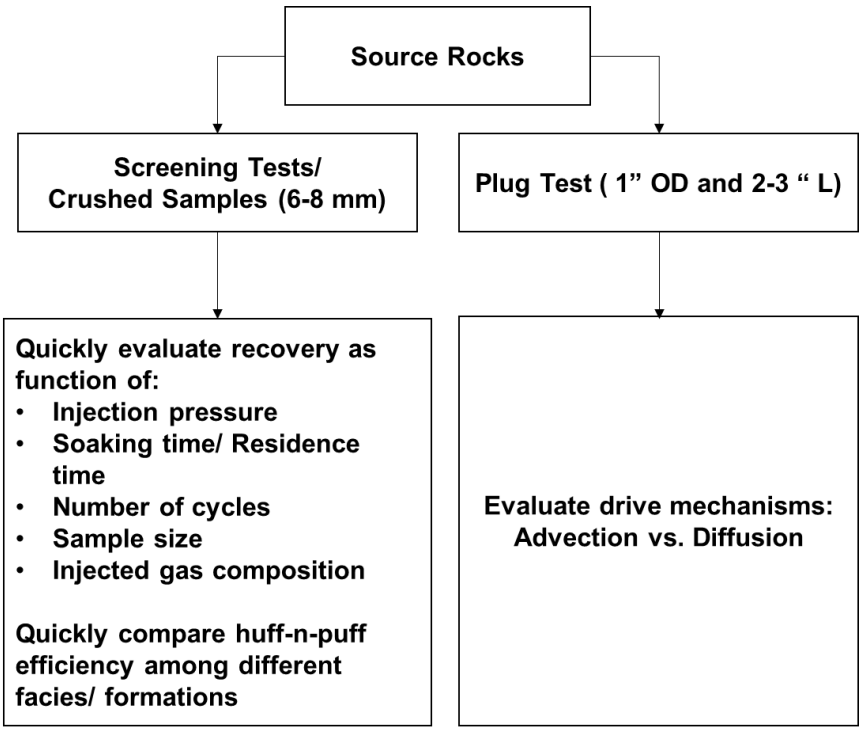

ii.

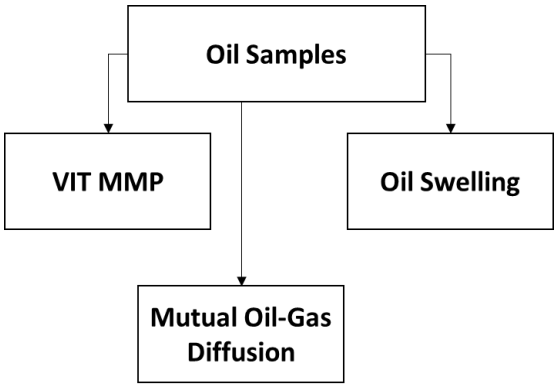

Figure 3. Flowchart for major experiments, which were performed to address different scopes of three development phases proposed for EOR study. Note measurements of both oil samples and rock specimen were simultaneously performed.

i. Measurements on source rock specimen. Preserved samples are preferable.

ii. Measurements on reservoir fluids (separator oils, field gases, and synthetic mixed gases)

I. Fundamental Understanding of Tight Formations

What is "shale"?

Shale is defined as being fine grained rock, a grain size less than 1/256 mm, with porosities less than 10-13% and possessing fissility. Shale's flow characteristics are uniquely tied to nano-scale pore throats, pore size distribution, and pore surface wettability partitioning (water wet versus oil wet components). The existence of solid organic matter (OM) in the shale matrix further complicates flow behavior. However, not all "shale" formations are organic rich. For example, Eagle Ford, Upper and Lower Bakken or Woodford are world-class source rocks, and potentially contain original TOC up to 20 w%, which went through thermal maturation, then generated hydrocarbons; whereas, Middle Bakken, Utica, Collingwood, and Meramec have very little TOC, but are still regarded as tight reservoir rocks. The following figures show the difference in fluid composition within Middle Bakken (reservoir rock), which is sandwiched between Upper and Lower Bakken (source rocks). Differential composition migration has been observed in this example.

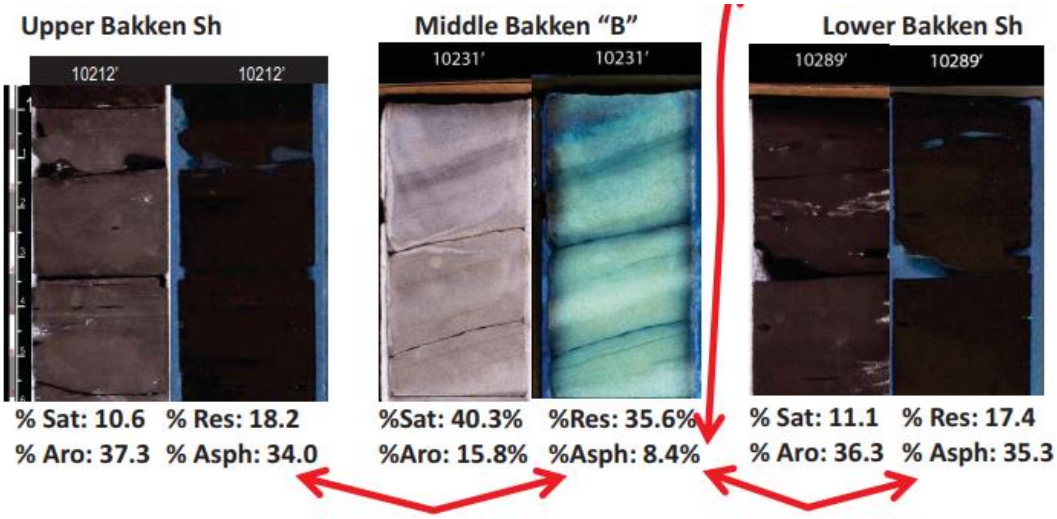

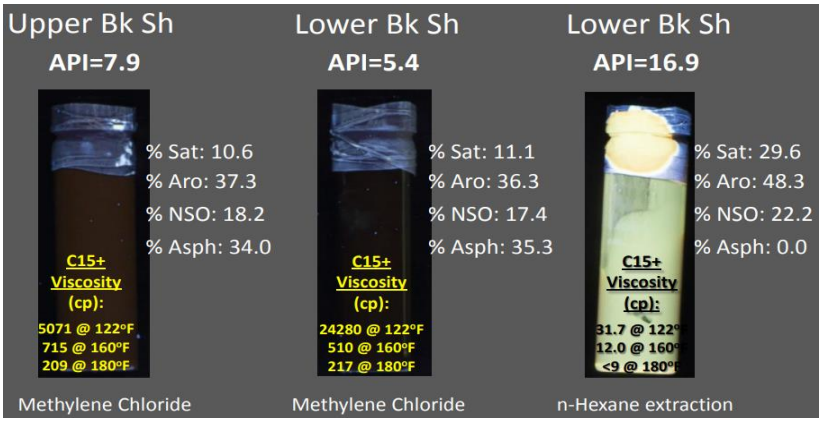

Figure 4. SARA (Saturates-Aromatics-Resins-Asphaltenes) analysis for the extracted oil from Upper-Middle-Lower Bakken, in which Upper & Lower Bakken are source rock layers, containing more highly polar compound than reservoir rock, Middle Bakken (Sonnenfeld and Canter, 2016).

Depending on organic content and its maturity level, *in situ* HCs in shales can be different. Initial Gas-Oil Ratio (GOR) is considered as good indicator of HC wetness, which generally correlates with the formation's thermal maturity. **Figure 5** shows the Eagle Ford production vs. GOR map across the oil prone-condensate prone-gas prone windows, from NW to SE. Fluid viscosity and fluid-rock interaction are critical for shale productivity. Operators observe the poorer production for the slightly less mature windows, mainly because HC viscosity restricts the flow in a tight matrix.

Major pore-throat sizes in tight shale formations are less than 25-30 nm (**Figure 6**, in general, the mercury intrusion pressures for shale samples are greater than 5000 psi). Based on NMR and SEM imaging, there are three different pore types: organic pore (generally assumed to be oil-wet), inorganic pore (generally assumed to be water-wet), and mixed-wet pores (Tinni et al., 2017) (**Figure 7**). Depending on the distributional model of these pore types, relative permeability among gas, oil and water are greatly impacted. In fact, the conventional relative permeability model may not be valid. Based on topography, there are three different pore types: micro-round pores,

microcracks, and meso-cracks (these terminologies are different from IUPAC pore size classification, in which micropores < 2nm, mesopores from 2-50 nm, and macropores > 50 nm.) Cracks in general are far more important to fluid transport in shale than in terms of storage (Walton and McLennan, 2013; Pruess and Narasimhan, 1985). However, determining the origin of cracks in recovered core samples is problematic; one does not know if are they *in situ* or induced? **Figure 6** shows the dependence of pore throat sizes as a function of mineralogy for Eagle Ford samples. Higher clay or lower carbonate content correlate with smaller pore throats. However, in **Figure 8**, there is no observed correlation between plug permeability and mineralogy, which suggests strong interference of cracks in permeability measurement.

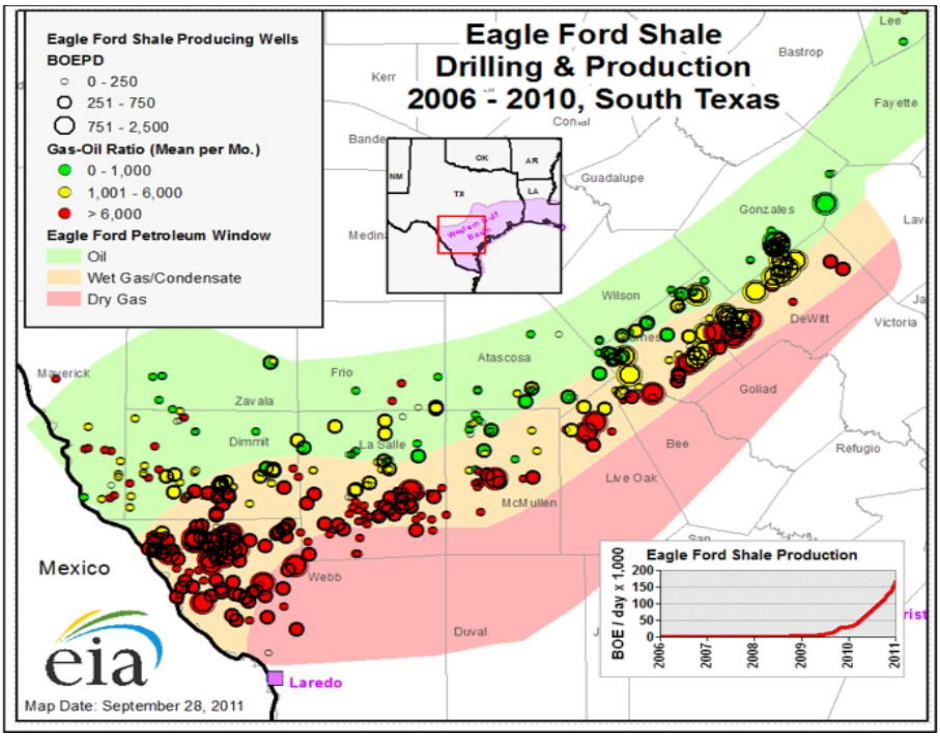

Figure 5. EIA 2010 production bubble map of Eagle Ford shale, corresponding to different maturity windows and different GOR benchmarks (EIA, 2011). Note how the reservoir fluid viscosity (from gas to condensate to oil) impacts the general production.

Cracks are described as low-compliance pore features; therefore, their density, dimension and anisotropy are extremely stress-sensitive. Therefore, shale compressibility and its transport characteristics are strongly governed by geomechanical conditions (**Figure 9**) (Metwally and Sondergeld, 2011). Measured shale permeability decreases with increasing effective stress Walsh (1981); however, the impact of stress on crack surface area has not been intensively investigated.

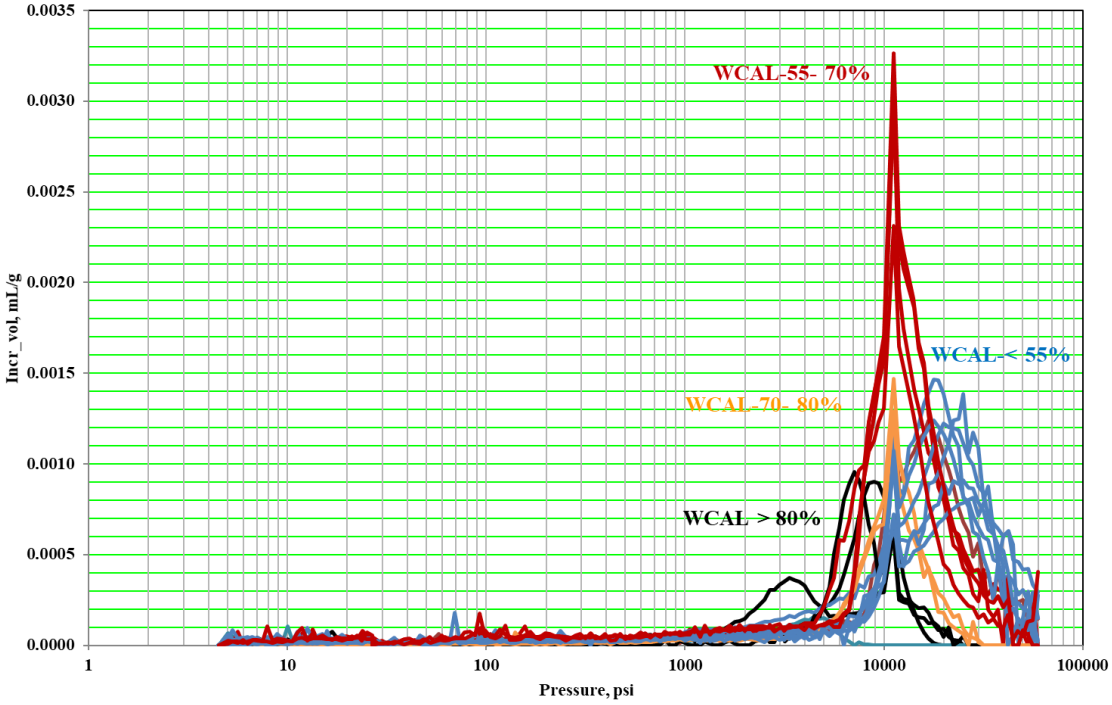

Figure 6. Examples of pore throat size distributions in the Eagle Ford shale, measured by Mercury Injection (MICP). Capillary pressure is inversely proportional to pore throat radius. These samples are categorized into 4 groups of different carbonate concentrations (WCAL). Highest carbonate samples show larger pore-throats, but poor pore connectivity; whereas, lowest carbonate samples (highest clay samples – marl stone) show smaller pore throats (IC^3 Data*).

*IC^3 is Integrated Core Characterization Center, Mewbourne School of Petroleum and geological Engineering, University of Oklahoma

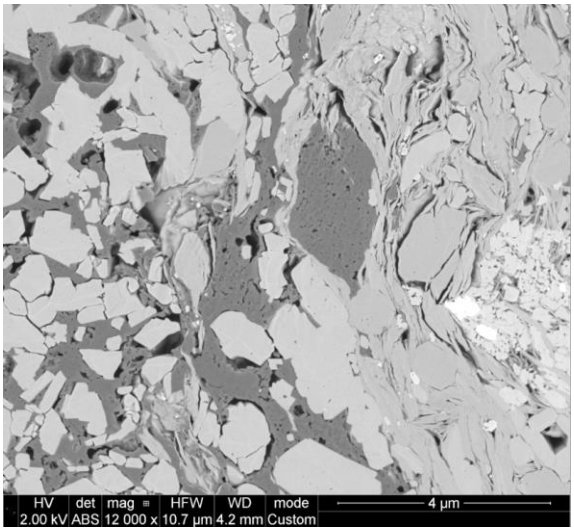

Figure 7. Back-scattered electron SEM image of an Eagle Ford sample within the oil maturity window (courtesy of Dr. Curtis). The bright matter is pyrite, light gray matter is mineral/inorganic matrix, and dark gray matter is solid organic content (kerogen). Pore system includes organic, inorganic and mixed pores.

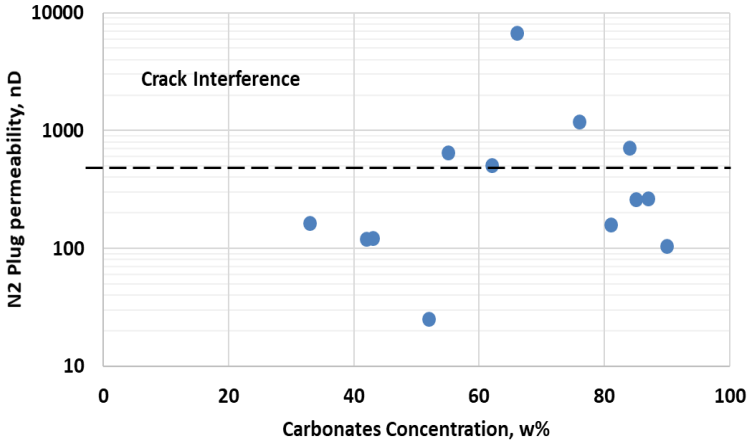

Figure 8. Nitrogen steady-state plug permeability measured for the same set of samples (**Figure 6**) from the Eagle Ford shale (IC^3 Data*). The measurements were done at a pore pressure of 2000 psi and effective pressure of 1500 psi. Samples with permeability higher than 500nd are crack-dominant.

*IC^3 is Integrated Core Characterization Center, Mewbourne School of Petroleum and geological Engineering, University of Oklahoma

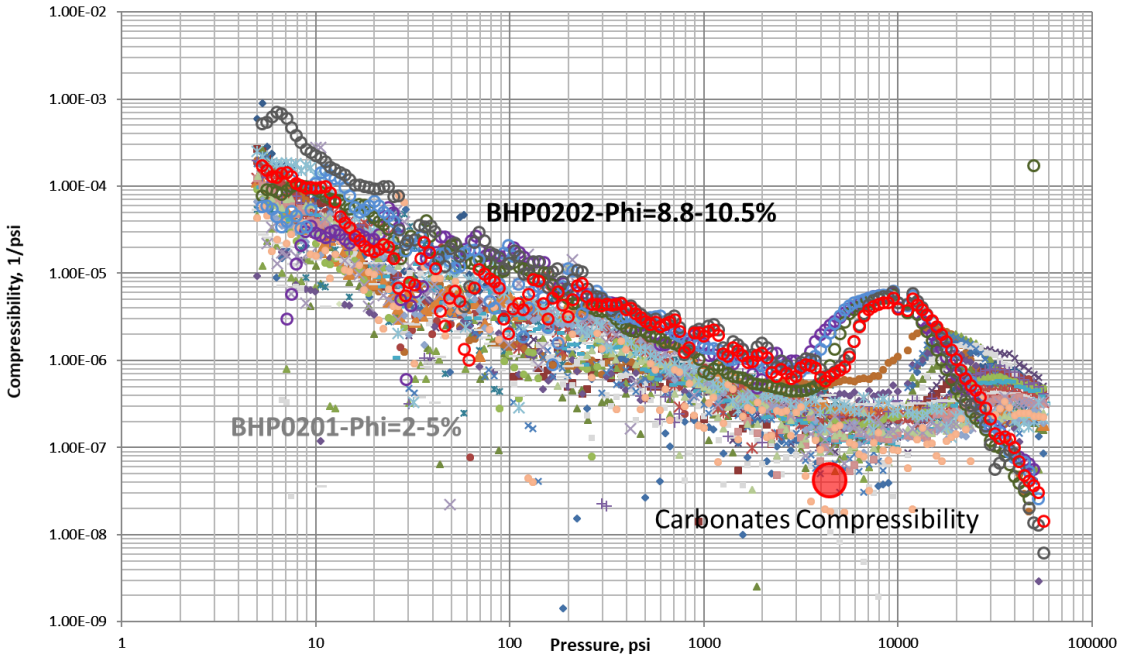

Figure 9. Effective compressibility from MICP data versus hydrostatic pressure (Dang et al., 2017.) These samples are from two different wells in the Eagle Ford, one shows higher compressibility and larger pore throats than another. Note water compressibility in ambient condition is about $3.5*10^{-5}$ psi^{-1}.

For shale/tight formations, mineral, geochemical, geomechanical, storage, transportation, and fluid properties are generally inextricably related; and considering all these factors are the key to a successful shale exploration and development program.

How shale formations are developed and operated?

Due to low permeability and complex connectivity, natural economic primary recovery in unconventional tight resources is nearly impossible. Various stimulation techniques have been applied to enhance flow of HCs into the wellbore; the combination of horizontal drilling, slick-water hydraulic fracturing (HF), and proppant placement have been proven most efficient in stimulating unconventional reservoirs. However, to maximize the EUR, drilling and completion strategies need to be carefully planned. **Figure 10** shows a general HF process scheme. Many

recent studies have shown that by reducing stage spacing and reducing the number of clusters per stage, drainage volume can be optimized (Roussel and Sharma, 2011; Ajisafe et al., 2017; Cao et al., 2017). In the Eagle Ford, the common stage spacing is 200-300ft, and the common cluster spacing within a stage is 25-50ft (Nwabouku, 2012). However, the performance from each stage is usually inconsistent.

The most common diagnostic evaluation survey for HF efficacy is microseismic, in which acoustic attributes are recorded and interpreted to help understand rock failure mechanisms (Maxwell et al., 2011). Despite sophisticated interpretation models, many fundamental questions remain: what kind of acoustic events are recorded? Breakage during HFs, or reactivation of natural fractures? Gale et al., 2007; Das and Zoback, 2011) Does the spatial distribution of the microseismic events, represent the dimension of Stimulated Reservoir Volume (SRV) or the dimension of effective stimulated volume?

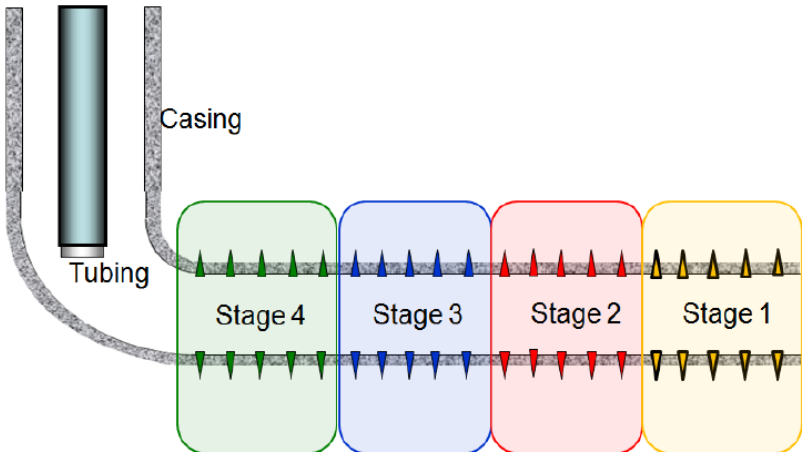

Figure 10. Schematic of typical completion design in shale formation, including horizontal drilling and hydraulic fracture design. Each stage was fractured separately by plug and perforation completion. Spikes are perforations (Du et al., 2011).

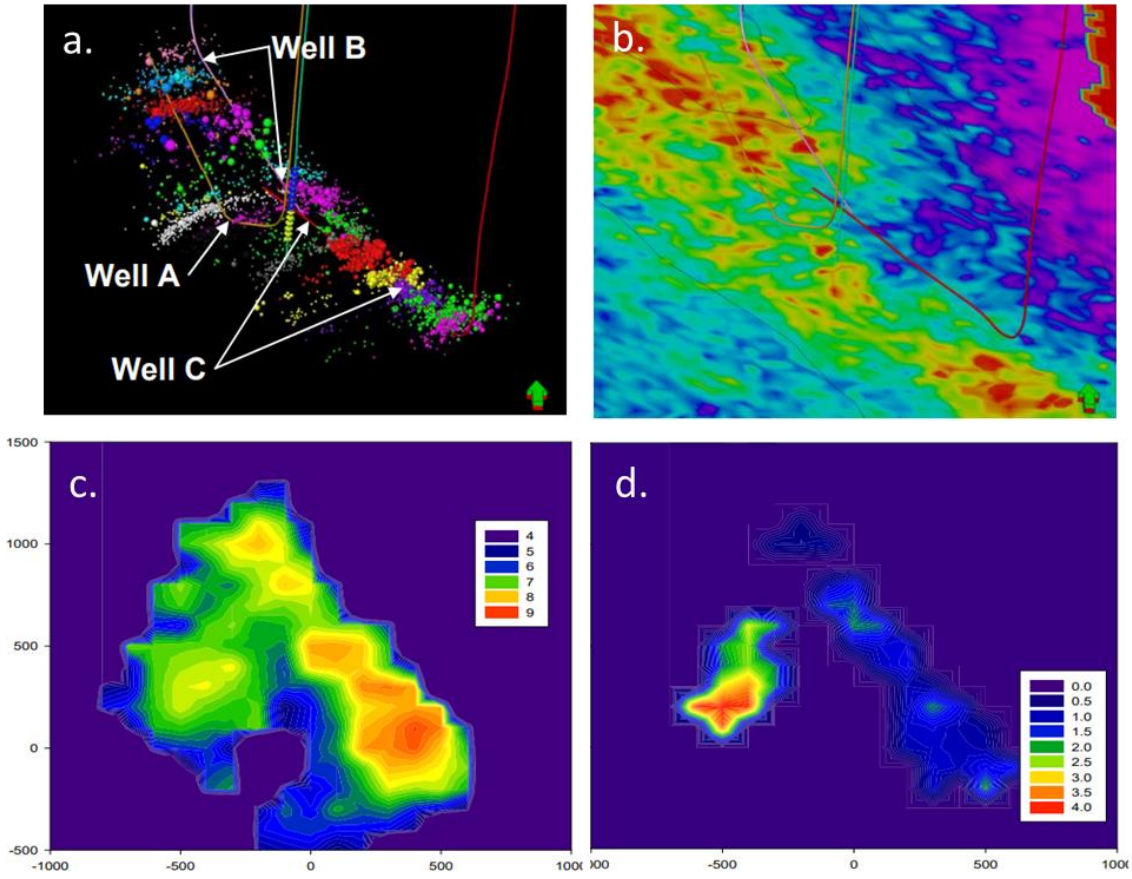

Figure 11. An example of a microseismic survey in the Montney shale (Maxwell et al., 2011). a) Location and magnitude of seismic events for different frac-stages in three wells. b) Heat map of the formation Poisson's ratio (warm color – low value). c) Overlaid seismic moment density. d) Overlaid frequency-magnitude relationship. All evidence supports well C was drilled in the area with high natural fracture density, and mostly HF induced events were from fracture reactivation.

The following plot shows poor correlations between physical count of fracture frequency and indirectly detected fracture frequency from a microseismic survey (Raterman et al., 2017). This highlights that the determination of fracture geometry and density is needed at a scale finer than seismic resolution and remains a challenge.

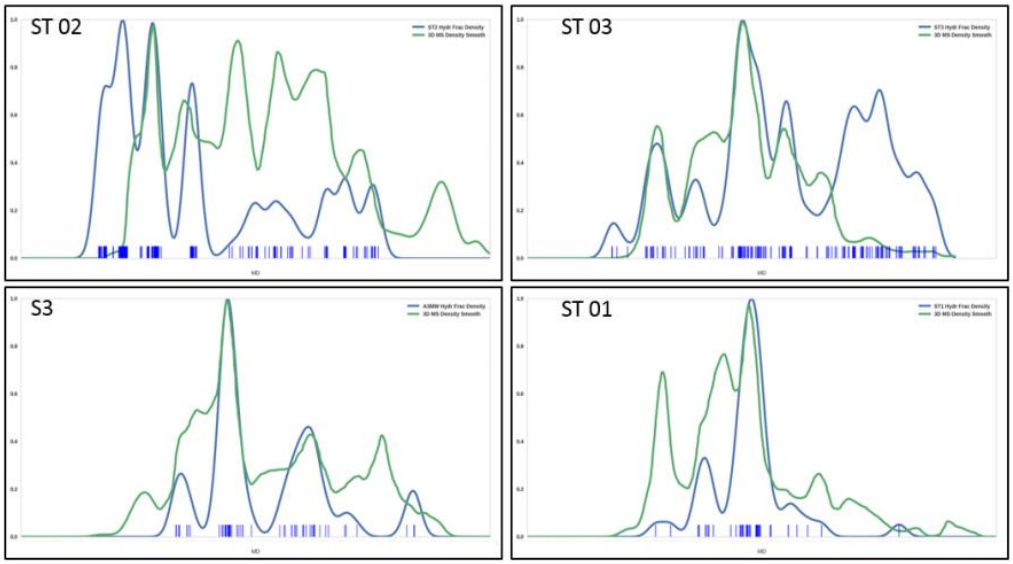

Figure 12. Fracture distribution along four well paths (Raterman et al., 2017). Green curve is distribution of microseismic density. Blue curve is distribution of fracture counts along each wellbore from micro-image log. Cores were also withdrawn along the horizontal wellbores, and fracture density was recounted to confirm the evaluation from image logs.

Figure 13 shows one hydraulic fracture swarm including 22 fractures, observed from both downhole image log and core recovered from a slanted well drilled through SRV of a stimulated parent well. Note how planar the fractures are, and fracture apertures could be resolved in the image logs, which implied they were open from the beginning of reservoir depletion. Depending on their apertures, some fractures are more likely to take proppant than others.

Proppant placement is also a big problem in tight formation completions. Proppants are used to keep the factures open and maintain fracture conductivity during the production. The following figure show two adjacent fractures, one is propped, and another is without proppant. Moreover, recent laboratory studies show even with properly propped fractures, their conductivity can be reduced by up to 90% within a month from the beginning of reservoir depletion (Mittal et al., 2017).

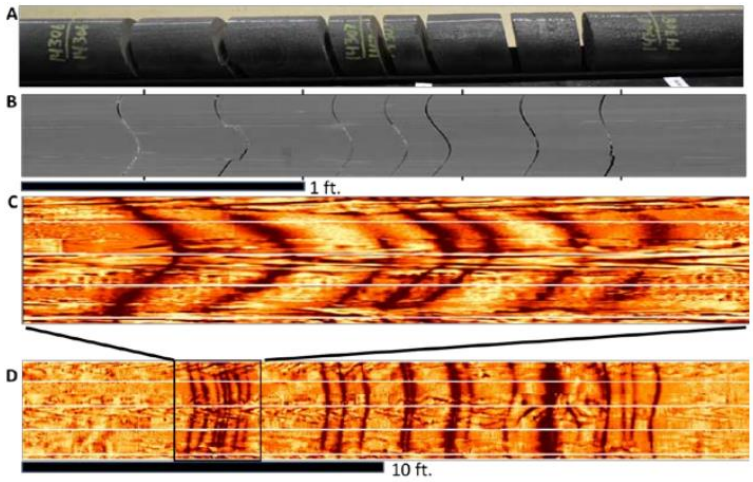

Figure 13. Swarm of fractures within 20ft of core (Raterman et al., 2017.) The same fractures were observed by the image log with different dips; fractures are generally planar.

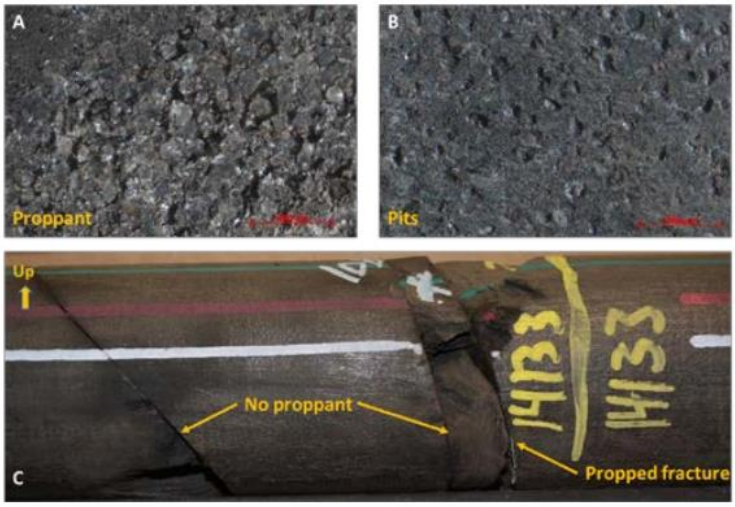

Figure 14. Proppant placement is inconsistent in unconventional reservoir stimulation. Note within adjacent fractures, some fractures were propped, others show no evidence of proppant. Between (A) and (B), engineers observed big difference in proppant concentration. This would impact overall fracture conductivity. (Raterman et al., 2017.)

The completion design does not only govern the productivity of a single well, but also affects cross-well performance, in which multiple wells share a common drainage volume. Cross-well

production is a major type of frac-hit, which can result in positive outcomes, but mostly in a decrease of the whole lease EUR (Anderson et al., 2016).

Production nature of tight formations

As mentioned above, unconventional tight reservoirs cannot be produced without stimulation; therefore, the productivity is governed by both rock properties and SRV properties, reflected in the completion quality. With the monitoring of bottom-hole pressure and produced fluids, production data analysis or Rate Transient Analysis (RTA) during primary production can provide useful information about reservoir properties (Bello, 2009; Qanbari and Clarkson, 2016). In general, different flow regimes are observed, starting first with the depletion in fractured volume (linear flow), then the depletion in rock matrix (radial flow).

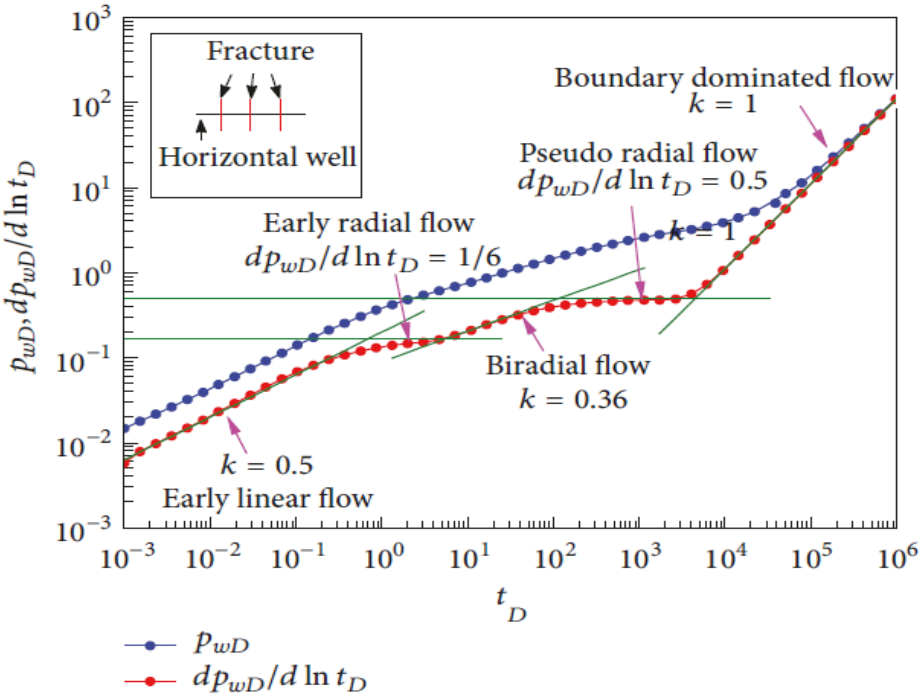

Figure 15. Dimensionless pseudo-pressure and pseudo-pressure derivative versus production time can help to distinguish different flow regimes, with the early domination of linear flows from fracture network (Feng et al., 2014).

Many recent studies focus on production drivers, including completion quality. Yuan et al. (2017) showed the impact of an increase in lateral length on tight rock productivity. For example, average Permian basin horizontal well lateral length increased from 5500ft to 7000ft between 2013-2016 (Curtis and Montalbano, 2017) with average productivity enhancement of 73%. Moreover, bigger completion size (more frac-fluid and more proppant) contributed to the productivity growth. **Figure 16** shows the yearly growth of productivity normalized by 1000ft lateral segment length; this growth resulting from bigger completion size, is independent of lateral length expansion (Curtis and Montalbano, 2017).

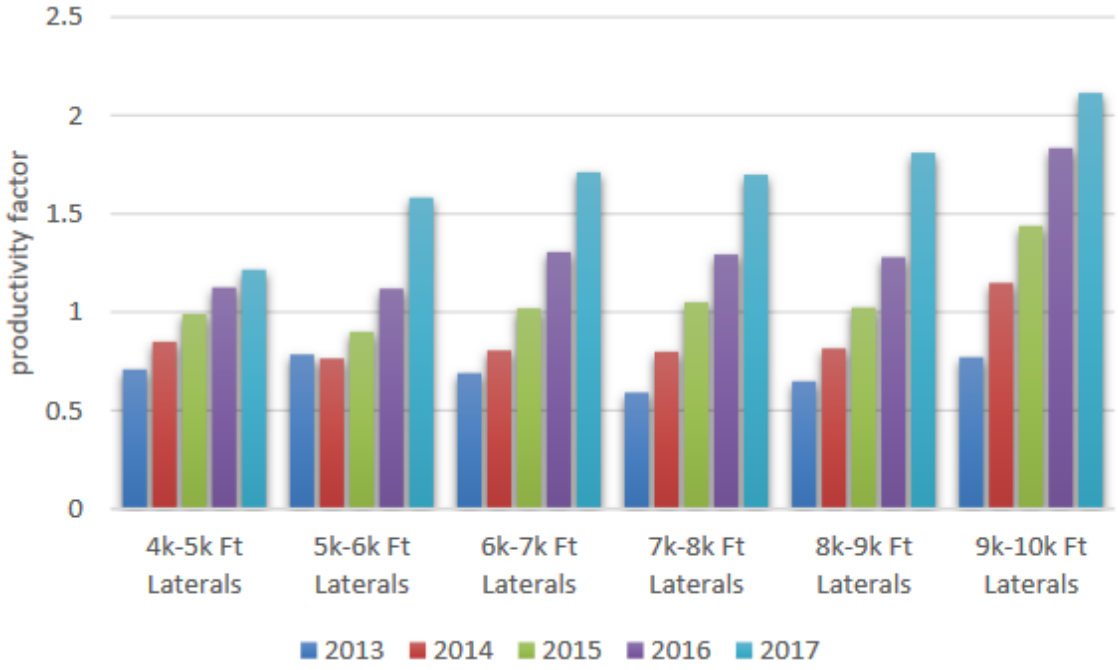

Figure 16. The growth in Permian basin horizontal well productivity normalized by 1000ft segment from 2013 to 2017 (Curtis and Montalbano, 2017). This growth is independent of lateral expansion, implies the completion enhancement in each frac-stage.

Despite different rock-fluid and completion qualities, the performance from tight reservoirs yields a common characteristic behavior of high decline rates, compared to conventional

reservoirs. **Table 2** lists decline analysis parameters by county of Eagle Ford shale. B-factor (0< b < 1) is hyperbolic decline constant; at high b-factor, reservoir production rate declines faster. Note EOG had piloted EOR in La Salle, Atascosa, Karnes, and Gonzales counties. EOG decided to extend their EOR program to 56 wells in 2017 and to 90 wells in 2018; all wells are in Gonzales county.

Table 2. Results from decline analysis for different liquid-rich wells in different counties in the Eagle Ford shale play. Hyperbolic fitting was applied. Data shows a large fraction of wells in La Salle is under boundary dominated flow, whereas, most wells in Karnes and Gonzales were under linear flow (Indras, 2014).

County	No. of wells	Dominant Fluid Type	Dominant Flow Regime	b
Dimmit	7	oil	3 wells in LF 4 in BDF	0.3
La Salle	348	oil	169 wells in BDF 179 in LF	0.41
McMullen	225	oil	53 wells in BDF 172 in LF	0.32
Atascosa	180	oil	7 wells in BDF 173 in LF	0.45
Karnes	833	oil	71 wells in BDF 762 in LF	0.32
Gonzales	450	oil	44 wells in BDF 406 in LF	0.29

As the main fluid transport element, cracks and fractures (naturally occurring or HF generated) greatly impact reservoir performance. For example, Parshall field in the Bakken shale yields higher crude production compared to neighboring fields, due to its high natural fracture density (Sorensen and Hamling, 2016). This is an example, where fractures can be beneficial. On the other hand, intensive fracture communication among offset wells, or frac-hit, in general has a negative effect on production. The existence of fractures makes containment and hence EOR extremely difficult.

Recent studies explained fast decline behavior of tight formations, can be due to two main reasons. One reason is the formation quickly fails to maintain pore pressure near the sand-face (fracture face); this is critical, especially in condensate or volatile oil window, where gas separation

occurs, and liquid phase is below critical saturation to flow. This effect has been observed as the increase of GOR with the production (Altman et al., 2014). An interesting question is raised: within the flow system, where would the liquid drop out effect be mostly detrimental? Is it in vicinity of sand-faces or within proppant pack?

There is also another interesting behavior observed for a major fraction of unconventional liquid-rich wells, in which GOR does not change even after long production periods when bottom-hole pressure is below bubble point, while production rate continuously decreases (Altman et al., 2014). In this scenario, it seems the reservoir can maintain pressure, while fluid conductivity becomes more and more restricted. This concept will normally not exist in conventional reservoirs, because matrix advection is the dominant transportation factor. But in shales, a dual permeability system, this scenario can happen (Tran et al., 2011). Our previous study (Dang et al., 2017), **Figure 9**, on shale compressibility has shown at low effective stress region, pore compressibility can be as high as fluid compressibility. With a small fluid release rate, pore pressure can be maintained; however, if cracks are the critical conductive element, their stress dependence, would allow them to close as pore pressure is reduced. In this case, reservoir would behave as infinite-acting boundary system (Zhang and Ayala, 2015). The following figure captures this scenario. After 12 months of production, GOR is constant; even after the flash production after gas injection on the 13^{th} month.

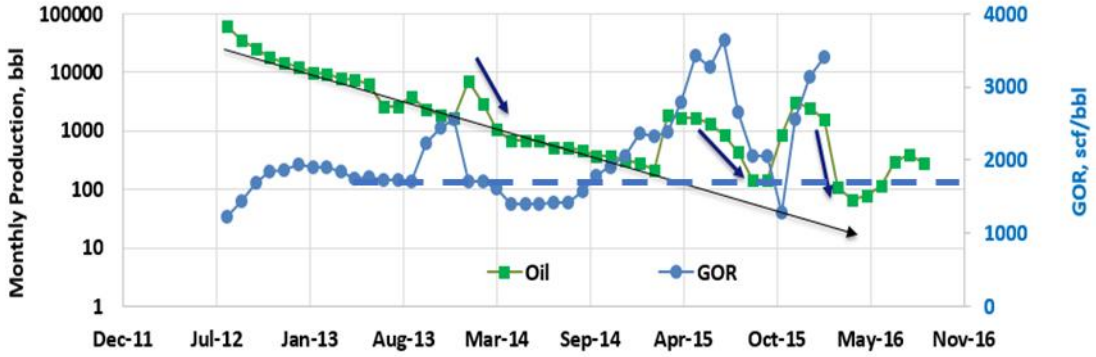

Figure 17. Monthly oil production and GOR for a liquid-rich well in Gonzales County, Eagle Ford. This well is one pilot well for the EOR project from EOG. GOR stays constant even after each huff-n-puff cycle (blue dash line), the general declining trend doesn't change. Production falls fast after each injection cycle (Texas Railroad Commission data, 2016).

II. Screening EOR Experiments on Crushed Samples

Minimum Miscibility Pressure Measurement

Assuming advection is one of the major mass transport mechanisms during the EOR huff-n-puff process, to achieve oil-gas miscibility, the injection pressure needs to be above minimum miscibility pressure (MMP). For miscible EOR in conventional reservoirs, high recovery factor can be attained using multiple contact miscibility process (MCM). This process includes the injection of small slug of rich gas followed by a large slug of lean gas; this requires lower injection pressures. Multi-contact MMP (MC-MMP) can be measured with the Slimtube® technique; at MC-MMP, the interfacial tension (IFT) between the oil and the gas phases does not need to reach zero. However, for tight reservoirs, with pore throat size on the nanoscale, the injection pressure is preferred to achieve first-contact MMP (FC-MMP), in which the interfacial tension between the oil and the gas phases completely vanishes (**Figure 18**). This guarantees capillary pressure becomes insignificant.

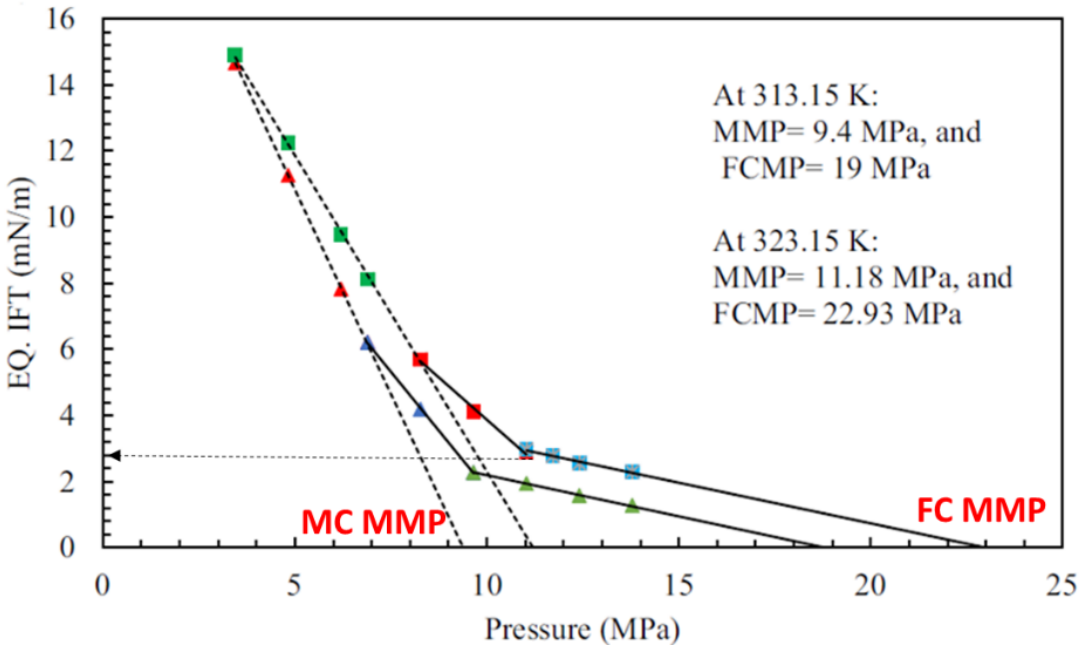

Figure 18. Golkari et al. (2017) measured the oil-gas interfacial tension (IFT) at different injection pressures. MC-MMP, acquired by Slimtube® measurements, does not guarantee IFT reaches zero. FC-MMP, acquired by VIT technique or a bubble rising test is preferable to determine MMP for tight rocks.

To measure FC-MMP, we propose using the vanishing interfacial tension method (VIT). In this technique, the observed interfacial tension was associated with the capillary rise within a small glass tubing (ID < 0.5mm). The pressure, at which the capillary rise disappears, is considered as FC-MMP (**Figure 19**).

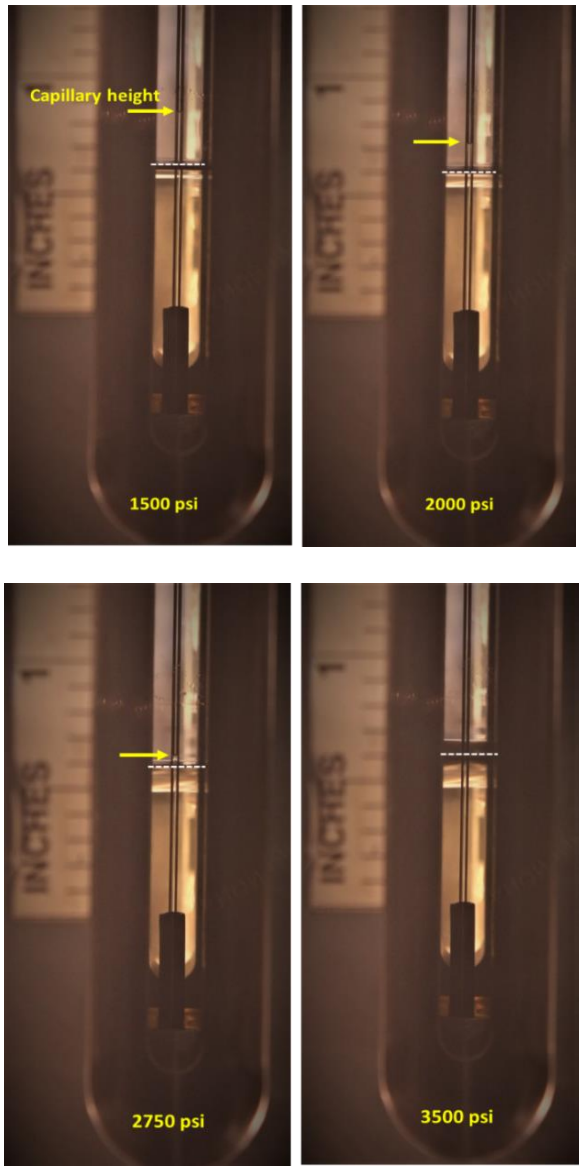

Figure 19. An example of a VIT measurement. The capillary rise of the oil phase inside a glass tube at different injection pressures (yellow arrows). The white dash lines correspond oil-gas contacts. At or above MMP, the capillary height (as the difference between the capillary rise and the oil-gas contact) would be vanished.

At a specific temperature, MMP is strongly governed by both the oil composition and the injection gas composition. With a same injection gas, the oil samples with higher intermediate fractions are observed to have lower FC-MMP; for example, dodecane or DV-1 oil (**Figure 20**). On the other hand, for an oil sample, the injection gas with richer ethane concentration yields lower MMP values (**Figure 20**).

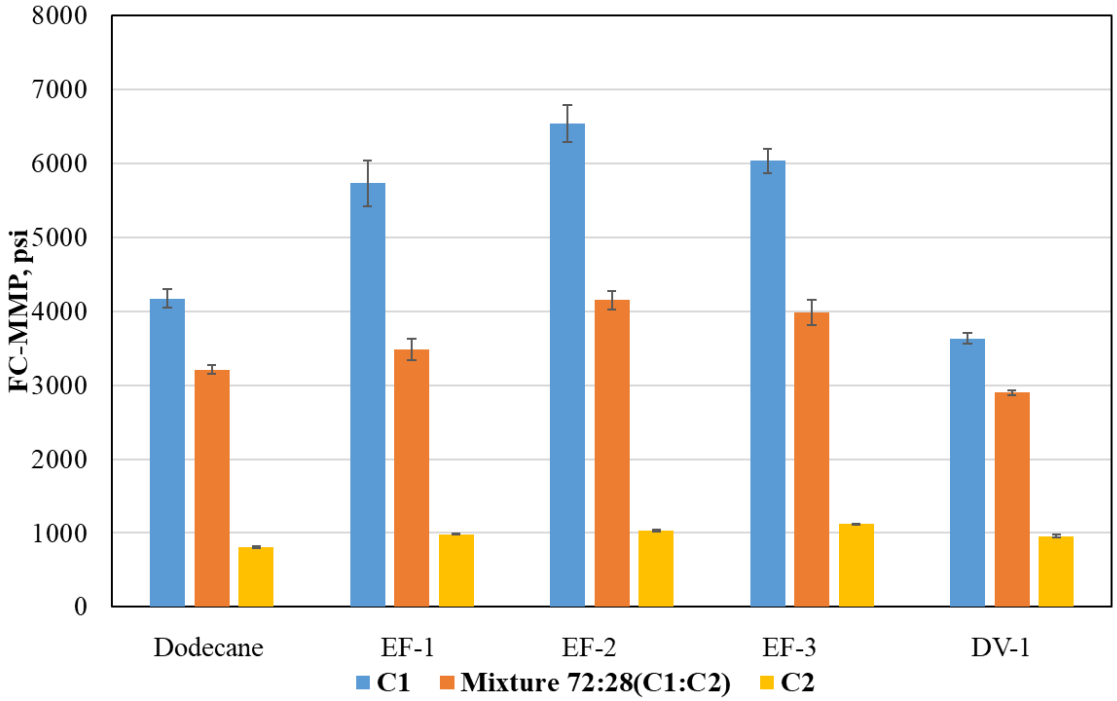

Figure 20. Summary of FC-MMP measures using the VIT technique for different oil samples with different injection gas compositions at the same temperature (T = 150°F). With a same injection gas, the oil samples with higher intermediate fractions are observed to have lower values of FC-MMP. For an oil sample, the injection gas with richer ethane concentration has a reduced FC-MMP.

EOR Recovery Measurements and Post Injection Characterization

As mentioned above, experimental results are presented in this section for the purpose of screening field parameters, which govern EOR recovery. To accelerate the screening process, experiments were performed on crushed preserved samples (samples were only crushed immediately before injection tests to minimize fluid loss), with the sample size of 6-8mm. Throughout the studies on both crushed tests and plug tests, all samples were cut from the same facies at the same depths. This helps to minimize the impact of sample heterogeneity while comparing results from different test configurations. **Figure 2**1 represents the general core scanning process and test specimen selection. Routine petrophysical characterizations were performed (**Table 3**), these provide general knowledge of sample properties, such as porosity, determined from a combination of Nuclear Magnetic Resonance-NMR and high pressure helium pycnometer-HPP tests, microstructure (Scanning Electron Microscope-SEM), pore-throat and pore size distribution (Mercury Injection-Capillary Pressure-MICP and Isothermal Nitrogen Adsorption-BET tests), mineralogy (Transmission Fourier Infrared Spectroscopy-FTIR), thermal maturity and hydrocarbon content (HAWK® pyrolysis).

Table 3. Results of the petrophysical characterization of the Eagle Ford samples, selected for EOR screening tests. The measurements include mineralogy, TOC, porosity, and thermal maturity.

Sample ID	**Total Porosity**	**TOC**	**Total Clays**	**Total Carbonates**	**Quartz + Feldspars**	**Maturity T_{max}**
	p.u.	w%	w%	w%	w%	^{o}C
EF1	5.1	4.9	16	62	13	456 Oil window

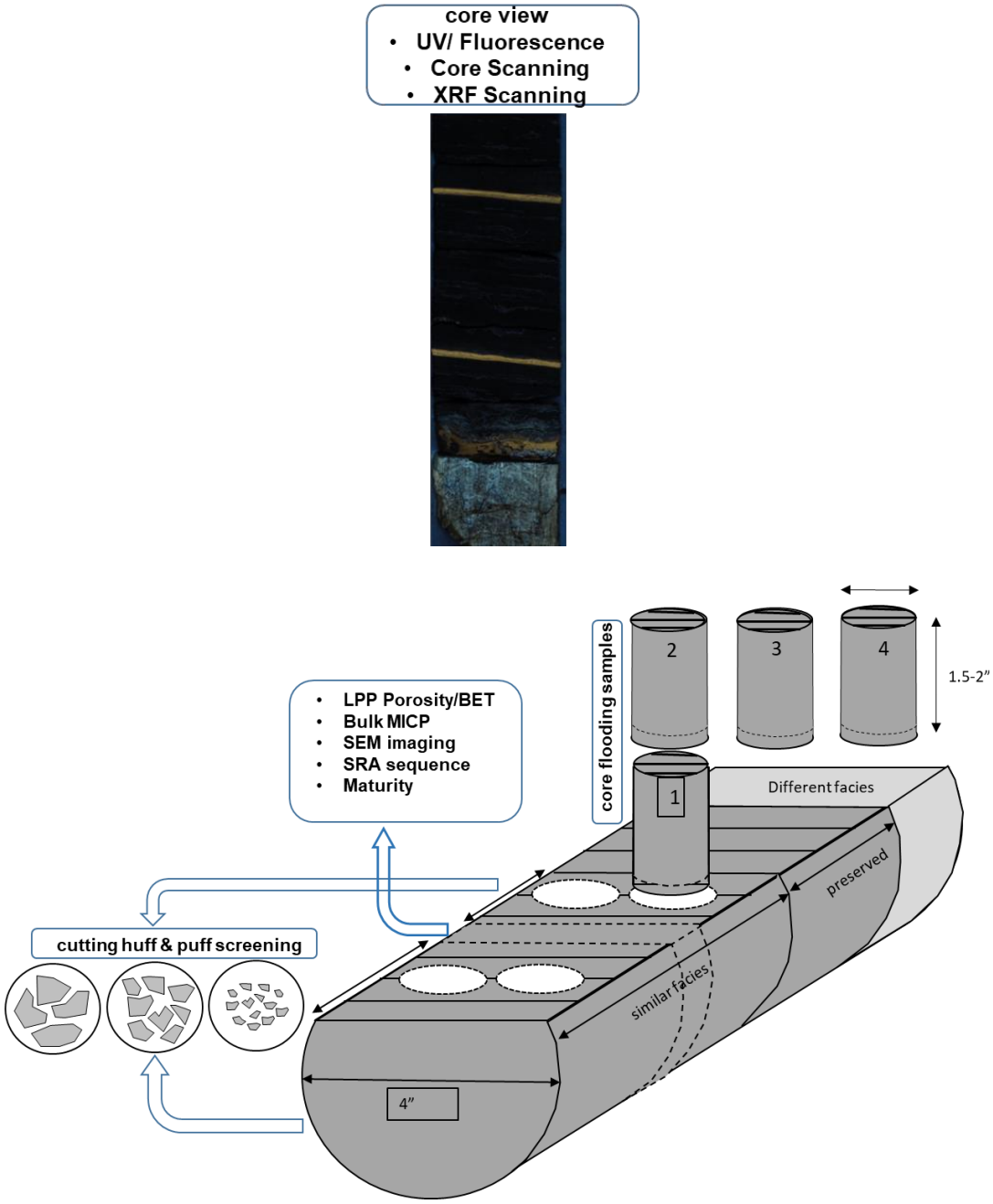

Figure 21. Throughout the study, all test specimens, including crushed samples and plugs, were cut from the same facies. From 1 ft of core, we were able to extract four 1"-diameter horizontal plugs for core flooding tests, and the rest of source material was quickly crushed and preserved back for screening tests. Routine petrophysical test were also performed, including mineralogy, TOC, pore-size/ pore throat distribution, microstructure observation.

Experiments for EOR screening tests were designed to simulate huff-n-puff gas injection process. Consistently, 25g of crushed samples were placed within a high temperature-high pressure cell. The cell was later placed inside an oven to maintain constant temperature during experimental cycles. The cell was connected to a syringe pump system which was used to compress gases from supply cylinders; the same pump is used to inject gases into the test cell at a designed pressure. A needle valve was connected to the cell outlet, this allowed controlled production rate or production time. **Figure 22** is a schematic of the experimental design used for EOR screening tests; only injection parameters were varied to evaluate their influence on the recovery.

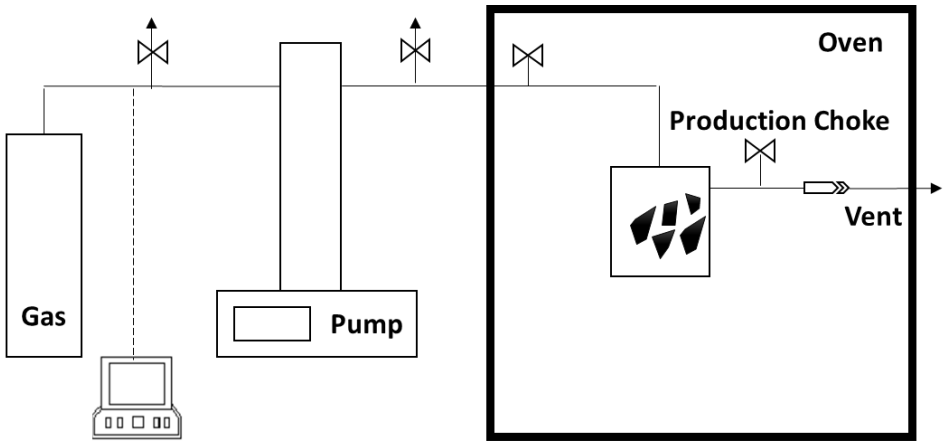

Figure 22. Experimental apparatus for EOR screening purposes. Crushed samples were placed inside a cell. The inlet was connected to a pump system, allowed to control injection pressure; the outlet was connected to a manual needle valve, which controlled production rate/ production time.

In addition to general petrophysical measurements, we also introduced the following characterization techniques, which allowed quantification of the remaining HCs within rock matrix throughout multiple injection/production cycles. Common practice for these experiments is to collect produced fluids, for later are quantification by secondary measurements. However, this approach is not applicable for tight rock EOR tests, since the original HCs content is very small,

which leads to inaccurate recovery estimation. Three sampling techniques are proposed; each technique has its advantages and disadvantages; however, their combination allows post-injection samples to be fully characterized.

Review of Nuclear Magnetic Resonance Measurements on Crushed Samples

Nuclear Magnetic Resonance (NMR) has been proven to be a useful tool to evaluate formation characteristics in both the laboratory and the field. NMR responses are induced during the relaxation of nuclear spins when subjected to a pulse sequence. At a specific magnetic-field strength, scanning frequency is tuned to resonate with the Lamour's frequency of hydrogen found in reservoir fluids, such as brines, oils, gases, and bitumen (Brown 1961; Bryan et al., 2002 and Hirasaki et al., 2003). Common NMR parameters used to interpret formation properties, include T_1, the longitudinal relaxation time, and T_2, the transverse relaxation time. Combination of T_1 and T_2 relaxation data can provide important information about formation pore structure and fluid properties. For conventional reservoirs, NMR has been used to estimate saturated porosity and pore size distributions (Keynon et al., 1986), from which permeability can be estimated (Coates et al., 1991; Kenyon et al., 1995 and Straley et al, 1994.) Recently developed applications of NMR, focusing on unconventional tight rocks, include the partitioning of pore surface affinity (oil-wet versus water-wet in shales) (Odusina et al., 2011; Valori and Nicot, 2019) and the characterization of *in situ* fluids.

NMR spectra, including T_2 relaxation distribution and T_1-T_2 maps, were acquired at a frequency of 12 MHz, using Oxford GeoSpec™ spectrometers, and Green Imaging LithoMetrix™ acquisition and processing software. The magnet temperature was set at 35^{o}C throughout the experiments. The optimal echo spacing of 114 μs, was chosen to capture fast relaxation

components in the shale samples (including fluids in small pores and heavy HCs components) (Besov at al., 2017), while preventing the interference from the fluorine signal from internal machine parts.

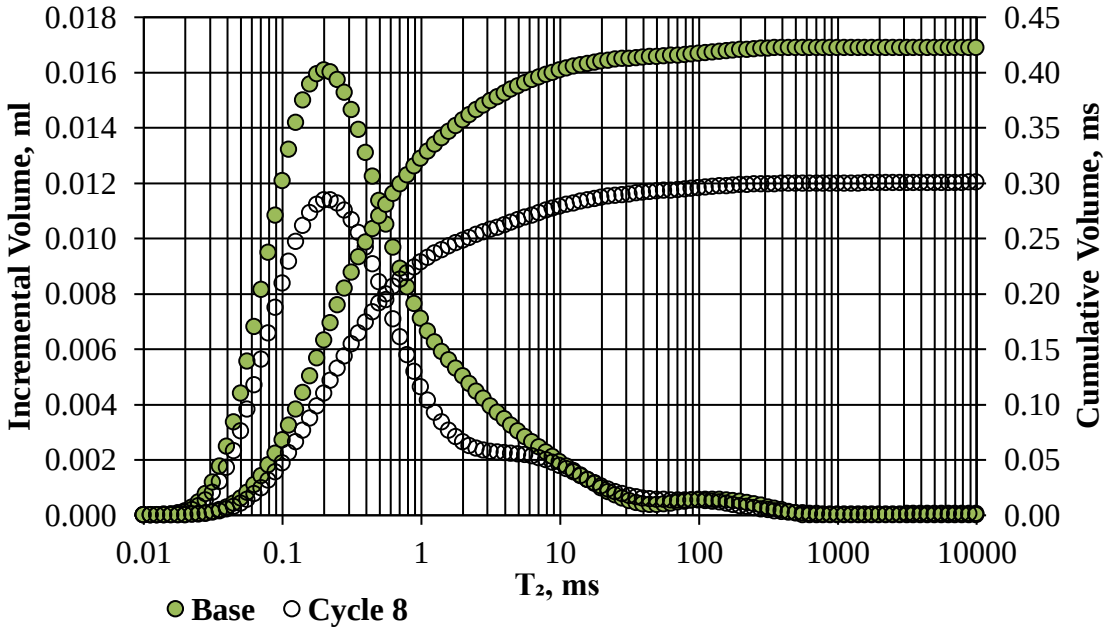

Figure 23. An example T_2 spectra for the same crushed sample at initial state (solid green), and after 8 huff-n-puff cycles (hollow). The plot includes both the incremental distribution (left) and the cumulative distribution (right). The difference between total fluid volumes is due to the recovery of HCs.

To quantify the HC content residing in rock matrix pre- and post- injection cycles, both T_2 data and T_1-T_2 maps were acquired. T_2 data (**Figure 23**) provided total fluid volume, including brine and HCs. T_1-T_2 maps (**Figure 24**) allowed the separation of different fluid volumes. By subtracting the brine volume (calculated from a T_1-T_2 map) from the total fluid volume (calculated from the corresponding T_2 spectrum), HC content could be estimated. The difference in HC volume before and after an injection cycle is a measure of incremental recovery. One major advantage of using NMR to estimate recovery is that it is a non-destructive measurement, therefore, subsequent huff-n-puff cycles could be performed on the exact same sample.

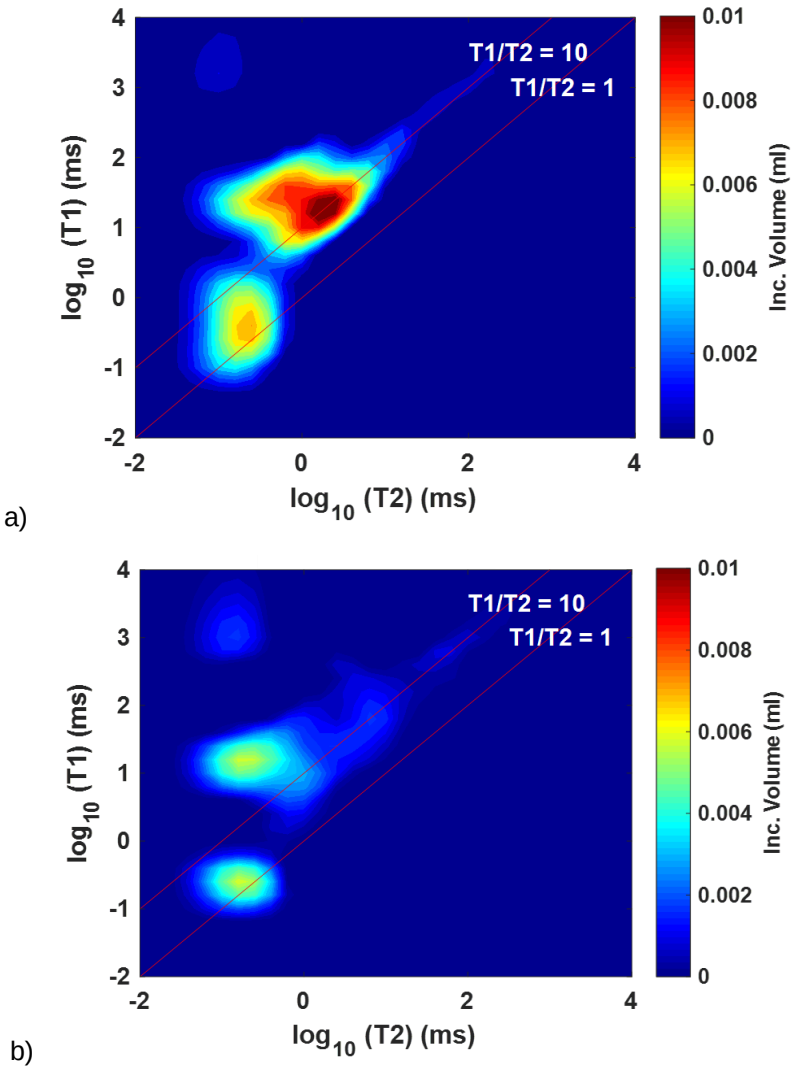

Figure 24. T_1-T_2 maps for the same crushed sample at initial state (a) and after 8 huff-n-puff cycles (b). Both maps were plotted with the same color scale. In each map, the brine volume can be determined by separating the signal clustered close to the 1:1 line from that above the 10:1 line. The HC volume signal occurs at a higher T_1:T_2 ratio line. The difference in HC content between two maps is the recovery after 8 cycles.

Review of Modified Rock Evaluation Measurement

While NMR measurements are non-destructive, subsequent huff-n-puff cycles remove the some of the source of the NMR signal, i.e. fluids, which results insubstantial Signal-to-Noise ratio

(SNR) decreases with increasing cycles. Secondly, NMR only provides indirect interpretation of the remaining HC properties. For example, after each cycle, we observed that T_1:T_2 ratio of HC signal increased (mainly due to the decrease of T_2 relaxation) (**Figure 24**); this could be interpreted as the remaining fluid resides in smaller pores or the remaining fluid is heavier. Therefore, to comprehensively understand what happened to the fluid system after each cycle, we proposed using a modified protocol of Hawk® pyrolysis to measure recovery. The advantages of this technique include:1) it provides the estimation of remaining HC content in mass units, 2) with the modified protocol, it allows a pseudo-compositional analysis of HC, 3) it is a fast screening technique. The disadvantage of using pyrolysis is that it is a destructive test.

HAWK® pyrolysis measurements have proven to be a useful method to evaluate source rocks. It offers the estimation of organic richness (TOC), thermal maturity, and converted HCs, which play a very critical role in exploration and development plans for unconventional reservoirs. Parameters such as S_1, S_2, T_{max}, etc. are interpreted from a pyrogram, a Flame Ionization Detector (FID) spectrum. These signals correspond to gases released while heating a rock sample under prescribed thermal heating profile (**Figure 25**). Produced HCs are quantified by the area below peak labeled S_1; this relates to available compounds with vaporization temperature less than 300^{o}C. In other words, S_1 only includes HCs lighter than $C_{17} – C_{27}$. However, HCs produced from different shales, especially in the oil window, also contain heavier compounds. The FID signal relating to these compounds generally overlaps with the S_2 peak (Dang et al., 2016), which is typically interpreted as un-cracked kerogen.

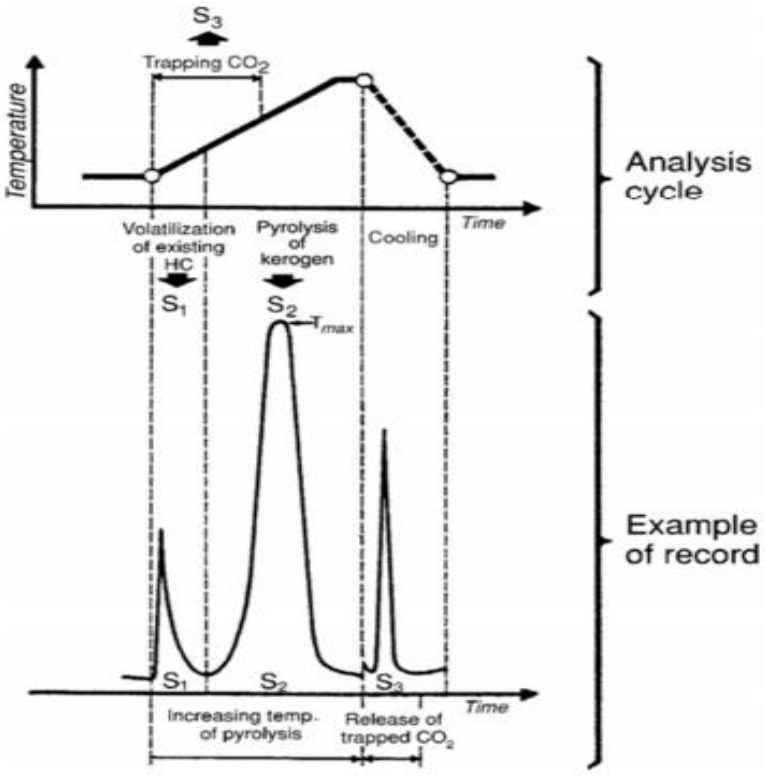

Figure 25. FID spectrum from HAWK® analysis (Tissot and Welte, 1984). S_1 corresponding to compounds vaporized below 300ºC and is considered producible HCs. S_2 is associated with pyrolysis of un-cracked kerogen.

Instead of following the standard protocol of a Rock-Eval® measurement, in which there is only a single thermal ramping step to evaporate HCs, we propose dividing the S_1 heating ramp into five thermal ramping steps (**Figure 26**). This allows delineation of five fractions of HCs, from $S_{1\text{-}1}$ to $S_{1\text{-}5}$. The corresponding HC fractions and thermal ramping steps are presented in **Table 4**. These temperature steps just provide a quick and rough compositional cutoff and cannot replace the traditional fluid analysis, like Saturates-Aromatics-Resin-Asphaltene (SARA) analysis, which is more precise but more time-consuming and costlier.

Table 4. Corresponding HC fractions and thermal ramping steps from the modified HAWK® measurement. These cutoffs were provided from a recent study coupling Rock-Eval® and GC-MS measurement (Abrams et al., 2017)

Peak	S1-1	S1-2	S1-3	S1-4	S1-5
Temperature Step, °C	< 100	100-150	150-200	200-250	250-300
HCs cutoff	<C7	C7-C13	C9-C17	C13-C24	C17-C27

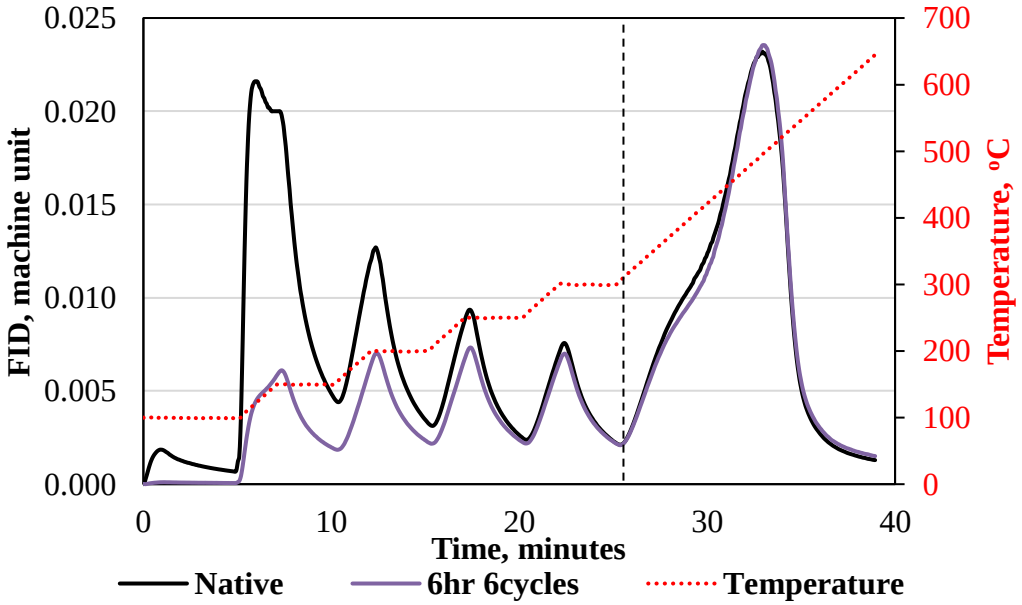

Figure 26. FID pyrograms for the same crushed sample at native condition (black), and after 6 huff-n-puff cycles (purple). The corresponding temperature profile is plotted in the dash red line. S_1 peak is separated into 5 peaks, representing different fractions of HC. The difference of the area below each peak, shows the bias of recovered HCs toward light components.

Review of Fluid Composition Analysis

Although the modified protocol used in the HAWK® measurements provides a quick way to understand the quality of remaining HCs after each cycle, traditional compositional characterization cannot be replaced to precisely determine the removable hydrocarbon fraction

throughout huff-n-puff experiments. Commercial SARA analyses were performed on pre-injection samples and a selected group of post-injection samples. Results would be normalized by sample weight which allows quantitatively comparisons. The detailed results of SARA analyses (**Figure 27**) were used to verify the observations of remaining HCs inferred from NMR and HAWK® pyrolysis measurements.

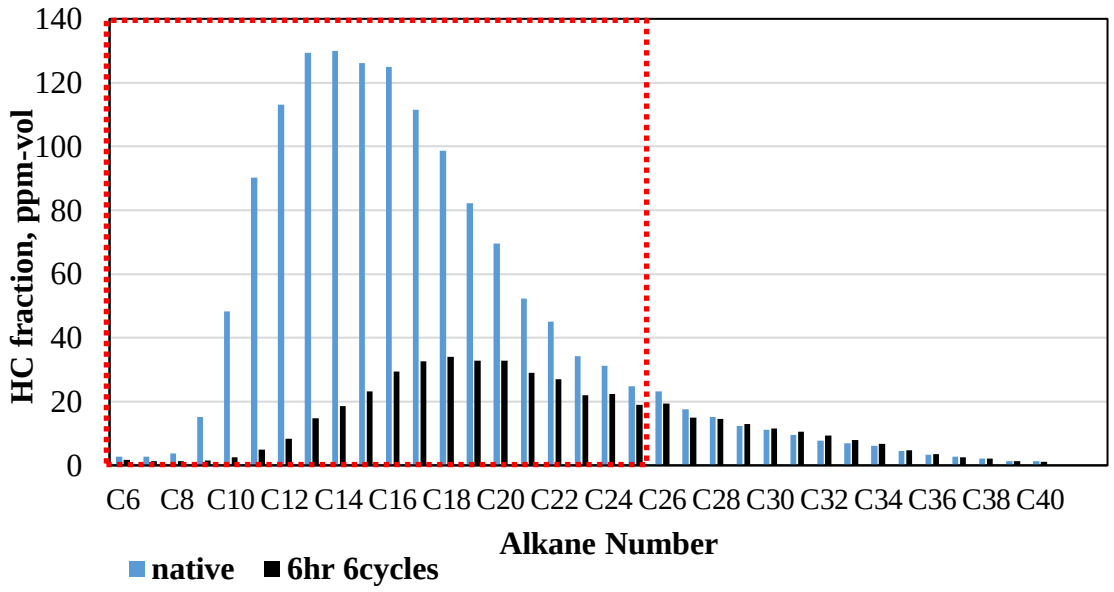

Figure 27. Alkane compositional analyses (from C_6 to C_{40}) on a crushed sample at pre-injection condition and after 6 huff-n-puff cycles. Only the fraction of HCs in the red box, corresponding to C_6-C_{25}, was removed during huff-n-puff experiment.

Results and Discussions

In this chapter, we review the impact of major injection parameters on the recovery in the EOR huff-n-puff process. The results will provide general guideline for injection-production strategies for field tests and development. However, it is important to say that all the following observations are biased toward small sample size with large sample surface area. Upscaling these observations is essential, which will be the focus of phase 3 in the overall EOR study.

1. Impact of Injection Pressure on Recovery

In this section, we evaluate the impact of the injection pressure on the HC recovery, for a crushed sample, using a specific injection gas (C_1:C_2- 72:28), at a temperature of 150^{o}F. The soaking time, 1hr, was kept constant throughout multiple-cycle experiments. Three injection pressures were chosen, respectively: at 1000 psi below MMP (MMP = 3500 psi), at MMP, and at 1000 psi above MMP. The recovery trends are shown in **Figure 28**. It is obvious that the final recovery is much lower (RF <10%), with the injection pressure below MMP. At this pressure and temperature, the gas phase was only able to vaporize a fraction of the remaining HCs (**Figure 29**). Moreover, when miscibility was not achieved, gas molecules could not be transported further inside rock matrix to remobilize the oil phase. At the injection pressure at or above MMP, the final recovery is above 25%. According to these results, there is no benefit of injecting gases at a pressure much higher above MMP. However, as mentioned previously, these experiments were performed on small specimens with large surface area and no effective stress was applied. The impact of excessive pressure above MMP will be discussed in the next chapter; in fact, its benefit is associated to the enhancement of surface area, when effective stress would decrease at higher injection pressure.

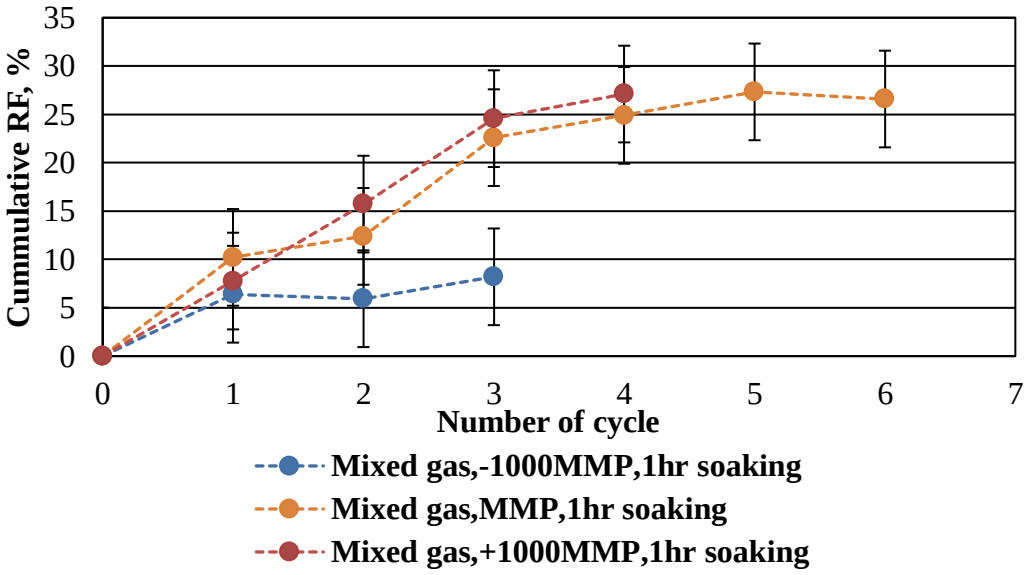

Figure 28. Impact of injection pressure on the huff-n-puff recovery factor in the Eagle Ford sample (MMP = 3500psi). At the injection pressure below MMP, recovery factor, RF, is small, i.e. <10%. Much higher RF is observed, for the injection pressure at or above MMP. For small sample size and no confinement applied, the injection pressure higher than MMP does not bring additional benefit in RF.

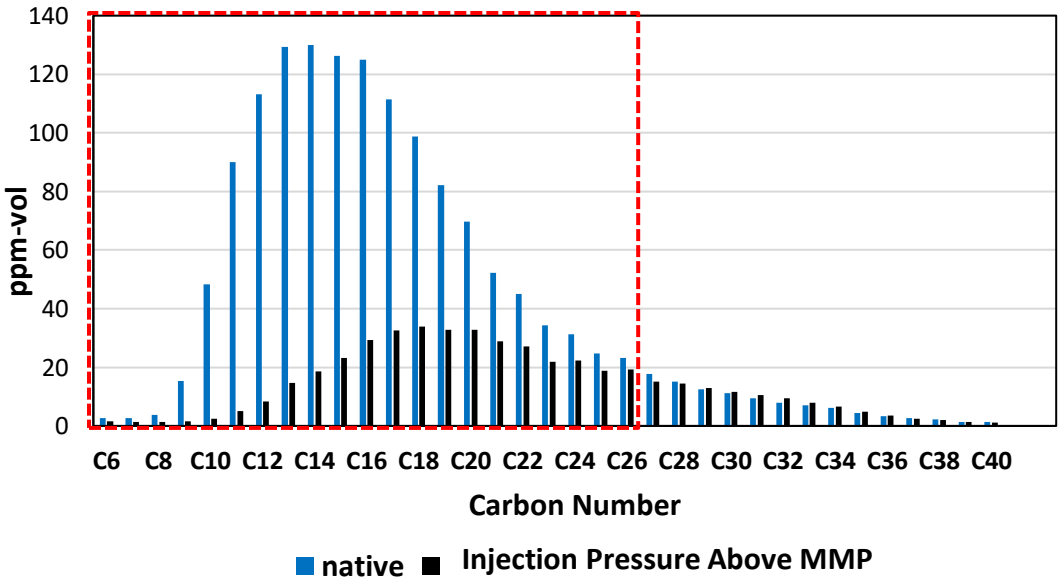

a)

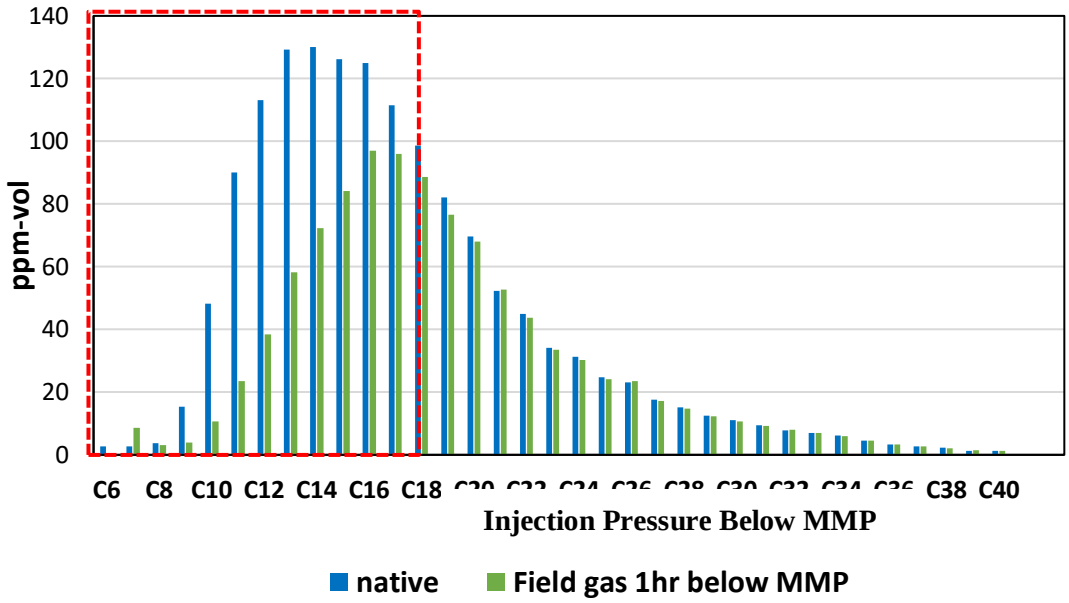

b)

Figure 29. Impact of injection pressure on the mobilization of HCs. GC-MS compositional analyses on pre-injection and post-injection samples; the difference between the two profiles is the composition of recovered HCs. At the injection pressure above MMP, major oil components were mobilized, whereas, with pressure below MMP, only up to C_{17} were recovered.

2. Impact of Soaking Time on Recovery

In this section, we evaluate the impact of soaking time on the recovery, for a crushed sample, using a specific injection gas (C_1:C_2- 72:28), at temperature of 150°F. The injection pressure, at 1000 psi above MMP (MMP = 3500 psi), was kept constant throughout multiple cycles. Three soaking times were chosen to be: 1hr, 3hrs, and 6hrs. The production time is consistently 1hr. The recovery trends are shown in **Figure 30-a**. If cumulative RF was plotted against the number of cycles, longer soaking time yields higher incremental recovery for first 4 huff-n-puff cycles. However, longer soaking time means longer dead time for a leased compressor unit. In **Figure 30-b**, the recovery trends were expressed in term of residence time, which is the sum of both soaking time and production time for each huff-n-puff cycle. It is obvious that longer soaking time seems

to be beneficial when compared on a cycle basis for a single well; but in field development for a lease-based injection strategy, shorter soaking time may be favorable, in which a compressor unit must be shared among multiple well-heads.

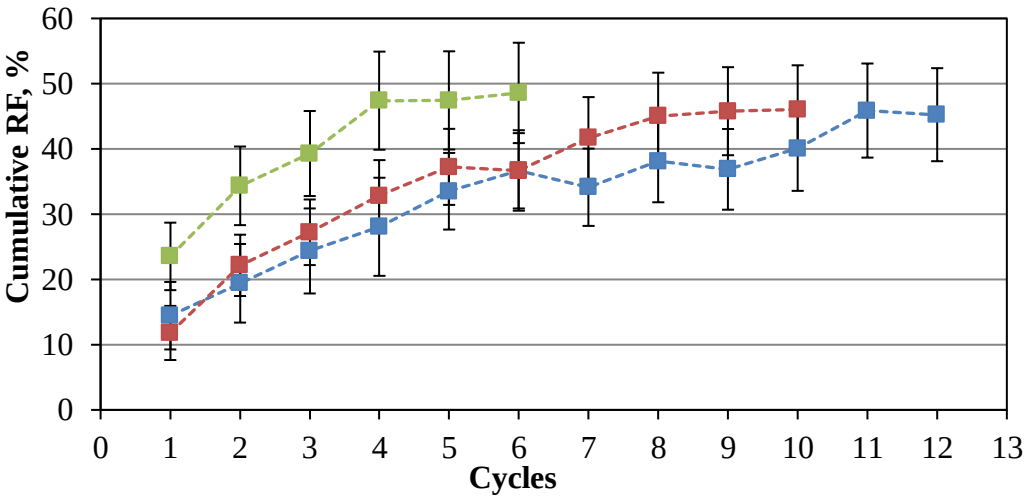

a)

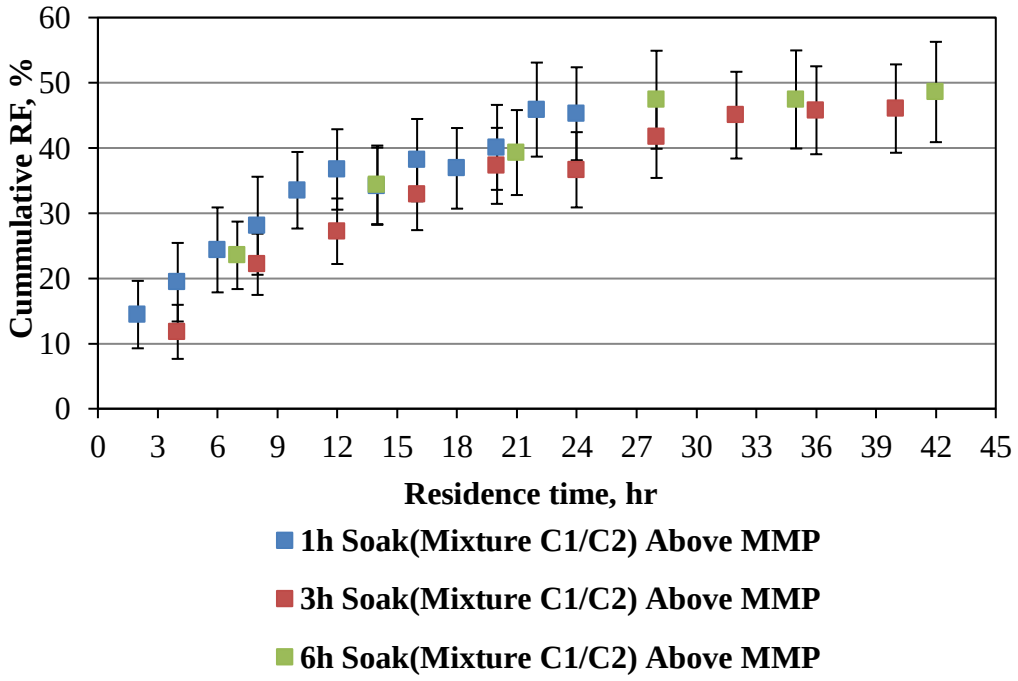

b)

Figure 30. The impact of soaking time on huff-n-puff recovery factor for the Eagle Ford sample. On cycle basis (a), longer soaking time yields higher incremental recovery, at least for first 4 cycles. However,

the recovery trend plotted against residence time is similar for the three different soaking strategies (b). In practice, shorter soaking time allows quicker rotation of the compressor unit among wellheads.

3. Impact of Injection Gas Composition on Recovery

In this section, we evaluate the impact of injection gas composition on the recovery trend, for a crushed sample of Eagle Ford shale, with a specific injection-soaking-production strategy and at a temperature of 150°F. The injection pressure was kept 1000 psi above MMP for the different injection gases; MMP for each gas was measured by the VIT technique. Five injection gases were chosen: CO_2, ethane, C_1:C_2-72:28, C_1:C_2:C_3-76:13:11 (namely, field gas), and C_1:C_2-95:5. The recovery trends are shown in **Figure 31.** It is obvious that injection gas composition has a strong impact on the huff-n-puff recovery. In addition to CO_2, natural gases with higher C_2+ concentration are the preferable choice. For example, with injection gas of C_1:C_2-72:28, recovery factor reaches 45%, whereas, with injection gas of C_1:C_2-95:5, the final recovery is only 20%. This observation can be explained as pressure decreases during the production phase, gases with higher methane concentration will drop out from the miscible phase faster. Moreover, richer gases are also able to mobilize heavier fraction of the HCs system, due to the molecular interaction for compounds with similar polarities. However, in practice, operators do not have many injection gas choices; therefore, the injection strategy, including injection time, or the time to initiate EOR play a critical role in the success of an EOR program.

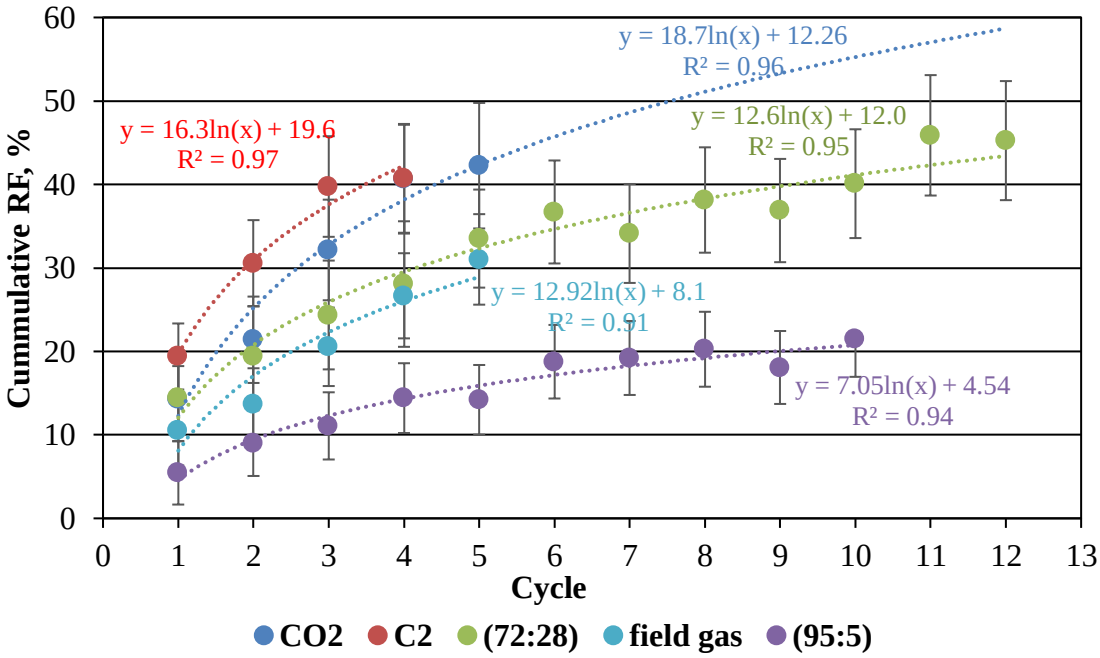

Figure 31. The impact of injection gas composition on huff-n-puff recovery on the Eagle Ford sample. At the same test conditions, injection gas with higher C_2+ concentration yield better recovery. CO_2 is also a good injection solvent, but often not available. Gas enrichment is recommended for field EOR.

4. Impact of Sample Size or External Surface Area on Recovery

We also evaluate the impact of sample size on the recovery trend, for a crushed sample, with a specific injection-soaking-production time, at a temperature of 150°F. In these experiments, the injection gas was CO_2, and the pressure was kept 1000 psi above MMP (MMP = 2500 psi). Four sample sizes were used: 0.9-2mm, 2-4.7mm, 4.7-6.7mm, and 6.7-8mm. After the 5 cycles, we observed the sample with smaller size or larger exposure surface, had a higher final recovery factor (from 54% to 72%). The recovery trends are shown in **Figure 32.** The impact of surface area will be explained in more detailed in the next chapter, in which mutual diffusion between the gas and oil phases would be proven to be a major mass transport mechanism. Upscaling to field

applications, the restoring of crack conductivity (which could be impaired during reservoir depletion) or the enhancement of surface area will be critical to shale huff-n-puff successes.

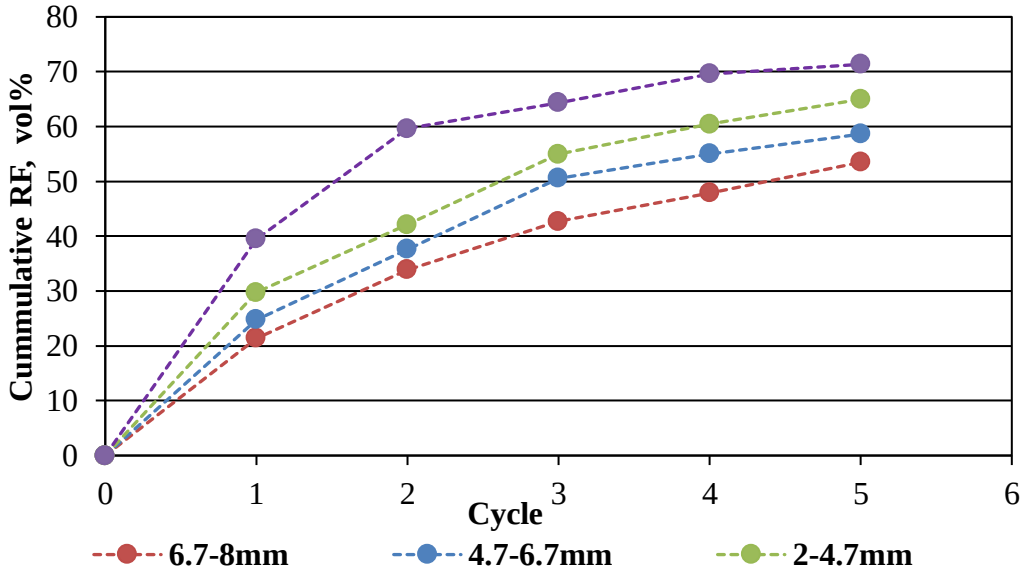

Figure 32. The impact of sample surface area on EOR recovery. It is obvious with smaller sample size, or higher surface area, the recovery is greater. Upscaling to field applications, the restoring of crack conductivity or the enhancement of surface area will be critical to shale huff-n-puff successes.

Post Injection Petrophysical Characterization

Throughout multiple huff-n-puff cycles, we also evaluated the alteration of the sample microstructure. In general, EOR gas injection at supercritical condition is not different from an organic solvent cleaning process, which would impact pore structure, pore-throat size, or internal surface area. Isothermal nitrogen adsorption (BET) measurements were utilized to evaluate the change in surface area and pore size distribution (for pores below 300nm in radius). **Figure 33-a** presents BET comparison of EF-1 sample between native state and after 10 huff-n-puff cycles (injection gas: C_1:C_2-72:28, T= 150°F, injection pressure: 4500 psi, MMP = 3500 psi, 1hr of soaking, 1hr of production). We observed that BET- surface area increased 250%, from 0.8m^2/g to 2.8m^2/g; and DFT inverted pore size distribution expanded toward smaller pore size, i.e. less

than 2nm of pore radius. In other words, huff-n-puff gas injection was cleaning HCs molecules adsorbed on pore surface and opened or exposed small pores. For this sample, EF-1, there was no significant change in pore-throat size, from the interpretation of MICP results between native and post-injection samples (**Figure 33-b**).

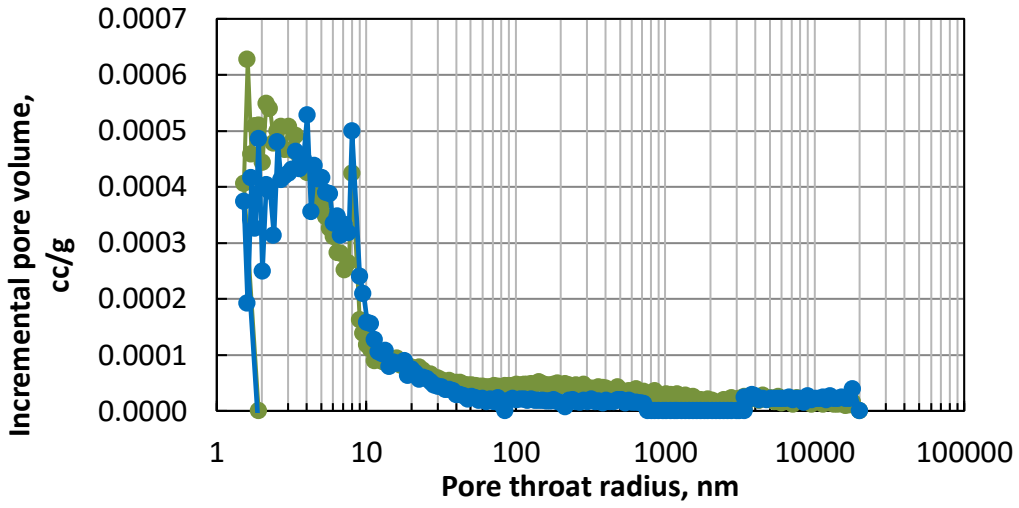

a)

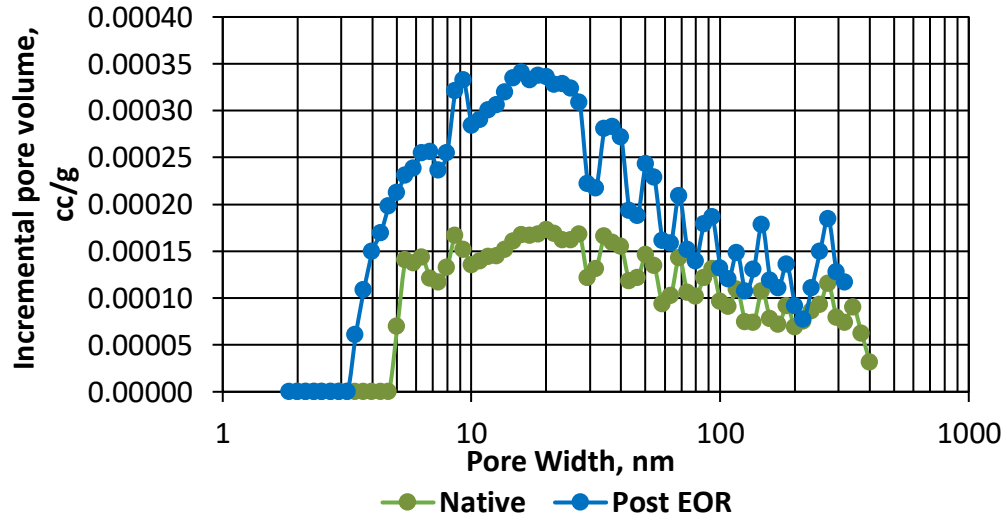

b)

Figure 33. MICP measurements (a) do not show significant change in pore throat size. However, isothermal nitrogen adsorption measurement (b) on EF-1 sample, show the change in BET surface area and the inverted pore size distribution. Nanopores, below 2nm, were exposed or opened after huff-n-puff.

However, when the same post-injection characterization study was carried out on another sample, DV-1, from a different tight formation, we observed the alteration in surface area, pore size distribution and pore throat size (**Figure 34-a&b**). This interpretation was also confirmed by SEM imaging (**Figure 35**).

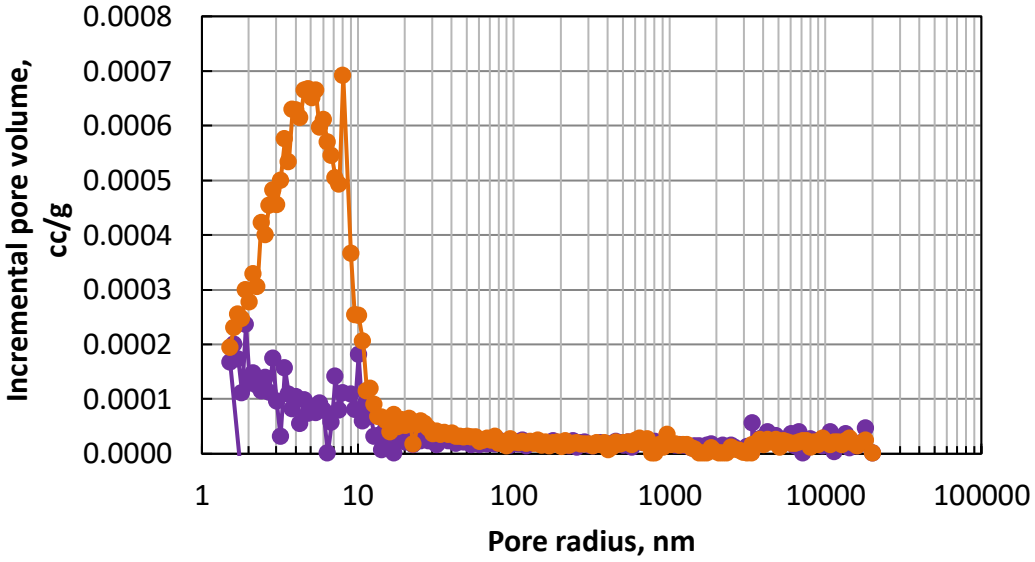

a)

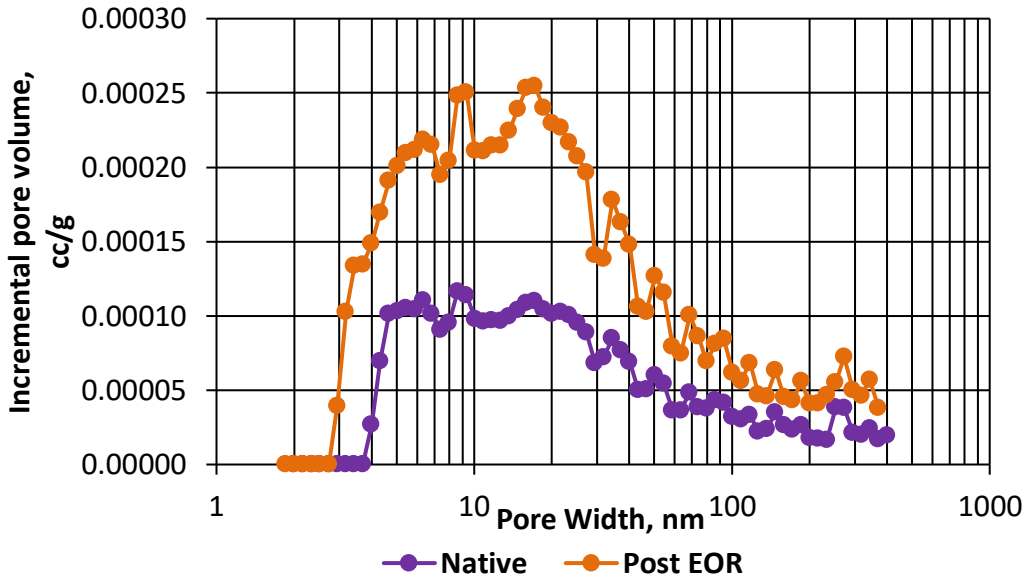

b)

Figure 34. MICP (a) and isothermal Nitrogen Adsorption (b) measurements on sample DV-1, show the change in BET surface area, pore size distribution, and pore-throat size. These interpretations are confirmed by SEM images.

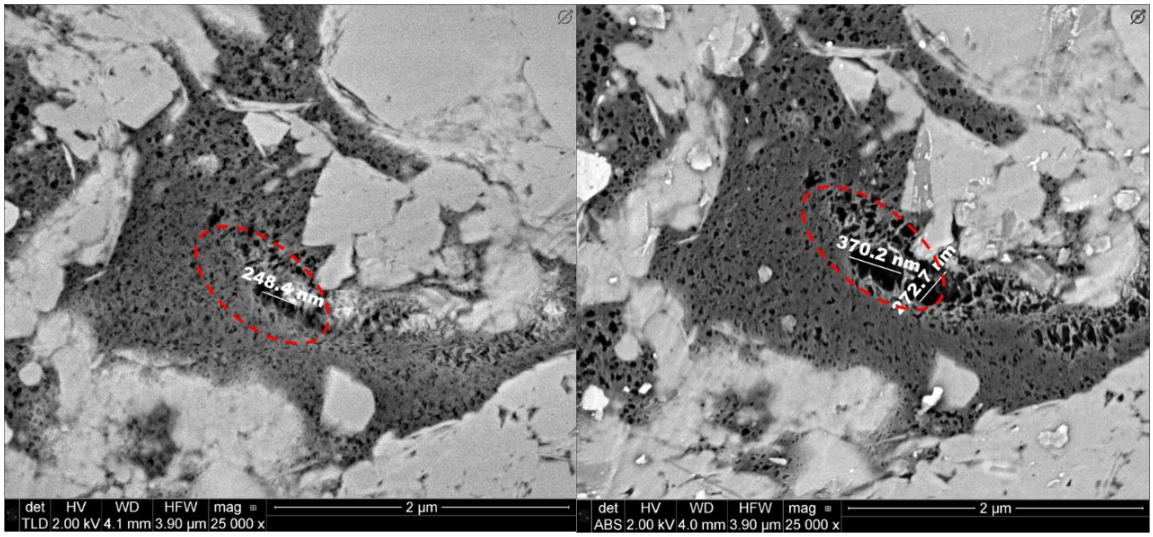

Figure 35. Microstructure alteration in sample DV-1 for pre- and post- injection. The increase in pore size was observed; this agrees with the interpretation from previous BET and MICP measurements.

Conclusions

While Phase 1 of this EOR study included rock and fluid sample characterization, Phase 2 provided preliminary understanding of the impact of various injection parameters on the final recovery factor. This phase included huff-n-puff experiments performed on crushed samples (6.7-8mm or smaller) to accelerate the screening process. The overall success of an EOR program does not only rely on the technical success (to achieve highest RF), but also the logistical aspects such as compressor capacity, compressor cycling and production soaking time. The major findings are listed below, note before extrapolating these observations to the field scale, more fundamental studies are needed (Phase 3):

- Injection pressure below FC-MMP yields much lower recovery factors, compared to recoveries from the tests with the injection pressure above MMP. For small sample size, there is no significant benefit of excessive pressure above MMP.

- Gases injected with pressure above MMP, promote the mobilization of heavier fraction of the HC content (up to C_{26}).

- On a cycle basis, longer soaking time provides better recovery; however, when compared against residence time (the sum of injection time and production time), there is no difference between 1hr of soaking and 6hr soaking. In field applications, optimal soaking time needs to be achieved, which will allow for quick rotation of compressor units among wellheads.

- CO_2 is a good injection gas, which yields a high RF for EOR huff-n-puff in shales. When using natural gases, the higher ethane concentration, the better RF. Enrichment of injection gasses will be beneficial, by reducing FC-MMP, and allowing mobilization of heavier HC fractions.

- Experiment-wise, test specimen with smaller size give better RF. In a field application, it is reasonable to conclude that surface area has significant control on the final recovery. Formation surface area is a function of crack density, natural fractures, induced hydraulic fracture network, and primary production-drawdown history.

- In general, we observed an increase in pore surface area [principally from the opening of smaller pores and pore-throat] in post-injection samples.

III. Plug EOR Experiment - Fundamental Recovery Mechanisms of Huff-n-Puff EOR in Tight Formations

Real-time EOR Monitor Measurements

As phase 2 provides preliminary knowledge on the controlling factors for a successful huff-n-puff process in shales, these understandings are drawn from screening tests on crushed samples. To upscale our observation to the field, fundamental mass transport mechanisms during huff-n-puff needs to be understood. For example, reported by Hoffman (2018) a pilot test in the Eagle Ford formation was implemented by an operator; the EOR process started with a charging cycle of 6-months of injection, the next two cycles had 2.5 months of injection, followed by shorter injection cycles of 1-1.5 months. The conclusion is after the injection strategy changed to the shorter injection time; a faster recovery trend was observed (**Figure 36**). It is obvious that to develop an optimal injection strategy for shale EOR, without trying too many costly field pilots, understanding fundamentals is essential.

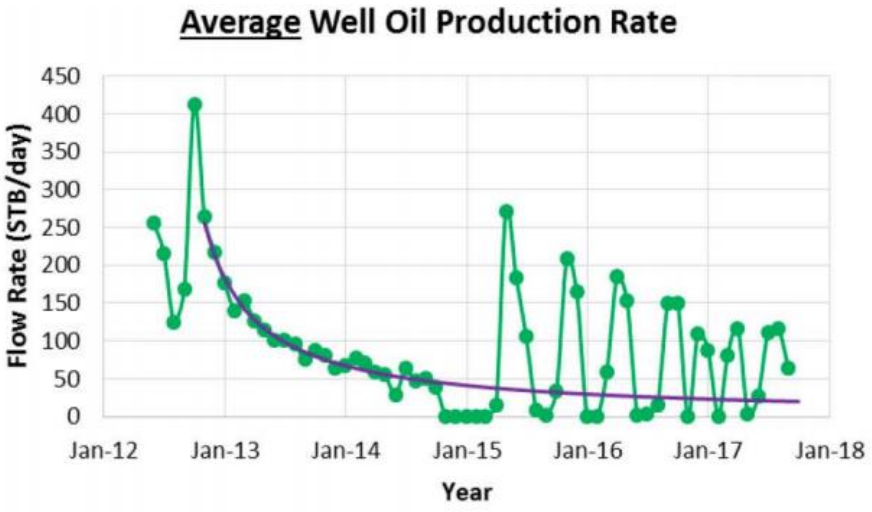

a)

b)

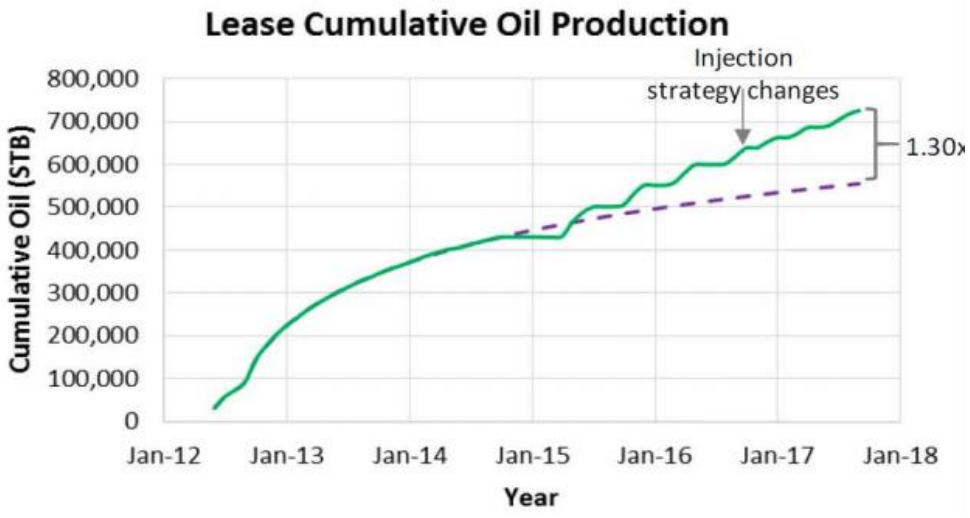

Figure 36. The results of an EOR huff-n-puff pilot in the Eagle Ford formation (Hoffman, 2018). (a) Incremental recovery and (b) cumulative recovery. The EOR process started with a charging cycle of 6-months injection, the next two cycles had 2.5 months of injection, followed by shorter injection cycles of 1-1.5 months. After the injection strategy changed to the shorter injection time, a faster recovery trend was observed.

One of the biggest drawbacks of the EOR tests, presented in phase 2, is that samples had to be removed from the test cell for recovery measurements. It raised the concern that pressure changes during sample removal could impact the final recovery. At the same time, we could not observe the dynamic interaction between injection gasses and the *in-situ* HC system, either during injection or production phases. To overcome these limitations, we need a real-time monitoring the EOR process. One possible monitoring technique is dynamic CT-scanning, which is successfully applied in many EOR studies for conventional rocks. However, for tight matrix with low porosity and small pores, CT-scanning does not offer enough spatial resolution to resolve the change within rock matrix. And, fluid interaction can only be indirectly interpreted via the alteration of phase density. If scientists want to quantitatively estimate the recovery, CT-numbers need to be calibrated.

To overcome the technical challenges mentioned above for tight rocks, we propose using uniform field Nuclear Magnetic Resonance (NMR), combining with specially made zirconium oxide pressure vessel for real time monitoring of the EOR process within rock matrix of core plugs. In parallel, a novel experimental apparatus was designed to monitor expelled fluids from gas injection tests. Again, the unique advantage from the combination of these techniques, is that they can provide the full understanding of dynamic interaction of the injection gas and the released HCs as well as those remaining within pores. For each huff-n-puff cycle, the pressure is maintained constant.

1. Nuclear Magnetic Resonance Measurements on Plug Samples

Introduction

Common NMR parameters used to interpret formation properties, include T_1, the longitudinal relaxation time, and T_2, the transverse relaxation time. Combining T_1 and T_2 relaxation data can provide important information about formation and fluid properties. Recently developed applications of NMR, focusing on unconventional tight rocks, include the partitioning of pore surface affinity (oil-wet versus water-wet in shales) (Odusina et al., 2011 and Valori and Nicot, 2019) and the characterization of *in situ* fluids. However, the interpretation is not straight-forward due to the coexistence of multiples fluids within a complicated pore structure made of inorganic pores and organic pores. During EOR gas injection, gas molecules are introduced into the matrix to mobilize residual HCs. To provide the accurate interpretation of NMR results while a huff-n-puff process is monitored, we will review the understanding of NMR response to HCs in bulk fluids as a function of temperature, as well as the new insights on how gas pressurization/ depressurization influences NMR response in organic rich tight rocks.

Experimental Instruments and Samples

NMR spectra, including T_2 relaxation distribution and T_1-T_2 maps, were acquired, using Oxford GeoSpec™ spectrometers, and Green Imaging LithoMetrix™ acquisition and processing software with CPMG sequence. For EOR flow through experiments, we utilized a 2 MHz NMR spectrometer. Compared to the 12 MHz instrument, which were used for simple screening EOR tests, the low field 2 MHz instrument had a better SNR.

For pressurization experiments, the samples were placed inside a Daedalus® pressure cell, made of NMR transparent ZrO_2; the cell can be operated up to 10,000 psi internal pressure. The cell was positioned inside the NMR spectrometer, in which cylindrical samples were aligned with the uniform section of the permanent magnetic field. The cell was connected to a syringe pump system which was used to compress gases from supply cylinders and inject gasses into the test cell at a designed pressure. The solvent gas was injected from every direction all around specimens. To understand the dynamic response of only the HCs components in rock samples during gas pressurization and depressurization, NMR transparent gasses were chosen. Injected gas candidates include CO_2, N_2, or CD_4 (deuterated methane). **Figure 37** illustrates major components of the experimental setup. Note there was no confinement applied on rock samples, gasses were injected at pressure all around the samples.

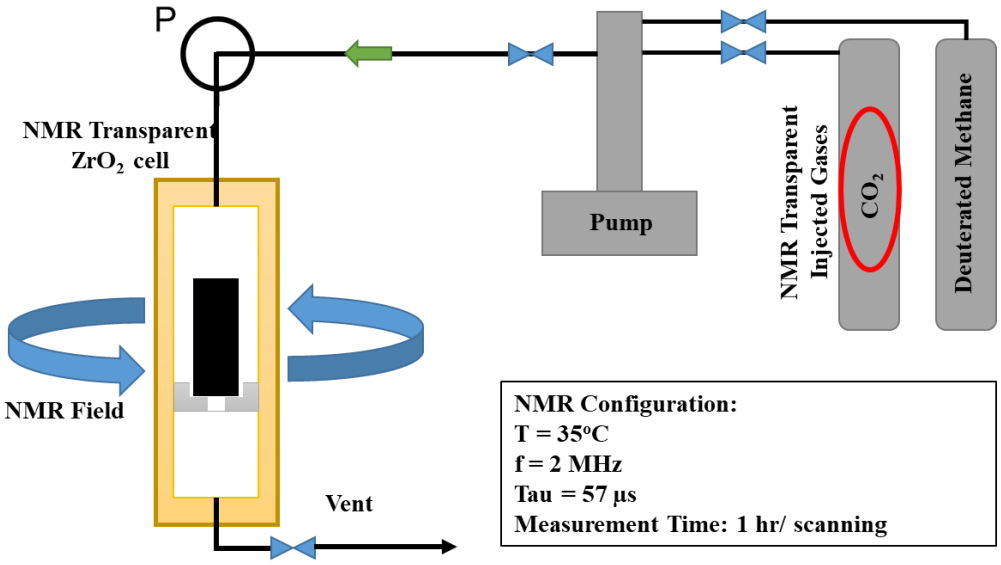

Figure 37. General experimental setup, including NMR transparent ZrO_2 pressure cell, placed within 2 MHz NMR spectrometer. The cell was connected to a pump system and to a vent line. NMR transparent injected gasses were chosen, including CO_2, N_2, or deuterated methane. 1"-diameter specimens were placed within the uniform section of the magnetic field. Note the solvent gas was injected all around the samples; all these specimens were horizontal plugs.

Four organic rich tight samples were selected for this study from various shale plays; two were preserved samples. Routine petrophysical characterizations were performed and presented in **Table 5**, including total porosity (the sum of high-pressure gas-filled porosity and NMR saturated porosity), mineralogy measured by transmission Fourier Transform Infrared spectroscopy (FTIR), and TOC measured with a LECO® instrument.

Measurable Fraction of HCs under NMR Spectroscopy

For T_2 relaxation acquisition, if a magnetization vector relaxes faster than the instrument echo spacing, protons inducing those magnetization vectors cannot be observed with the NMR spectrometer. Fast relaxing components in organic tight rocks include: 1) fluids bound in small pores, 2) highly viscous fluid components (bitumen or heavy alkanes), 3) fluids with strong

affinities for pore surfaces and 4) existence of paramagnetic minerals (pyrite or siderite). The existence or coexistence of these factors make the interpretation of NMR response of HCs in shale samples complicated.

Table 5. Petrophysical characterization of four samples. These samples are from three different tight formations.

Sample ID	**Porosity**	**TOC**	**Mineralogy,** w%				**Sample Condition**
	p.u.	w%	**Total Clays**	**Total Carbonates**	**Quartz + Feldspars**	**Others**	
A	11.2	7.2	43	0	42	15	**Non-preserved**
B	5.8	5	33	18	48	1	**Preserved**
C-1	5.1	4.9	16	62	13	9	**Preserved**
C-2	8.5	7.2	32	45	15	8	**Non-preserved**

Figure 38 illustrates the impact of surface affinity or pore type on NMR response. *In situ* HC compositional analyses and LECO® TOC measurements were performed on two rock samples. In spite of similar HCs species (confirmed by their similar HC distribution using modified Hawk® pyrolysis), sample (**1**) with lower TOC, more inorganic pores (implied weaker surface affinity to *in situ* HCs), the HC signal was observed in slower relaxation region; whereas, for sample (**2**) with higher TOC, more organic pores (implied stronger surface affinity to *in situ* HCs), the HCs signal was observed in a faster relaxation region.

Dang et al., (2019) also synthesized a set of six oil samples from the distillation of a produced crude under inert conditions. The crude was heated to elevated temperatures to generate oil

samples with successively increasing mean molecular weights. Since NMR measurements were performed at 35°C, the results suggest that NMR response for these oil samples correlated well with the existence of < C17 fraction. **Figure 39** shows good agreement between NMR response and HAWK® S_1 peak intensity (Dang et al., 2019). S_1 is associated with the measured fraction of total HCs with vaporization temperature equal to or less than 300°C.

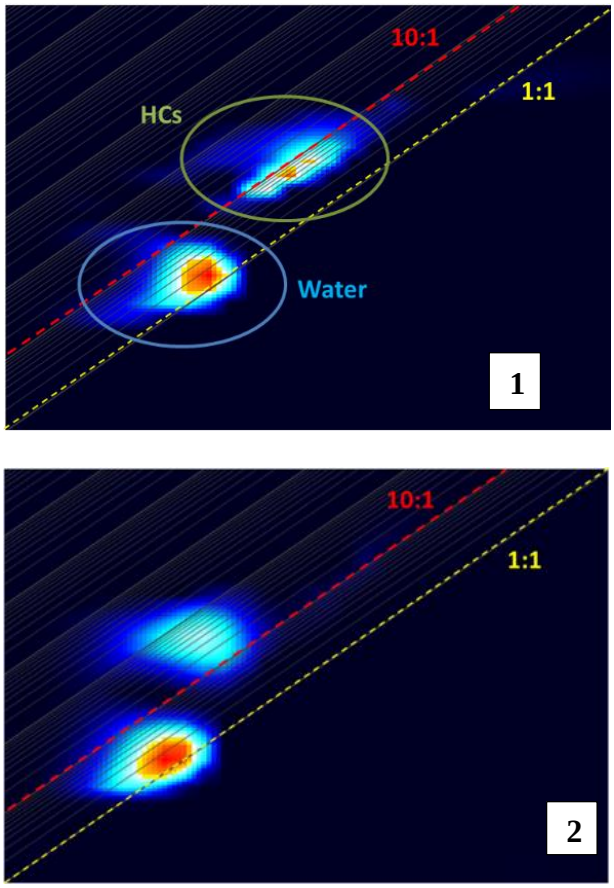

Figure 38. T_1-T_2 maps of two preserved tight samples with T_2 is on the x-axes, and T_1 is on the y-axes. Brine NMR response is close to 1:1 line (yellow dash line). Sample (**1**) with dominant inorganic pores, the HCs NMR response is between 1:1 line and 10:1 line (red dash line). Sample (**2**) with dominant organic pores, HCs NMR response is above 10:1 line, suggesting stronger affinity between HCs and the pore surface.

Previous studies (Hirasaki et al., 2003; Chakravarty et al., 2018, and Dang et al., 2018) on NMR properties of petroleum reservoir fluids also suggests that besides tool configuration and echo times, NMR response is sensitive to the mobile fraction of HCs, which is clearly a function of fluid composition and temperature.

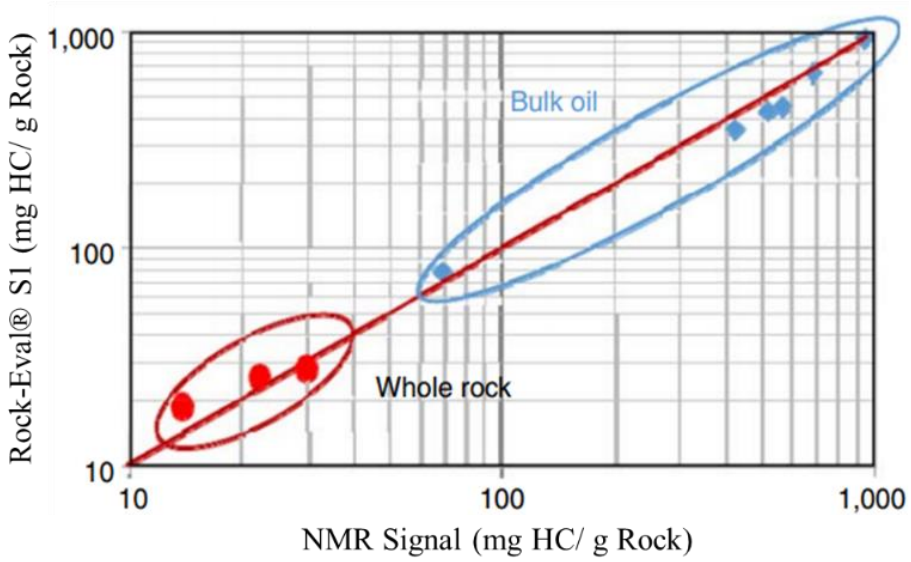

Figure 39. Comparison between NMR response for HCs and HAWK® S_1 (Dang et al., 2018) S_1 intensity represents the fraction of HC components vaporized at or less than 300°C, or roughly <C17 fraction. Blue data points are from bulk oil samples; whereas red data points are from rock samples. NMR response is sensitive to the mobile fraction of HCs, which is clearly a function of fluid composition and temperature.

Impact of Gas Pressurization and Depressurization on NMR Response

As previously mentioned, the mobile HC fraction is governed by overall fluid composition and temperature. Since NMR response is sensitive to HC mobility, it is critical to understand the role of gas loss while rock samples are brought to surface conditions. Gas loss changes the overall HC composition, making the comparison between NMR benchtop measurement and downhole

wireline responses inexact. On the other hand, NMR sensitivity to fluid mobility makes it a useful tool to evaluate HC mobilization during gas injection EOR studies.

To focus on the dynamic change of *in situ* HCs within the rock matrix, experiments were performed with NMR transparent gasses. **Figure 40** shows NMR T_2 spectra of sample **C-1** as CO_2 is injected at different pressures. As injection pressure increased, T_2 spectra shift to the slower relaxation times (1-10ms), and signal intensity in the fast relaxation region (0.1-1ms) decreased. These behaviors can be accounted as either by the reduction of heavy HC's viscosity or the movement of *in situ* fluid into larger pores. However, when the injection pressure was dropped (within a short time period), we observed the reversibility of T_2 spectra to the original distribution, which suggested viscosity of the original fluid was reduced or mobilization of HC as the main mechanism for this behavior.

We also obtained T_1-T_2 maps, which help to separate brine from the HC signals. HC volume in the rock matrix could be calculated by subtracting brine volume from total fluid volume. **Figure 41** shows the normalization of HCs volume in the rock matrix as a function of injection pressure. In addition to the shift toward slower T_2 relaxation, HC volume detected by NMR increases with injection pressure. This result confirmed the existence of a fraction of HCs which was invisible to NMR under routine laboratory condition. For some samples, the HC volume can increase by 25vol% from initial condition to 5000 psi pressurized condition. **Figure 42** illustrates the mobilization of HCs during gas injection, which reduces fluid viscosity and makes the originally undetectable fraction of HCs become visible under NMR at high injection pressure. Beside the reduction of HC viscosity, the move of fluid from small pores to larger pores can yield the same phenomena.

Figure 43 shows the hysteresis of normalized HC volume as a function of pore pressure between pressurization and depressurization. While pressurization data confirms the mobilization of HC, depressurization data suggests the existence of a gas trap phenomenon inside the HC phase during depressurization. Translating to field applications, huff-n-puff EOR can be effective by increasing remaining HC mobility. Due to potential gas trapping mechanisms, engineers can plan for shorter subsequent injection cycles.

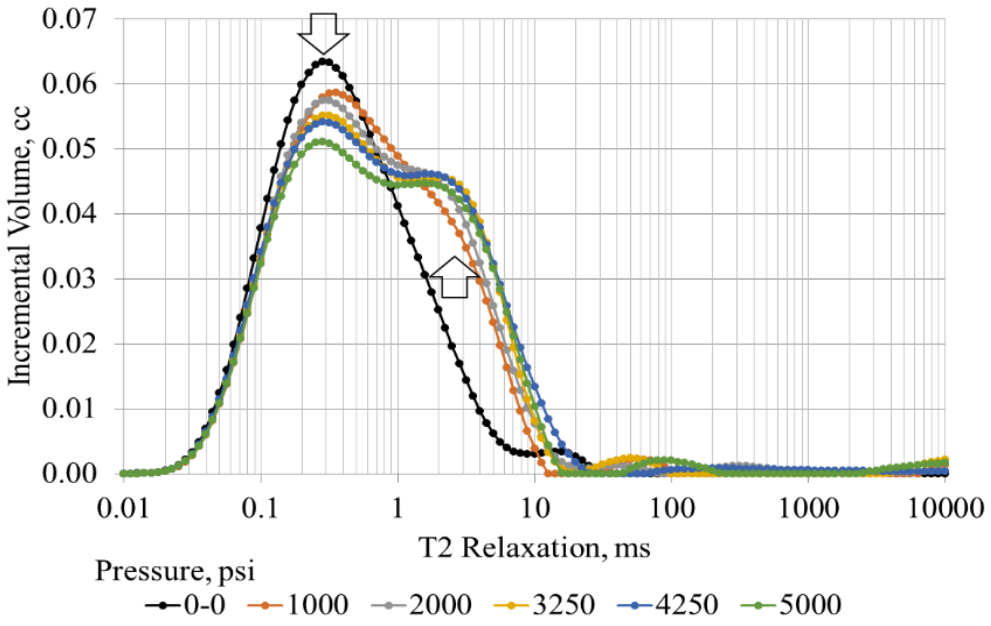

Figure 40. T_2 spectra of sample **C-1** with the injection of CO_2. Black spectrum is NMR response at original conditions. T_2 spectra were observed to shift to slower relaxation times (1-10ms), and signal intensities in the fast relaxation region (0.1-1ms) decrease. These changes suggest the reduction of fluid viscosity.

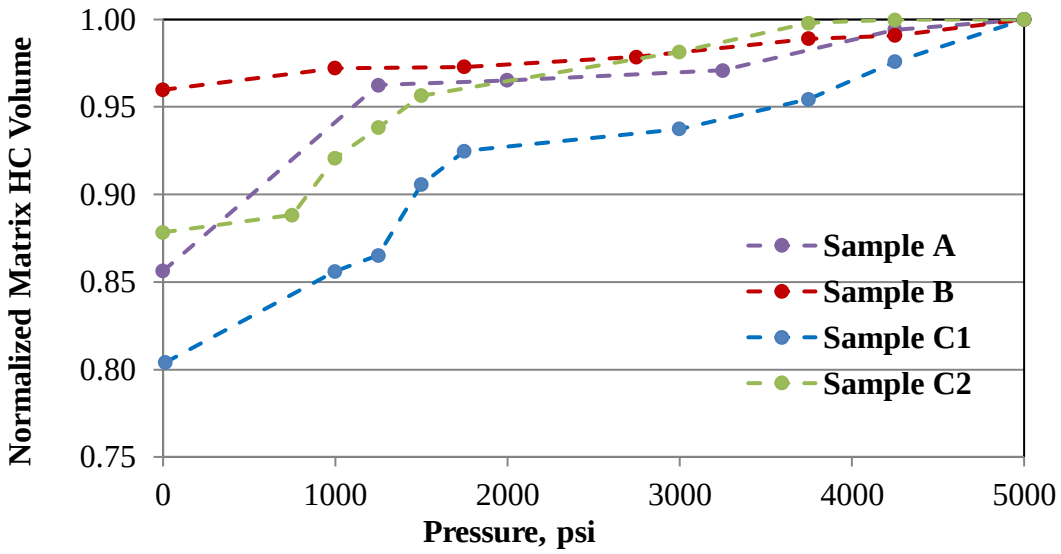

Figure 41. Normalized HCs volume as a function of injection pressure (constant temperature =35ºC). HC volume detected by NMR increases with injection pressure. This suggests the existence of a fraction of HC, originally invisible for NMR under routine laboratory condition.

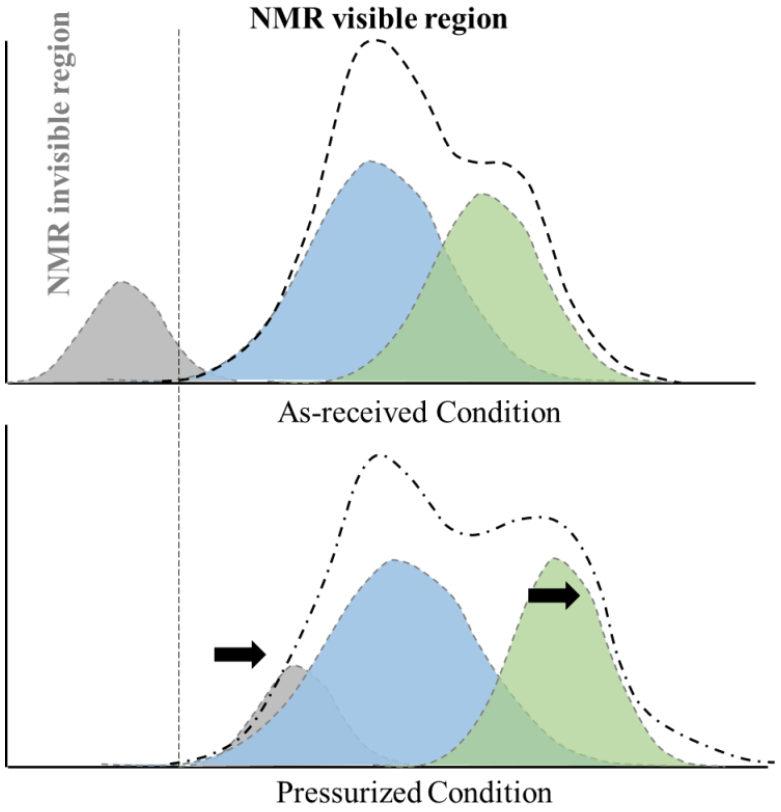

Figure 42. Scheme for the mobilization of HCs during gas pressurization experiments. Blue peaks correspond to brine, green peaks correspond to light/ originally mobile HC fraction, and gray peaks correspond to heavy HC components. Gas pressurization reduces fluid oil viscosity, brings the HC signals toward slower relaxation times. This makes more HC detectable by NMR than at the original condition without gas injection.

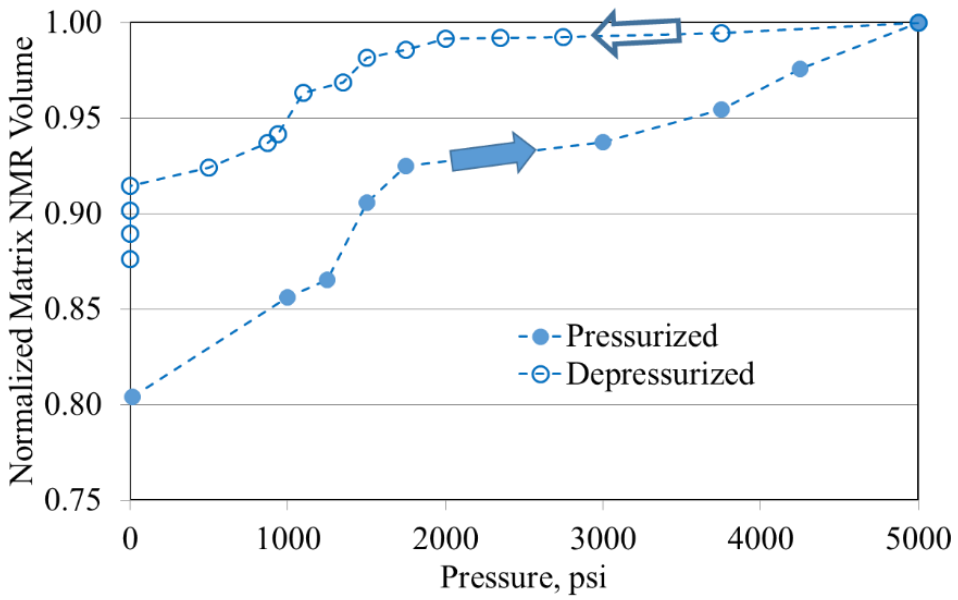

Figure 43. Normalized HC volume detectable under NMR as a function of gauge pressure during pressurization and depressurization. Each measurement point in this plot is the result of 35minutes- NMR scan. The hysteresis between two data sets, suggest gas trapping during depressurization. Obviously, this hysteresis is also a function of time. Note at 0psi, more gases escaped out with longer time, which reduced NMR amplitude.

NMR EOR Measurement Results

As mentioned above, real time NMR was utilized to monitor the dynamic alteration of the HC content within rock matrix during the huff-n-puff experiments. In field EOR experiments, the usual choices of injection gases include CO_2 or natural gases (with different methane percentages). However, to solely observe the response of pre-existing HC within rock specimen during gas

injection, we choose CO_2 as the injection solvent; this gas is transparent in NMR spectroscopy (other options include N_2 and deuterated methane). For each experiment, T_2 spectra were collected every 1hr (for experimental details, see III.1). Identical huff-n-puff strategies were applied for all four plug samples (**Table 5**); the details are as follows:

- Tests were run at 95^oF
- 1 day of injection with constant pressure
- 1 day of production during which gauge pressure was slowly reduced to 1250psi, then dropped to 0 psi.
- For each sample, the first three cycles were performed with increasing injection pressures of 3750 psi, 4250 psi, and 5000 psi (MMP = 2500 psi). Injection pressure was kept at 5000 psi in subsequent cycles. The whole huff-n-puff experiment was carried out until the recovery trend reached a plateau.

Throughout every step of a huff-n-puff experiment, HC was expelled from rock matrix. We can use NMR T_2 spectra to differentiate the remaining HC fraction and the expelled HC fraction, using a T_2 cutoff of 20ms. We also propose to use 1ms as the cutoff between the movable fraction and the non-movable fluid fraction within rock matrix (**Figure 44**).

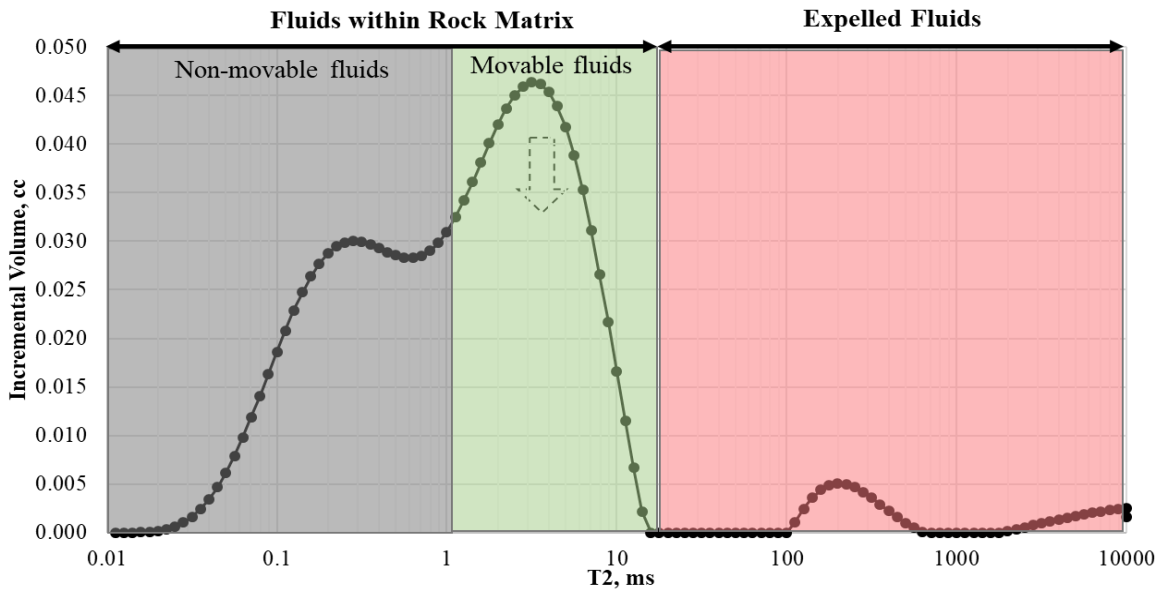

Figure 44. Proposed schematic for different fluid fractions observed under NMR spectroscopy during huff-n-puff. Non-movable fluid within rock matrix, with T_2 less than 1ms (gray). Movable/recoverable fluid but still residing within rock matrix, 1ms $<T_2 <$ 20ms (green). Expelled HC, from rock matrix, with T_2 greater than 20ms (red).

Figure 45 presents the NMR response of HCs within rock sample **C-1**(**Table 5**). NMR signal of HCs within rock matrix (gray + green fractions) was plotted as function of time. For this experiment, four cycles of huff-n-puff were completed before reaching the RF plateau. During each cycle, NMR volume increased during the injection, implying mobilization of a heavy fraction of HC. NMR volume slowly decreased as HC was expelled from matrix. Finally, when gauge pressure dropped below 1250psi (about CO_2 supercritical pressure at 95^{o}F), observable NMR volume dramatically decreases; this effect was not due to expelled HC, but the solvent gases escape

made a heavy fraction of HCs immobile, hence invisible under NMR. In fact, NMR volume of the following cycle after gases being re-injected, would recover to the same magnitude.

Due to the mobilization of HC when solvent gases were injected, a fraction of heavy HCs became detectable with NMR spectroscopy. Therefore, the NMR volume at 5000 psi during the first injection cycle should be considered as the actual maximum HC, V_{max}. The offset between NMR volume during the test and V_{max} is incremental recovery.

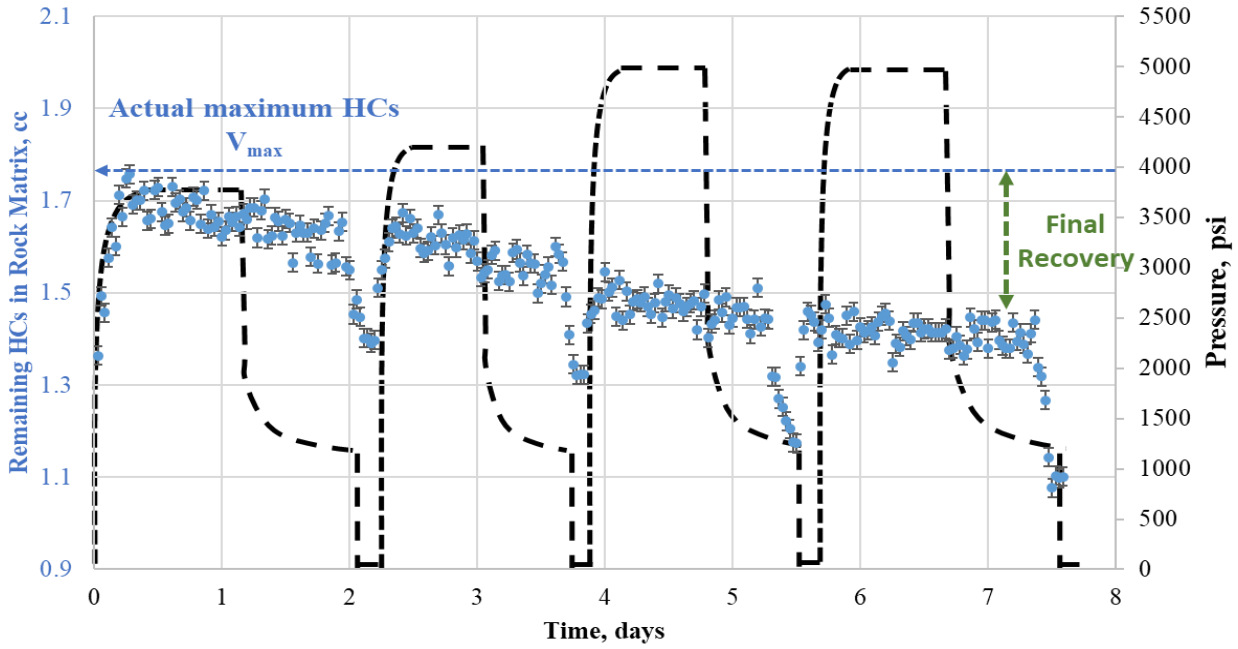

Figure 45. Huff-n-puff experiment with 4 cycles, for sample **C-1**. NMR signal of HC within rock matrix was plotted as function of time. During each cycle, NMR volume increased during the injection, implying mobilization of a heavy fraction of HC; NMR volume slowly decreased as HCs were expelled from matrix; finally, when gauge pressure dropped below 1250psi (critical condition of injected CO_2), and HC volume quickly dropped due to the solvent gases escape made a heavy fraction of HCs immobile, hence invisible under NMR. Pressure profile is also plotted as dash black line.

Figure 46 plotted **C-1** recovery profile, which is the offset between NMR volume during huff-n-puff experiment and the actual maximum *in situ* HC, i.e. V_{max}. In this plot, we ignore the data when pressure is below 1250psi. The final RF is 17.5%, compared to the maximum RF for the crushed sample (6.7-8mm) at the same test condition of 53%.

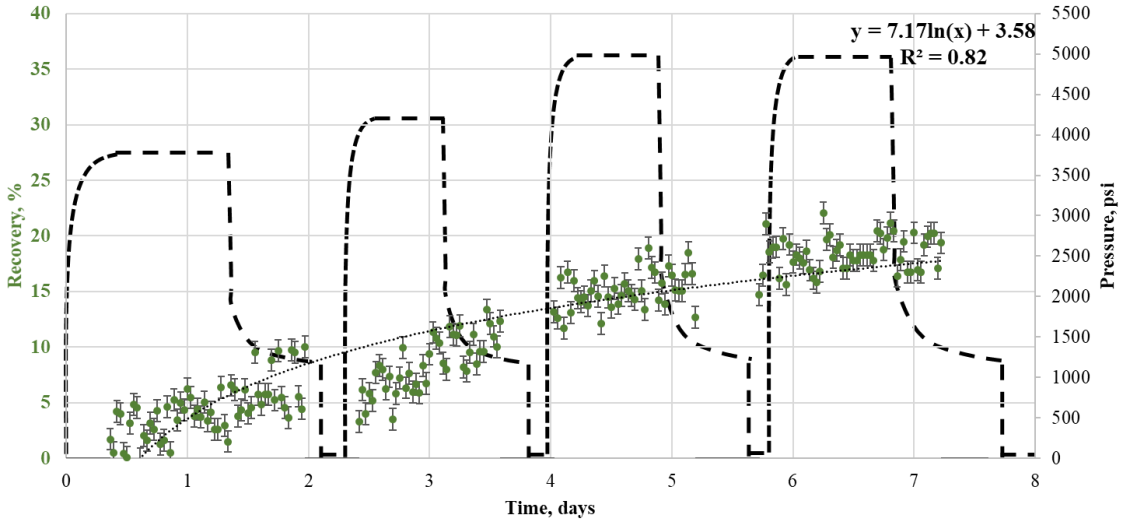

Figure 46. Recovery and pressure (dashed line) profile of sample **C-1** throughout 4-cycles huff-n-puff. The final RF is 17.5%, much lower than RF measured on the crushed sample of 53%.

Following the same approach, we measured the recovery trends (**Figure 47**) for all four samples (**Table 5**). Huff-n-puff cycles were continuously repeated until reaching an RF plateau. In general, we observed non-preserved samples yield higher final RFs. This can be the consequence of the difference in sample microstructure (crack density) or/and the non-preserved condition allows more internal surface exposed due to fluid escape. Overall, for plug tests, both preserve samples yield RFs not greater than 35%, across nearly 10 days of continuous huff-n-puff process.

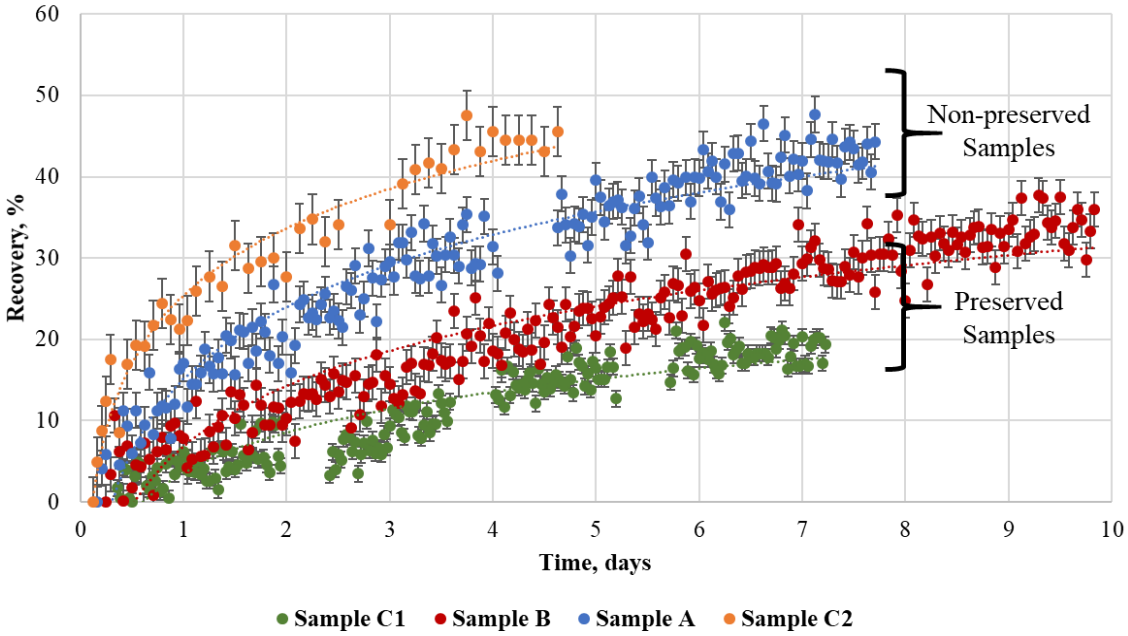

Figure 47. Huff-n-puff recovery trends for 4 samples after plug tests. In general, non-preserved samples yield greater RFs. We hypothesize with less *in situ* fluids, non-preserved samples had higher air-filled porosity, and then more exposed surface area between remaining HCs and injection gas.

While T_2 cumulative volume measurements are useful in monitoring recovery during EOR experiments, T_2 spectra provide useful insights about the dynamic interaction between the oil and gas molecules within rock matrix. Previously, in **Figure 44,** we propose to differentiate three different fluid fractions using incremental T_2 data:

1) Non-movable fluids within rock matrix: this can be fluids trapped inside small pores, or high viscosity HC components, or the combination of both. NMR amplitude associated with this fraction does not change throughout EOR experiments.

2) Movable fluid within rock matrix: this is the dynamic fraction of overall HC, which can be mobilized by gas injection. During huff-n-puff experiments, due to mass transport mechanisms

(diffusion and advection), HC components will be expelled from the rock matrix, in exchange for the injected gas molecules.

3) Expelled HCs: this is the HC fraction originally residing in rock matrix, but later interacted with injection solvent and transported out of the matrix. NMR amplitude of expelled HC is analogous to the loss of NMR amplitude associated with the movable fluid fraction within rock matrix during huff-n-puff process.

Figure 48 shows T_2 spectra of sample **A** during an EOR soaking phase. We observed the continuous reduction of NMR signal for movable fluid fraction within matrix, spontaneously with the increasing of NMR signal for expelled fluid fraction.

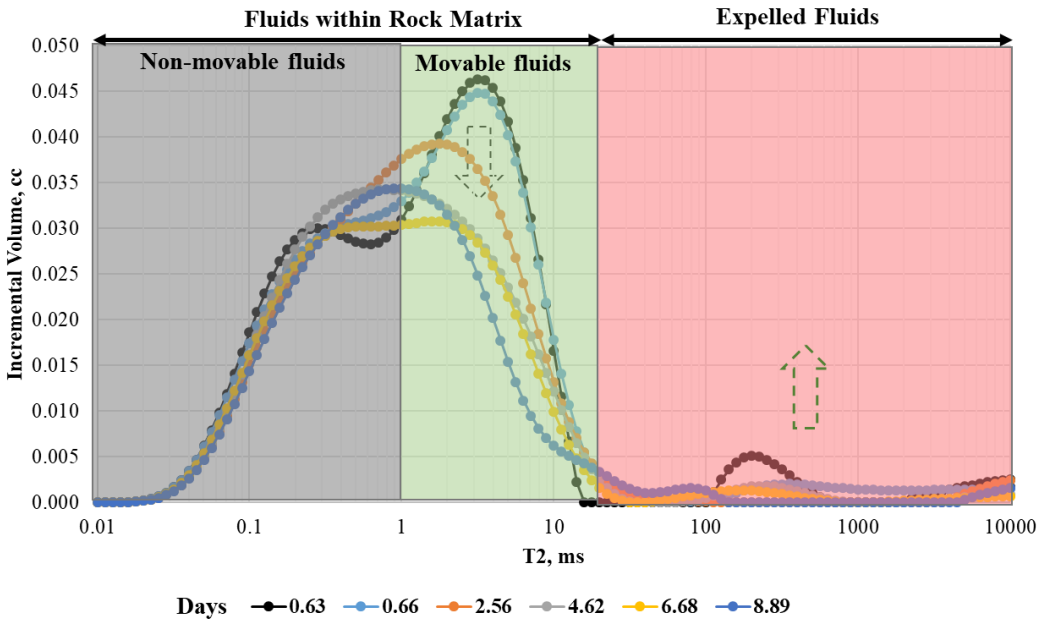

Figure 48. T_2 spectra of sample **A** during huff-n-puff process. Recoverable HCs gradually move from the movable fluid region to the expelled fluid region. Gray area is for non-movable fluid within rock matrix, green area is for movable fluid within rock matrix, and red area is for expelled fluid out of rock matrix.

There different fluid fractions with distinctive behaviors are presented in **Figure 49**, in which the non-movable fraction does not change, movable fluid fraction continuously decreases, and

expelled fluid volume increases along injection/soaking time for each cycle. However, incremental recovery decreases in subsequent cycles.

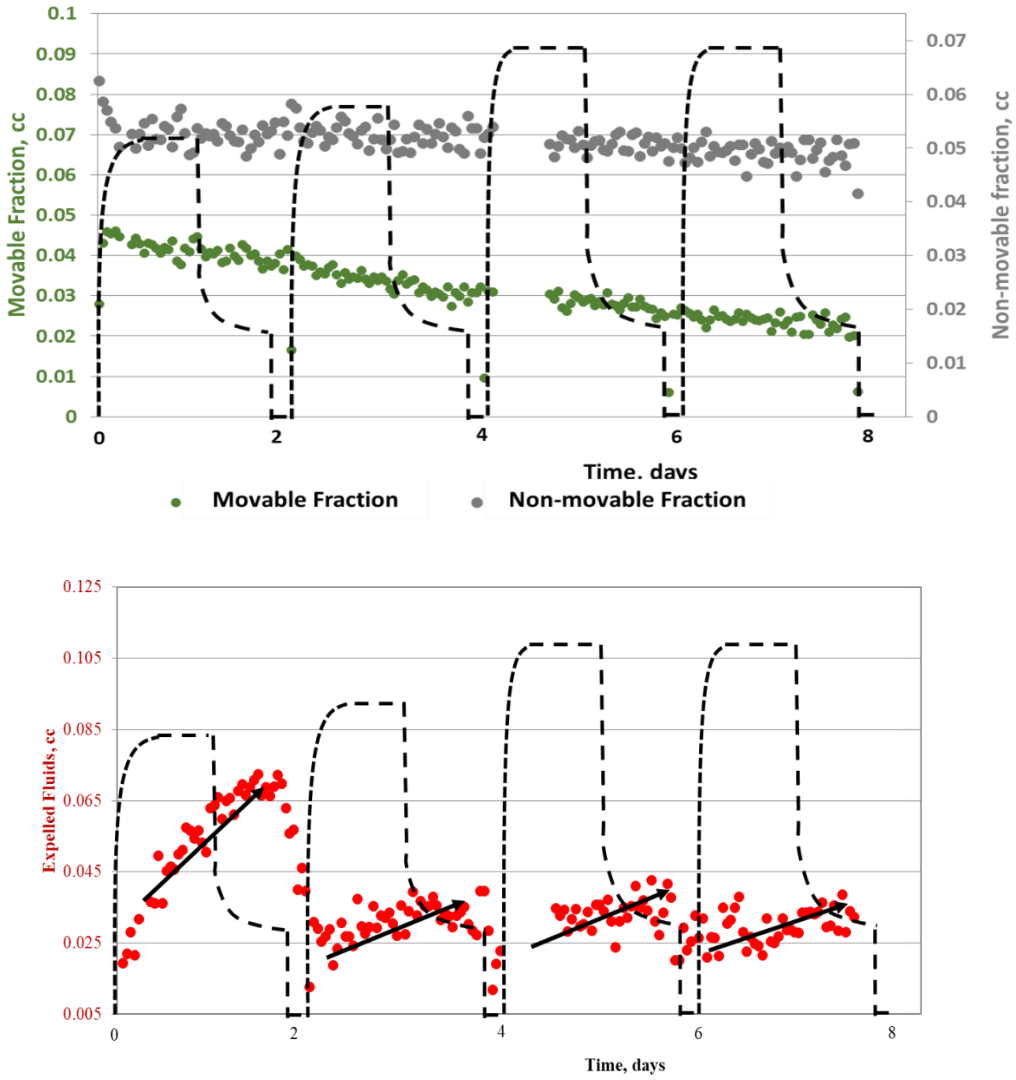

Figure 49. Behaviors of three different fluid fractions defined by their T_2 relaxation responses. During the EOR process, the non-movable fraction does not change, movable fluid fraction continuously decreases, and expelled fluid volume increases with injection/soaking time for each cycle. Color labels correspond to **Figure 48**: green and gray data represent movable and immovable HC fraction, respectively; these fractions reside inside rock matrix at the investigation time. Red data represent expelled HCs during the huff-n-puff.

2. Transmission Infrared Spectroscopy Measurements on Expelled Fluids

Introduction

Infrared spectroscopy (IR) has been applied extensively to characterize various phases of materials including solid, liquid, and gaseous. In the oil and gas industry, this spectral analysis had been employed to measure mineralogy (Harville and Freeman, 1988; Sondergeld and Rai, 1993; Herron et al, 1997 and Ballard, 2007) and reservoir fluid composition (Livanos et al., 2016). Typically, all these measurements were performed under ambient or low-pressure conditions. For our objective to monitor the expelled fluids during huff-n-puff in shale, high-pressure IR cells with transparent IR windows (Zinc Selenium for maximum 2500 psi and Sapphire for maximum 5000 psi) were installed in line with rock sample holder to capture flow-through fluid signal. Thermo-Scientific Nicolet 6700® FTIR spectrometer (wavenumber ranges 600–4000cm^{-1}) was used to continuously measure and analyze fluid signals. A schematic of the experimental set up is presented in **Figure 50**.

During the experiments, the IR spectrometer captures the interactive exchange between injection gases and oil molecules outside rock matrix. It complements the NMR measurements dedicated to record the alteration within the rock matrix.

Fourier Transform Infrared Spectroscopy (FTIR) Calibration

Throughout the huff-n-puff process, the dynamic change in fluid composition is due to the exchange of oil and gas molecules. A single infrared beam focused through the transparent IR windows is used to capture IR absorbance intensity, which is due to the vibration of gas molecules between IR windows. As long as the monitored molecules are not diatomic gasses; they will have

characteristic signature vibrational bands. For example, CO_2 has a major bending band at 2000-2250cm^{-1}, methane has its signature peak at 3106cm^{-1} (**Figure 51**); and different alkane molecules will vibrate at the aliphatic stretching band of 2800-3000cm^{-1} (Nistchem Webbook)

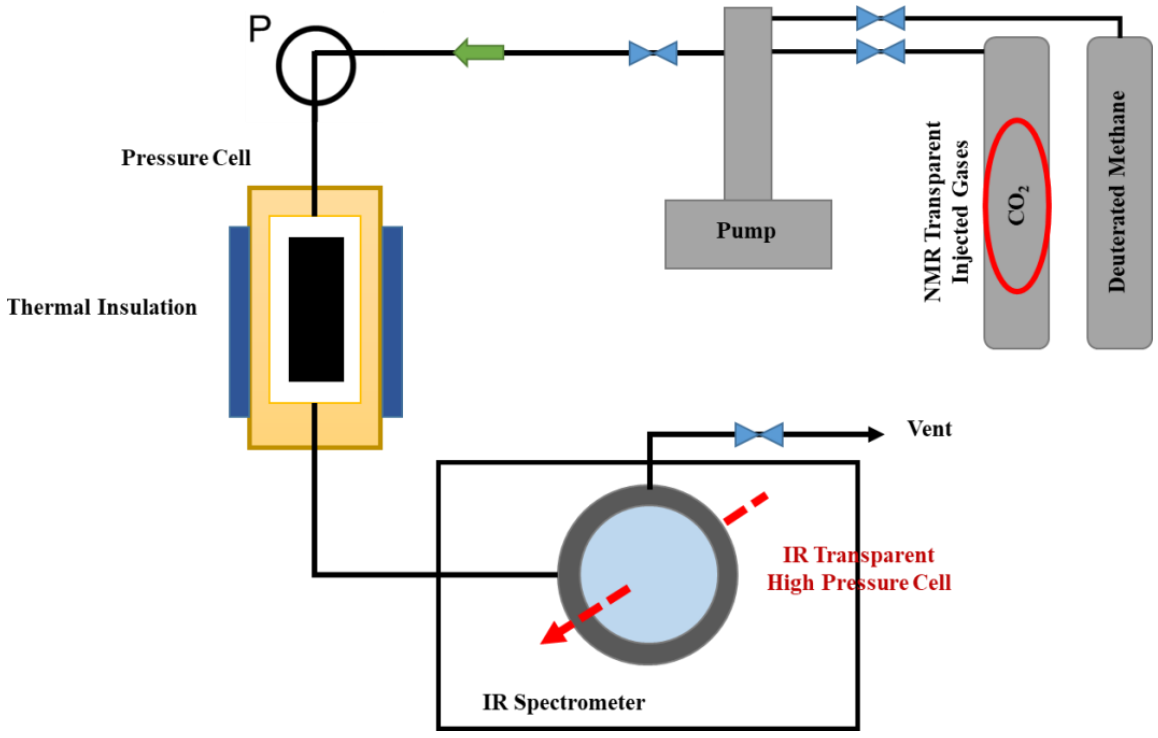

Figure 50. Experimental apparatus, in which porous media was filled with nitrogen for 24 hours, then methane was diffused through the porous media when the zero-displacement valve was opened. A mercury displacement pump was used to keep the system under constant pore pressure throughout the diffusion process. This configuration allowed dynamic monitoring of processes without requiring physical sampling which affects the pressure gradient and hence diffusion.

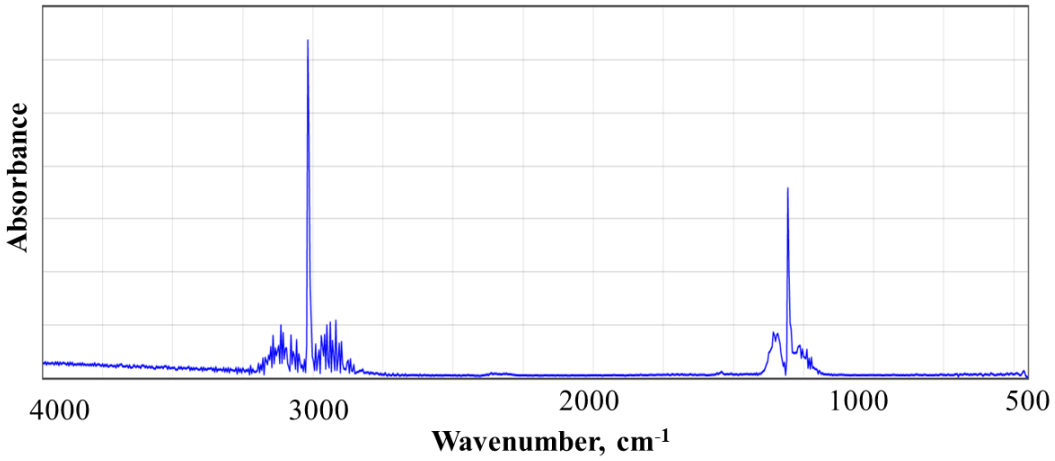

Figure 51. Mid-range FTIR absorbance spectrum of methane. The main absorbance range is from 2800-3100cm^{-1}.

Although all alkane gasses (beside methane) have the same major vibration band of 2800-3000cm^{-1}, the length of their carbon chain has negative relationship with the CH_3:CH_2 functional group ratio. In other words, when expelled HCs become heavier and heavier, greater CH_2 intensity and lower CH_3 intensity would be observed. **Figures 52** and **53** illustrate the relationship between aliphatic carbon chain length versus CH_2 and CH_3 peak intensities.

Beer-Lambert Law (**Equation 1**) describes the linear relationship between IR absorbance intensity and gas concentration:

$$A = l \sum_{i=1}^{N} \epsilon_i \, c_i \quad (1)$$

where A is absorbance, l is the path length of the light beam through IR transparent windows, ϵ_i the absorptivity of each gas component at a particular pressure and temperature, and c_i is the concentration of each gas component within the gaseous phase.

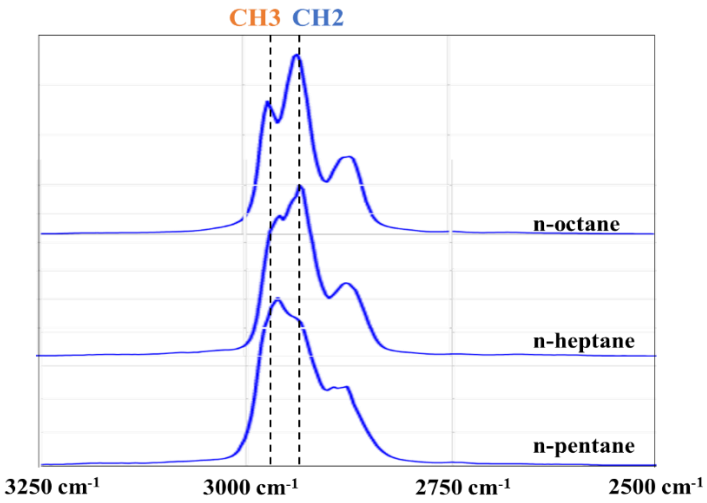

Figure 52. Mid-range FTIR absorbance spectrum (Nistchem Webbook) of alkane molecules. The length of their carbon chain has negative relationship to the CH_3:CH_2 functional group ratio.

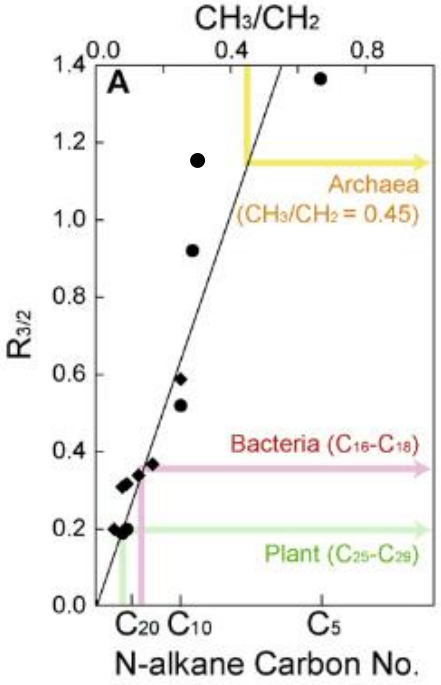

Figure 53. Relationship between CH_3:CH_2 ($R_{3/2}$) IR functional group ratio and ratio of molecular CH_3/CH_2 for n-alkanes standard samples (C_5-C_{40}). CH_3:CH_2 IR functional group ratio can be converted to carbon chain length or apparent recovered HCs heaviness (Nistchem Webbook and Igisu et al., 2009).

Infrared Expelled Fluid Monitoring Results

The IR expelled fluid monitoring experiment was performed independently from previous NMR tests. The injection gas was CO_2. The pre-estimated MMP for the oil associated with this rock sample is 2500 psi. There was only one major huff-n-puff cycle in this test, including one injection phase and four production phases. The first three drawdown steps had different holding times while the production pressure was kept above MMP; the last production step maintained the production pressure below MMP. **Figure 54** presents the absorbance intensity of CH_2 and CH_3 peaks, which belong to the stretching absorbance band of the expelled HCs during the huff-n-puff experiment. Even with the interference of four different drawdowns, we observe that either CH_2 or CH_3 absorbance intensities just followed the same increasing trends, which developed during the injection/soaking phase.

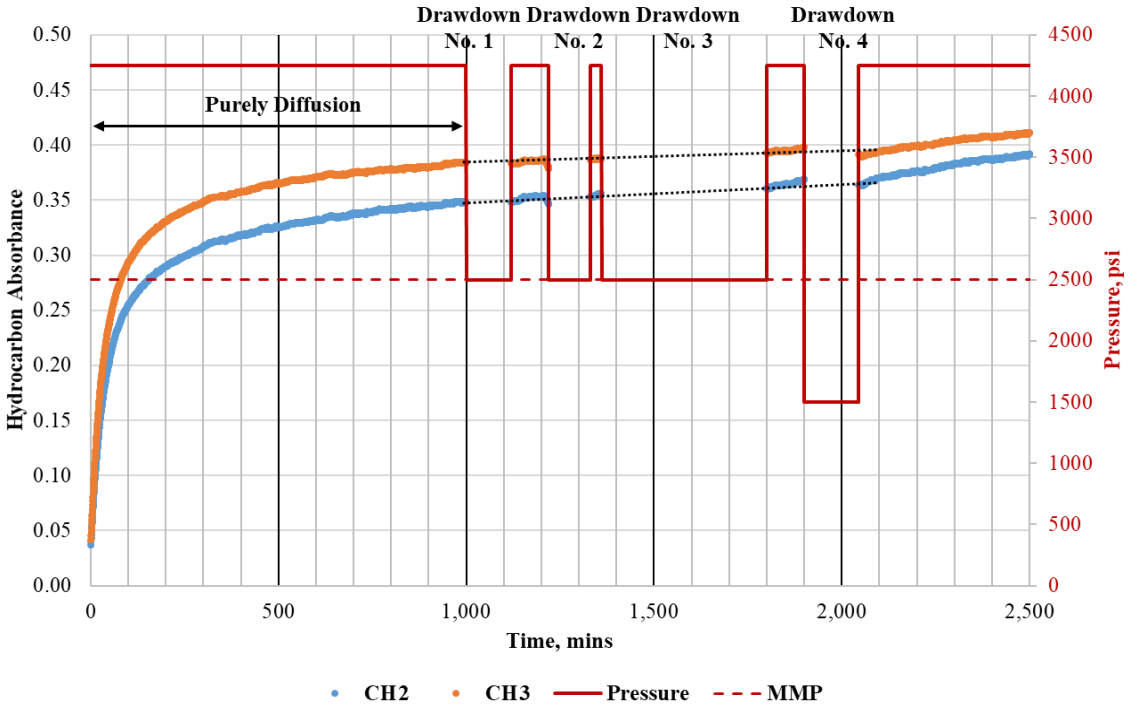

Figure 54. CH_2 (blue) and CH_3 (orange) apparent peak intensities for the expelled fluids during a huff-n-puff experiment (Sample **C1**). Even with the interference of four different drawdowns, we observe that both CH_2 and CH_3 absorbance intensities just continue the same increasing trends, which have developed from the injection/soaking phase, suggesting that the produced HCs were getting heavier.

As the ratio of CH_2:CH_3 IR absorbance can be correlated to the average carbon chain length, CH_2:CH_3 profile can help to evaluate the general composition of expelled HCs. As observed, the ratio increased as the function of time throughout the injection step and four drawdown steps, suggesting that the produced HCs were getting heavier and heavier (**Figure 55**). As discussed in the next section, if diffusion is a major mass transport mechanism, a HC molecule with higher mass would be exchanged with injection gas molecules at a slower diffusion rate; which is consistent with the observation.

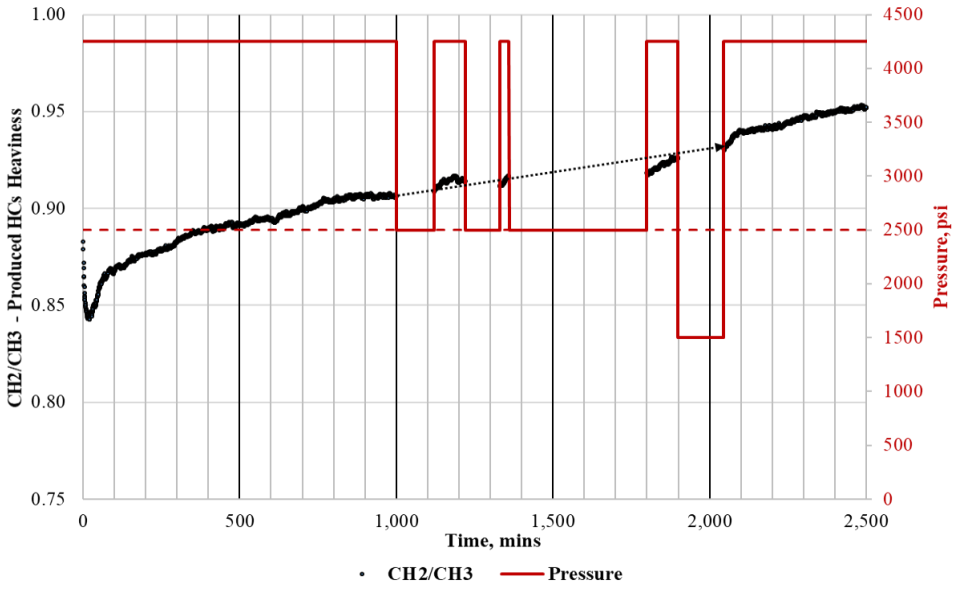

Figure 55. CH_2:CH_3 IR absorbance ratio (from apparent peak intensities) increased during a huff-n-puff cycle, suggesting produced HCs were getting heavier. The crimson dash line represents MMP value.

Results and Discussions

Two newly designed experiments were designed to evaluate mass transport mechanisms during a huff-n-puff process. While NMR measurements monitored dynamic changes of HCs within the rock matrix, IR measurements provided observations of expelled fluid composition as function of time. The recovery behavior during different phases of a complete huff-n-puff cycle, reveals the relative contributions between diffusion ($\Delta P \leq 0$, associated with the injection or the soaking phases) and advection ($\Delta P > 0$, associated with the production phase). It is important to mention that the observed relative contributions between these two mechanisms could be governed by the experimental configurations, such as applied stresses, or test-cell dead volume.

1. Role of Diffusion in Mass Transport in Shales

From NMR real time monitoring experiments, we observed the recovery trends for four tight shale plug samples. Although the final RF is different for each sample, one common behavior is that the recovery tendency during drawdowns (or production phases) follow the recovery tendency during gas injection (or soaking phases) (see **Figure 56**). One can argue that during drawdown, advection or viscous flow should be partially responsible for oil recovery, with a positive pressure gradient outward from the rock matrix. However, it is obvious that during injection or soaking phases, with a negative or zero pressure gradient outward rock matrix, oil recovery must be due to mutual oil-gas diffusion. During the production phases, both diffusion and advection contribute to the recovery, which supposedly results in a faster recovery trend; however, the fact that both recovery trends between injection phases and production phases are similar, suggests that for the tested samples, diffusion is the more dominant mass transport mechanism.

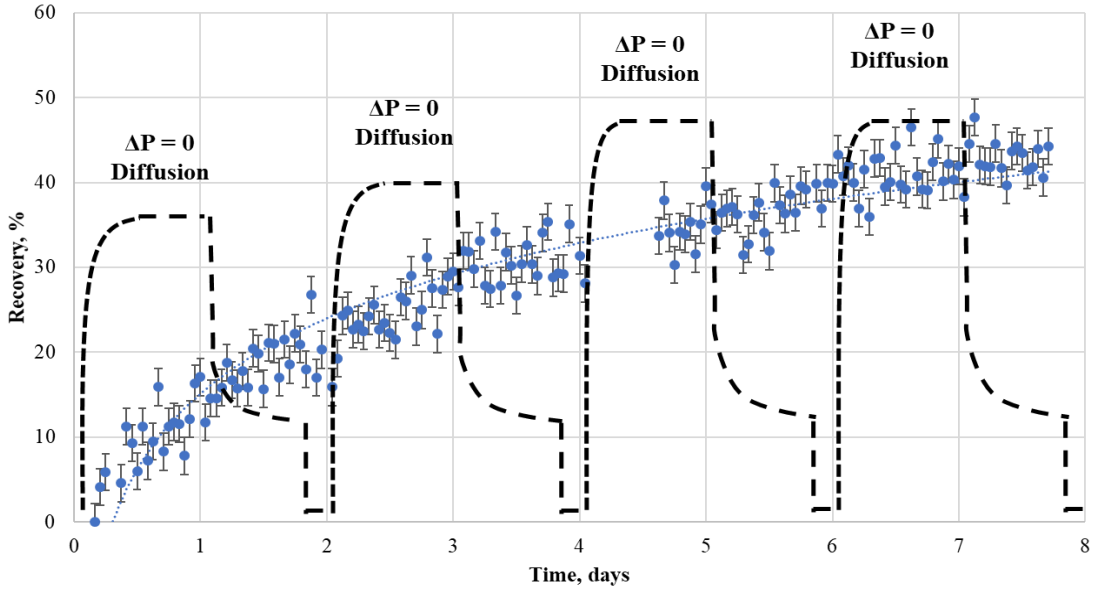

Figure 56. Huff-n-puff recovery trend of sample A with the pressure profile (black dash line). HCs expelled from rock matrix during injection and soaking periods ($\Delta P \leq 0$), suggesting diffusion plays an important role in recovery in tight formations. Moreover, the recovery trend during drawdowns ($\Delta P > 0$) is similar to the recovery trend during injection and soaking steps. Porosity measurement on this sample using pressure decay (HPP), confirms at no confinement, 24 hours of injection time is sufficient to achieve pressure equilibrium.

In **Figure 54**, the HC IR absorbance profile, also shows a similar trend in expelled fluids between the injection steps and the drawdown steps. From both independent experiments, one monitoring remaining HCs within rock matrix (NMR) and another monitoring expelled HC content (IR), confirm the importance of diffusion in nano-porous transport.

If diffusion is one of major recovery mechanism in tight rocks, the following phenomena should be observed. Some of these have been confirmed within this study:

- Expelled fluids get heavier due to the slower mutual diffusivity between injection gasses and heavy HCs components (see **Figure 55**). The molecular diffusivity in the gas phase can be computed with the Sigmund **(**1976**)** correlation.
- Rock specimens with greater crack densities, or higher internal surface areas will yield higher recovery. Crack density is a function of rock matrix properties and applied stress conditions, past and present. **Figure 57** shows the difference in final RF between two preserved Eagle Ford samples. Sample **C-2** has much higher crack density then sample **C-1**, (confirmed by CT-scanning images) and has a much higher RF (45% versus 17.5%) for shorter huff-n-puff time (4.75 days versus 7.5 days.) Note huff-n-puff experiments were performed on these sample without any confinement stress.

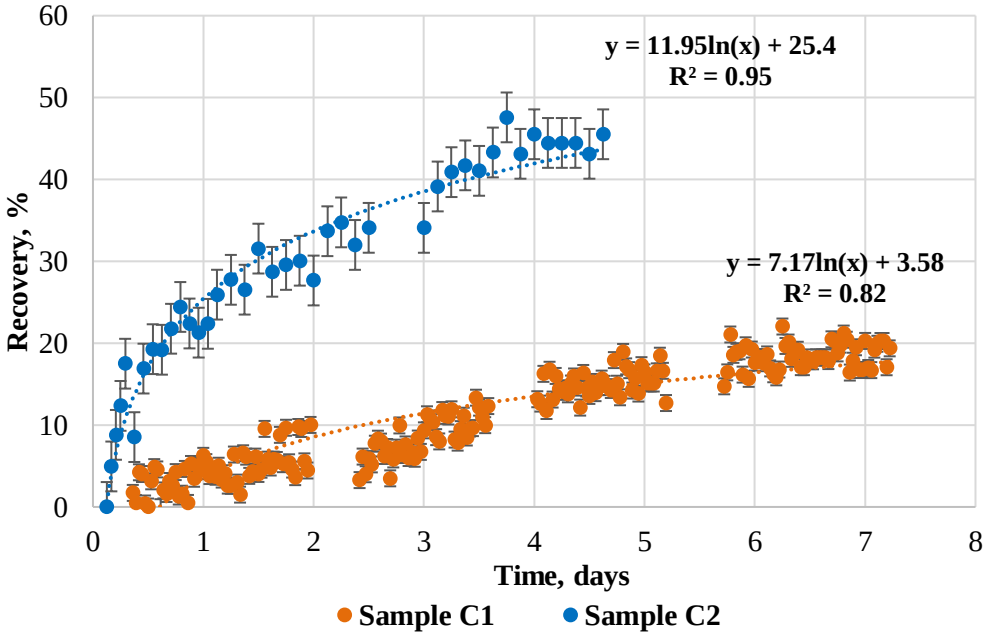

a)

b)

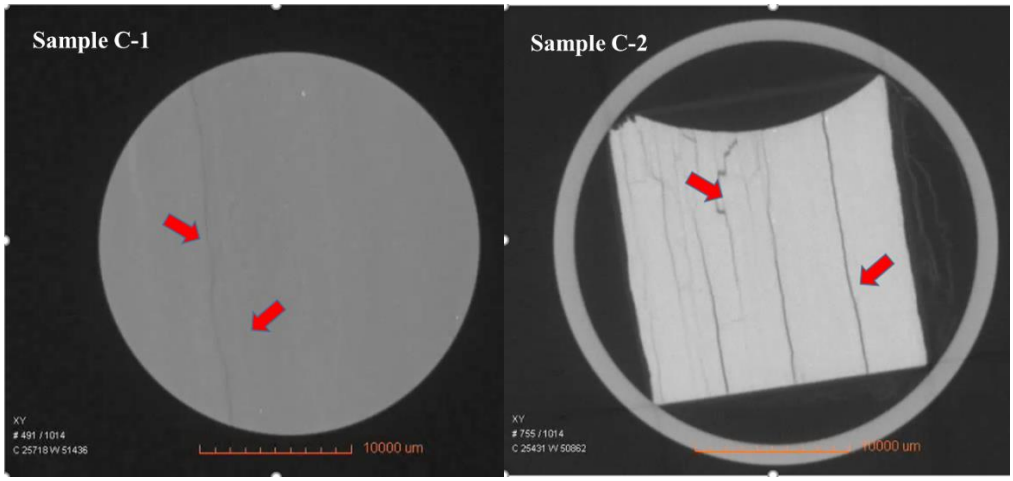

Figure 57. The difference in recovery trends between Eagle Ford sample **C-1** and sample **C-2** (a). Sample **C-2** with higher crack density yields a better RF after a shorter experimental time. (b) CT-scanning images of two samples with identified cracks labeled with red arrows. However, it is difficult to distinguish between natural cracks or induced cracks during sample recovery and/or machining.

As mentioned above, surface area is one of the most important factors governing the efficiency of gas-oil diffusion. Surface area, equivalently crack density, is a function of not only rock matrix but also applied effective stress. To demonstrate the impact of confinement on recovery in shales, we performed a comparison experiment. Utilizing the same experimental apparatus shown in **Figure 37**, two EOR tests were run: one with confinement – the effective stress is of 1750psi and another one without confinement. Both tests were performed on rock sample B (**Table 5**), with the injection pressure of 3750psi, i.e., 1000psi above MMP between reservoir oil and CO_2, and the temperature of 35ºC. **Figure 58** illustrates the difference in test configurations. There was only one injection plus one soaking cycle. The results are presented in **Figure 59**, as the volume of remaining HCs within rock matrixes decreased throughout the tests. Without the confinement, the final RF is much higher, 30% versus 5% RF with effective stress applied. 5% RF seems to be a

pessimistic number for laboratory EOR results; however, shale primary recovery usually ranges from 3-10%. This 5% recovery from huff-n-puff is of the same magnitude as primary production (Hoffman, 2018).

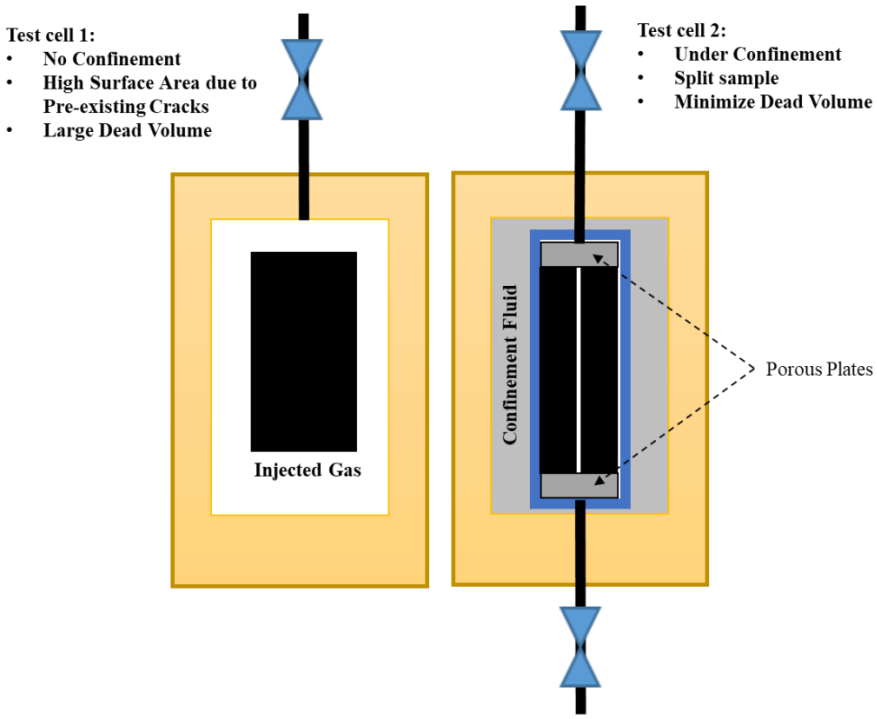

Figure 58. The comparison of experimental configurations to evaluate the impact of confinement on EOR efficiency in shale. With effective stress applied, a fraction of cracks within rock matrix will close; this leads to a reduced surface area, increased tortuosity and a decrease in diffusion processes. Note for test cell 1, with no confinement, gas was injected into the matrix from all directions.

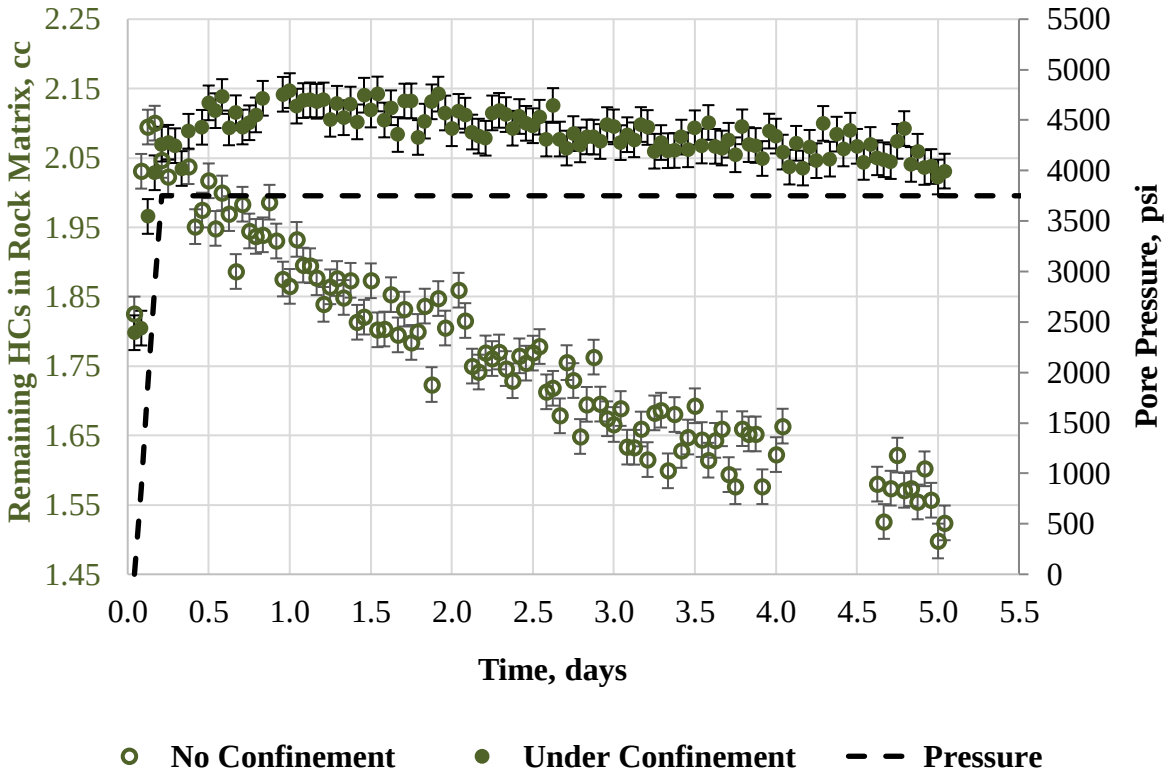

Figure 59. The profiles of pore pressure and remaining HCs monitored by NMR spectroscopy. Without confinement, HCs are expelled quickly from the rock sample; final RF = 30%. With applied confinement, HCs are released slowly from the matrix; final RF=5%. Pressure profile is plotted as the black dash line.

2. Role of Advection in Mass Transport in Shales

If diffusion is the sole mass transport mechanism in shale EOR, we should not observe the impact of different injection pressures, respective to MMP, on oil recovery, especially on crushed samples. However, **Figure 28** clearly shows how final RF is limited when gasses were injected below MMP. To demonstrate the contribution of advection in shale EOR, we performed an experiment, in which four identical 1" diameter by ½" thick Eagle Ford (**EF-1**) rock discs were stacked together, constituting a 2" length cylindrical compound sample. This joint sample was later placed inside test cell and subjected to a huff-n-puff process. One end of the compound

sample was terminated with a Vicor® end plug; while both injected gases and produced HCs flowed through the other end. **Figure 60** illustrates the experimental configuration.

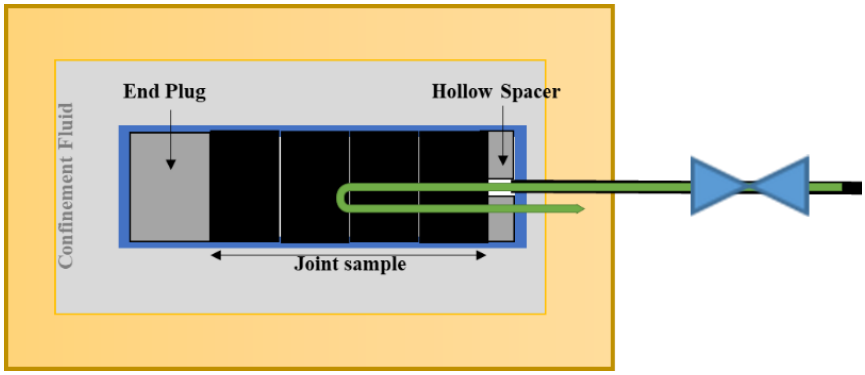

Figure 60. Experimental setup simulating huff-n-puff, with a jointed compound sample composed of 4 identical Eagle Ford rock cores of 1" diameter and 0.5" length. Injected gases and produced HCs flow through the same inlet. The other end of the sample was fitted with a Vicor® end plug.

Since there was no back pressure on the end plug side, during the injection phase, the positive pressure gradient would be pointing to the left (**Figure 60**). This experiment was executed with CO_2 as the injection gas and the soaking time of 12 hours; subsequently, the pressure was quickly decreased to atmospheric for the recovery estimation. **Figure 61 a & b** show the stain of oil recovery through the inlet, and clear evidence of mobilized HCs migrating toward the end plug side, in the same direction of positive pressure gradient. We also plotted the change in HC volume from each disc (**Figure 62**); the two discs near the producing end yielded positive recovery; the other two discs near the end plug yielded negative recovery, i.e. the HC volume increased. The combined RF is 5%.

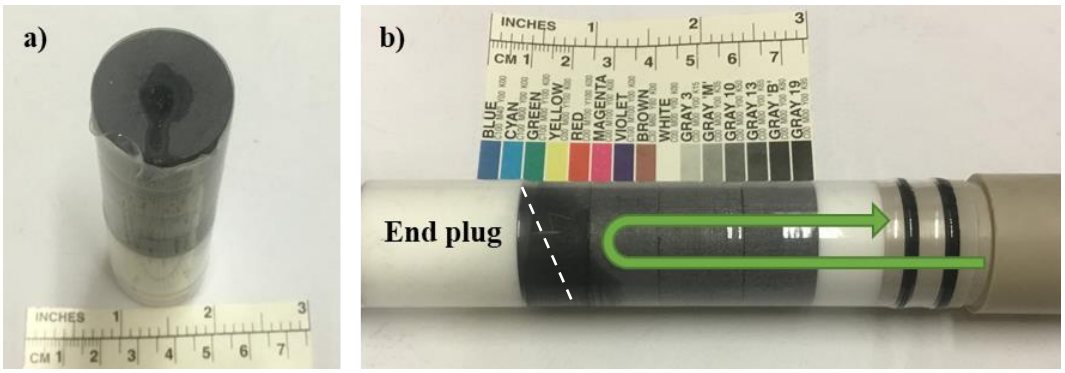

Figure 61. Visual results of the experiment demonstrating the impact of advection on EOR in shale. (a) The stain of oil recovery at the inlet. (b) Clear evidence, indicated by color change, of mobilized HCs migrating toward the end plug side, in the same direction of positive pressure gradient during injection/soaking phase.

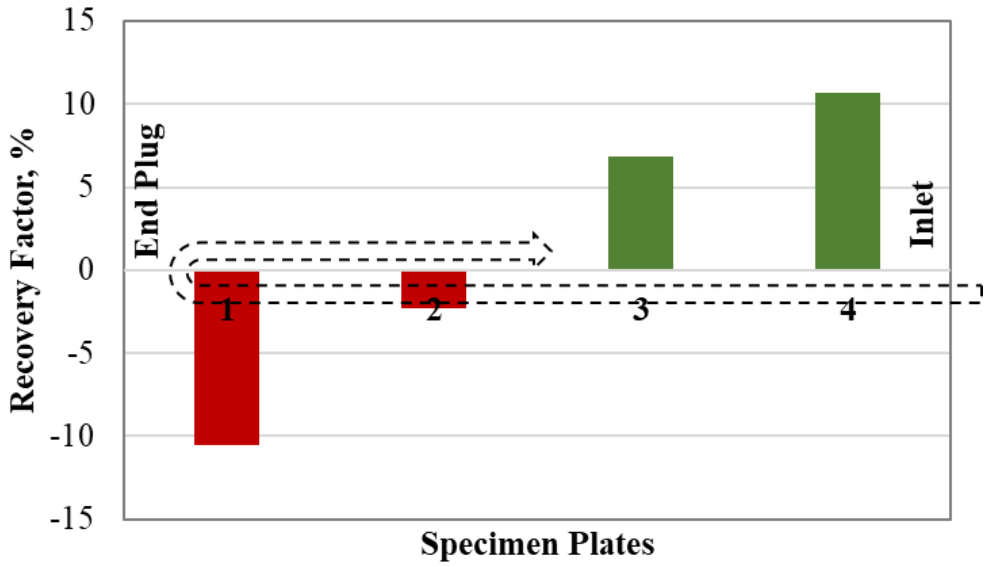

Figure 62. The change in HCs volume for each specimen disc. The two discs near producing end show a positive recovery, the other two near the end plug show negative recoveries. The combined RF is about 5%. It is obvious that advection was responsible for mobilizing HCs which followed the positive pressure gradient.

3. Proposed Hybrid Mass Transport Model for Gas Injection Recovery

Reported in the Eagle Ford field pilots (Hoffman, 2018), gases were injected with downhole pressure just below formation breakdown pressure and above MMP. Despite the cost of high-pressure gas compressors (P-max = 10,000psi), higher pressure gas is injected, resulting in higher reservoir hydraulic energy and lower gas-oil interfacial tension. At high pressure faster and deeper gas components are dispersed further into the formation.

During the injection phase, gases must pass from a surface facility into the formation though a continuous conduit, including wellbore, proppant pack in primary fractures, secondary fractures and matrix, respectively. While the pressure transient is determined by permeability, fluid and rock compressibility, and fluid viscosity; the transportation of gas molecules into reservoir fluids is governed by convection processes, which including mutual diffusion and advection/mechanical mixing (**Equation 2**) (Perkins et al., 1965).

$$K_l = \frac{D_o}{F\emptyset} + 0.5 U d_p \sigma \quad (2)$$

In which K$_l$ is the overall dispersion coefficient, the first term is associated with the dispersion by diffusion: D_o is mutual fluid diffusivity, $F\emptyset$ represent tortuosity, the second term is associated with the dispersion by advection/mechanical mixing: U is viscous flow velocity (controlled by permeability), d_p is characteristic pore throat diameter, and σ is porous heterogeneity.

In the wellbore and the proppant packs within primary fractures, due to their 'infinite' conductivity, the overall dispersion coefficient which is about10^{-4} to 10^{-3} m^2/s, is dominated by mechanical mixing, which is 3 to 4 orders of magnitude greater than the mutual diffusion coefficient. The fast mixing process would occur within wellbore and primary fractures. Given

published Eagle Ford reservoir characteristics (see Appendix), we estimated the total injected gas volume is 500,000 reservoir barrels, (Rbbl) (or 80,000 m^3) for 6 months of injection. While the total proppant pore volume, which can be estimated from total proppant mass and average proppant pack porosity (Mittal et al., 2017), ranges from 1200-4200 Rbbl (or 200-800m^3). This means when injected gases reach the secondary fracture network and disperse into formation matrix, the volumetric concentration of C_2-C_{17} components (from oil within proppant pore volume), relative to bulk injected gas would only range from 0.2-0.95vol% (0.05-0.25 mol.%). This level of enrichment is marginal in changing the interaction of injected gas and reservoir fluid. For example**,** **Figure 63** shows the impact of C2+ concentration of injection gases on MMP; decreasing of MMP is observed when C2+ is above 5-10 mol.%

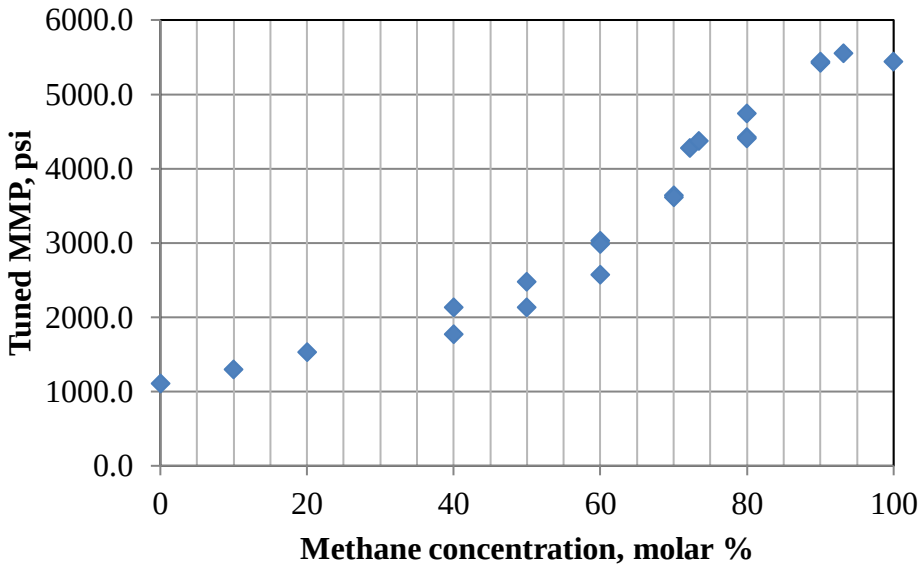

Figure 63. Estimated MMP from EOS versus methane molar concentration in injected solvent gas. Computed MMP values were later verified by measured MMPs at the same test condition with pure methane as injection gas ($C_{methane}$ = 100%) and pure ethane ($C_{methane}$ = 0%).

Assuming reasonable values of fracture height, fracture half-length, and wellbore lateral length (see Appendix), Stimulated Reservoir Volume (SRV) is estimated to be approximately 4,200,000-10,000,000m^3, as a rectangular box around lateral wellbore. With 5% formation porosity, the total formation pore volume that injected gas can occupy at the end of dispersion process is estimated to be 65,000-165,000m^3. Field reported total volume of injected gas after 6 months to "fill up" the reservoir ranges from 40,000-60,000res.m^3. These estimations of total potential invasion pore volume versus total injected gas volume show the injection rate of 2-4 MMscf/day/wellhead is completely possible. However, with better reservoir containment, the injection rate can be reduced, or the injection time can be shorter.

Gas convection can be a strongly time-dependent process (**Figure 64**). Unlike advection dominant in primary fractures, gas dispersion into tight rock matrix is predominately governed by the oil-gas diffusion processes. The advection coefficient is the product of average displacement velocity and average pore-throat of the porous medium; this term is proportionally equivalent to permeability to the power of 3/2. From proppant pack with millidarcy scale permeability to shale matrix with nanodarcy scale permeability, advection term can decrease 6 to 9 orders of magnitude. If chemical diffusion processes dominate in tight rocks, the total convection coefficient would depend on the bulk fluid diffusion coefficient and rock tortuosity. Therefore, how fast gases disperse into oil-filled formation is a function of rock transport characteristics, reservoir fluid composition, injected gas composition, and injection configuration. **Table 6** lists different components of the complete path from surface facility to rock matrix with respect to their conductivities and associated mass transport mechanisms.

Table 6. Components of a complete path from wellbore to rock matrix, and their associated mass transport mechanisms. Shale matrix in general is composed by both microcracks and nanopores. Depending on crack density and applied stress condition (Appendix C), the relative contribution between advection and diffusion can be adjusted.

Flow Component	Conductivity Nature	System	Dominant Mass Transport
Wellbore	High conductivity	Drilling schematic	**Advection**
Primary hydraulic fracture + Proppant pack	Sensitive to stresses and proppant damages	Stimulated Reservoir Volume	**Advection**
Secondary hydraulic fracture	Sensitive to stresses		**Advection**
Rock microcracks	Sensitive to stresses	Rock matrix	**Advection**
Nanoporous matrix	Low compliance pores		**Diffusion**

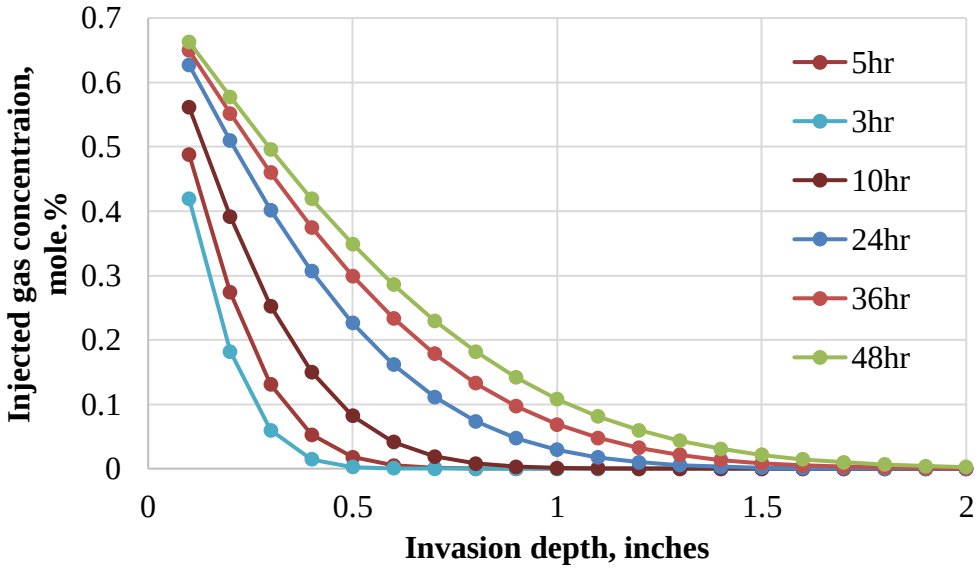

Figure 64. Simulated gas concentration profiles for different injection/soaking periods (for assumed inputs, see APPENDIX). In this simulation, injection pressure is 3500psi (1000psi above MMP), injected gas is CO_2, and rock tortuosity $(\frac{L_{actual}}{L_{apparent}})^2$ is 8.3. These data were used to determine the time scale for an EOR test for 2" long core plug.

With the continuous dispersion of injected gas in oil-filled pores, dominantly due to concentration gradient, formation fluids would 'swell' and be 'expelled' from the matrix. These

physical behaviors simply reflect the counter diffusion flow of oil components into the gas phase. However, for low porosity-low permeability rock, it is unlikely for swollen-oil in individual pores to merge to form a continuous phase. **Figure 65** shows the impact of formation tortuosity characteristic and bulk fluid diffusion coefficient on the volumetric concentration of remaining oil within rock matrix during injection phase, assuming swelled oil is spontaneously expelled from the sample.

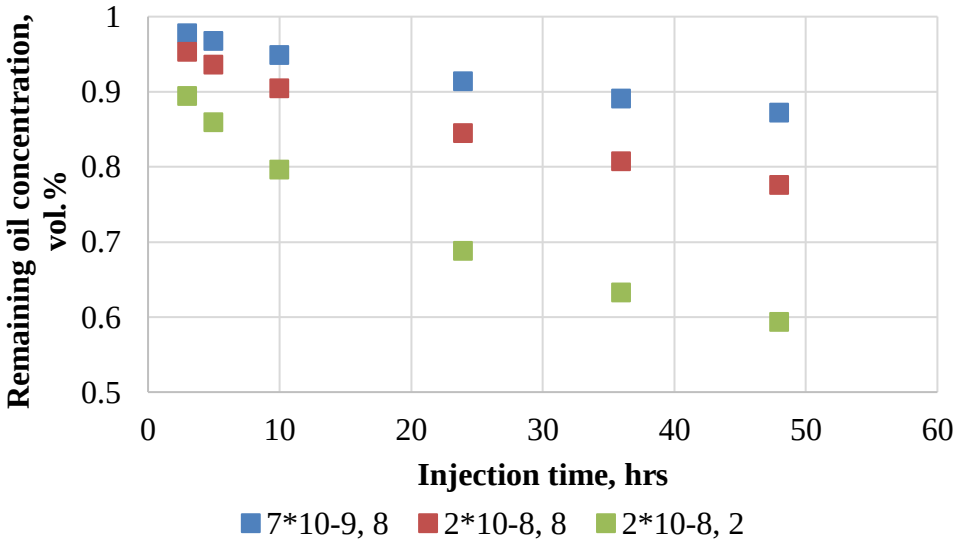

Figure 65. Remaining oil volumetric concentration within rock matrix as a function of time, simulated for a 2" long by 1" diameter core plug test. Note there are two parameters for each legend, the first is bulk fluid diffusion coefficient (in m^2/s), the second is tortuosity. Blue symbols are for tight rock and CO_2 injection. Red symbols are for tight rock and methane injection. Green symbols are for conventional rock with methane injection.

Another important parameter determining the efficiency of gas dispersion during the injection and production phase is the ratio of formation surface area to stimulated reservoir volume; this ratio is tied closely with recovery rate and indicates the effectiveness of hydraulic fracturing processes. Stage spacing and cluster spacing are major elements controlling the level of near

wellbore reservoir stimulation; whereas, the frac-fluid and sand volumes determine the extent of fracture propagation. Depending on reservoir configuration (leak-off rate or mechanical stratigraphy), fracture propagation can be optimized. Raterman et al. (2017) show the fracture count distribution of a stimulated Eagle Ford well, along the lateral wellbore parallel to the simulated wellbore (**Figure 66**). Observation well #1 drilled horizontally closed to stimulated well shows higher fracture frequency, with average fracture spacing of 2ft along the lateral; while observation well #2 drilled vertically close to stimulated well, but further in horizontal distance, shows lower fracture frequency, with average fracture spacing of 4 ft. In other words, the ratio of surface area to simulated volume is spatially dependent. Well #1 also appears to have more uniform fracture distribution along wellbore; well #2 has higher fracture density at the heel but much lower fracture density at its toe.

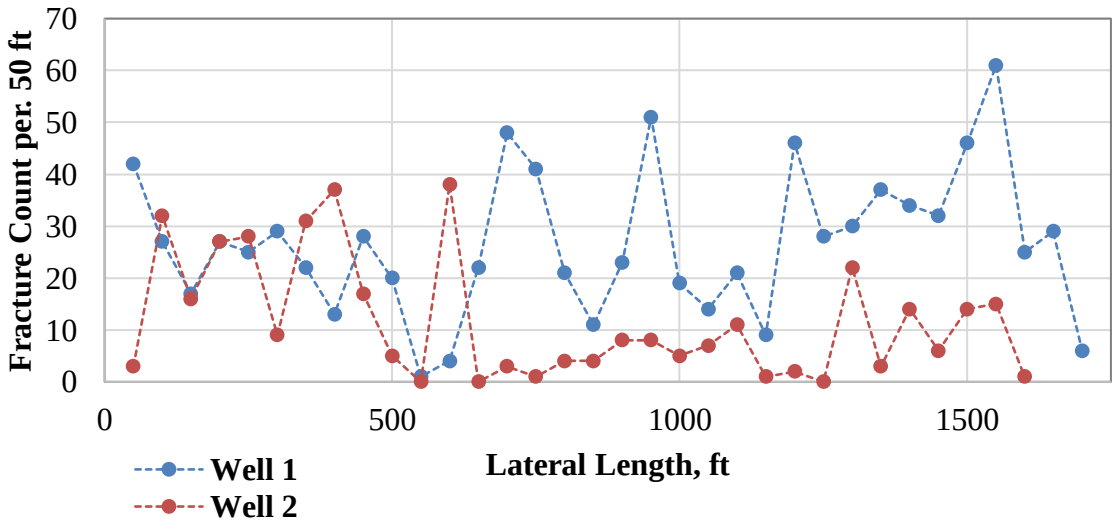

Figure 66. Fracture counts every 50ft or per cluster along nearly 2000ft of lateral wellbore. High fracture density and more uniform fracture distribution were observed in the well which is horizontally closer to the stimulated wellbore.

As presented in Raterman et al. (2017), not all observed fractures are primary fractures. However, secondary fracture networks play a critical role in fluid conductivity. Since gas dispersion is a time-dependent process, dispersion efficiency increases with closely spaced fractures and higher fracture density; after a certain injection period. Although the dispersion/gas mixing efficiency is almost linearly proportional to the depth of invasion (**Figure 67**), the need for optimization of injection/production phases is required; these directly affect the economic value of an EOR project. However, recent studies (Bhoumic et al., 2018; Damani et al., 2018 and Ratzlaff et al., 2019) shows that fracture density varies non-linearly with distance along and away from the main fracture, which suggests that the mixing invasion depth is not linear (**Figure 67)**.

Figures 68 and 69 represent the cumulative and derivative relationship of mixing efficiency as a function of injection time, respectively. According to the plots, for this formation, the time for the injection process to 'fill up' the reservoir should be optimized after 6-7 months; the average mixing efficiency among the two wells is 30 vol.%.

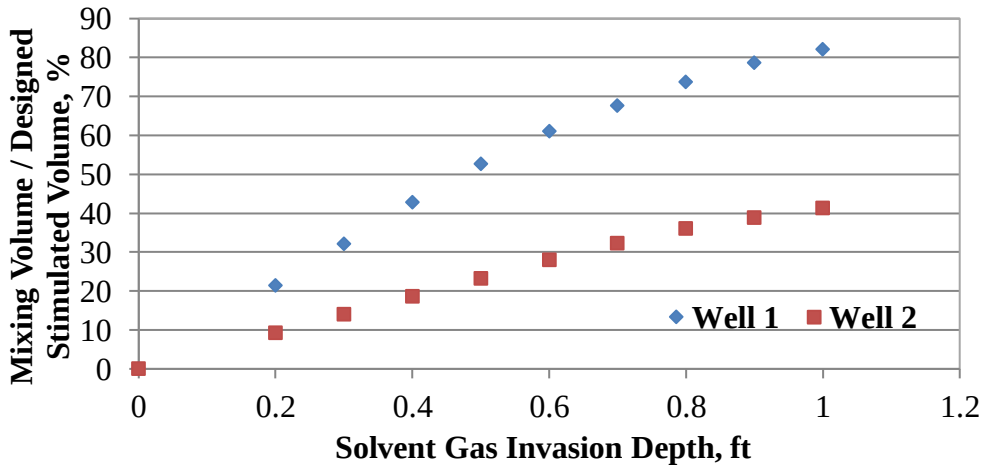

Figure 67. Mixing efficiency as a function of invasion depth. Invasion depth is governed by injection pressure, injection time (which can be optimized), injection gas composition (economically constrained), reservoir fluid and matrix permeability (engineers have no control).

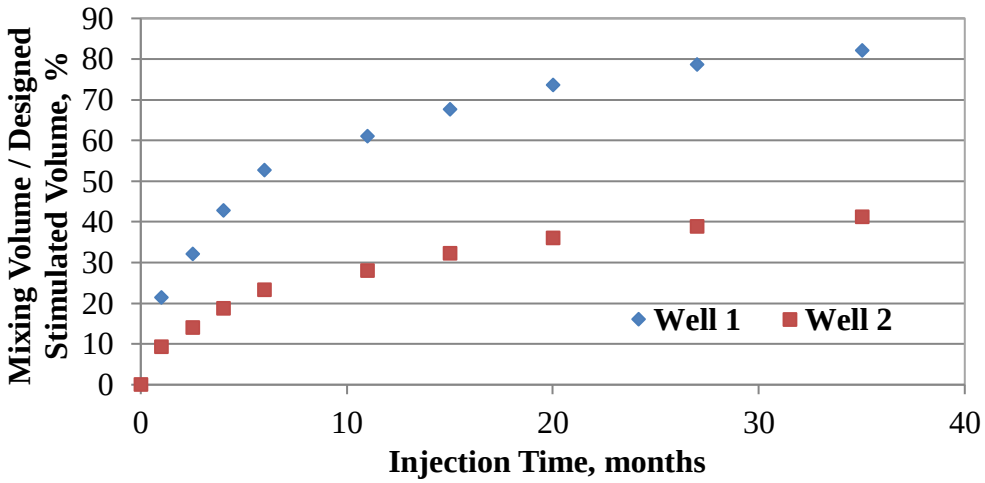

Figure 68. Cumulative mixing efficiency as a function of injection time. The mixing efficiency becomes marginal after a period of injection; after this point, excessive injection time and injection volume are wasteful.

While many researchers consider oil swelling a major mechanism of oil recovery during the huff-n-puff EOR process, I propose that counter diffusion of oil components into gas phase as an alternative approach to describe the recovery process. Theoretically, the oil swelling is the consequence of the gas dispersion into the oil phase. In fact, studies have utilized this phenomenon to back calculate the gas-oil diffusion coefficient see for example, Jamilalahmadi et al. (2006). In general, a single valued swelling factor was reported and used as input to a conventional reservoir simulation. This is not really an unreasonable approach for high permeability-high porosity formations, in which the swelling process swiftly reaches equilibrium. However, modelling reservoir behavior with a single value of swelling factor does not reflect the dynamic aspects of the swelling process in tight formations. Swelling factor is measured in the laboratory, typically for bulk oil; this process is relatively fast. In reality, swelling equilibrium requires longer times when the medium is tortuous. The swelling factor acquired from laboratory measurements should only be considered as an endpoint of the dispersion process.

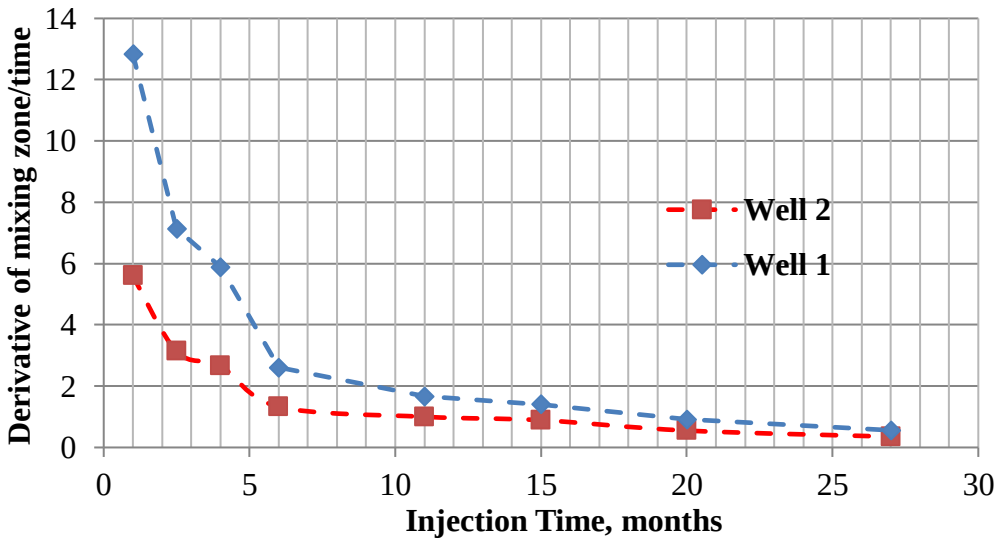

Figure 69. Incremental mixing efficiency as a function of injection time. This plot shows clearly that the 'fill up' reservoir process should be stopped after 6 months. Investigation from EOG Eagle Ford pilot report the first injection cycle lasted 6-6.5 months (Hoffman, 2018).

Another issue with a swelling test is that it should be conducted with various volumetric combinations of bulk oil and injection gas volume. Described by Maxwell-Stefan equation, the diffusion coefficient of a binary mixture is a function of initial relative molecular concentrations; therefore, during the injection process, with the increasing overall gas concentration, the swelling factor should be dynamically varied.

Despite these issues, the swelling factor estimated at the end of the reservoir 'fill-up' process, can be used to quantify the recovery of first cycle if injection time/soaking time are long enough to achieve pseudo-equilibrium. With estimated total SRV pore volume, and total injection gas volume, I estimated oil: gas relative molecular concentration to be 52:48, which results the swelling factor after 6 months of injection of 1.14-1.20. Assuming oil formation volume factor of 3 and estimated reservoir mixing efficiency of 30 vol.%, the calculation of oil recovery after the first cycle is between 17,000-42,000stb. This range of recovery is the same order of magnitude as

the first cycle recovery reported from EOG's pilot after 6 months of injection, which is about 20,000stb per well for 4 wells within this lease. This agreement helps to validate the critical role of chemical diffusion during huff-n-puff for tight formations.

Conclusions

Phase 3 of the EOR study includes newly designed experiments, which focus on addressing fundamental recovery mechanisms during huff-n-puff in shales. These experiments exploit two spectroscopy techniques: NMR with the capability of real-time monitoring of the residual HCs within the rock matrix, and infrared with the capability of real-time evaluation of expelled fluids. The biggest advantage of combining these two techniques is that we can continuously estimate the incremental RF, without removing the rock specimen from a test-cell. In other words, the pressure condition during huff-n-puff are unaltered. This combination of techniques provides a unique means of observing changes during gas injection EOR in shales without altering the environmental conditions:

- Incremental recoveries were observed from both injection-soaking phases (pressure gradient is negative to zero) and production phases (pressure gradient is positive, equivalent to drawdown). This suggests that diffusion is one of the major mass transport mechanisms.
- Recovery behavior during injection-soaking phases and production phases, followed had similar general trends. This suggests, for tested samples, diffusion, indeed, is the dominant drive compared to advection.
- Expelled fluid composition got heavier and heavier during the huff-n-puff experiment, suggesting mutual diffusivity between injection gasses and *in situ* HCs, can be biased toward light component fractions.

- The effect of advection should not be overlooked, especially when there is a high-pressure gradient between the injection pressure and average reservoir pressure after primary recovery. We observed a fraction of HCs was pushed along in the same direction as the pressure gradient, which can hinder the final recovery.

- Within rock matrix, diffusion governs mass transport in nanopores, while advection governs mass transport in microcracks. In field applications, excessive injection pressure above MMP can play a very important role, not in term of gas-reservoir fluids interaction, but in term of crack opening and surface area exposure. This is beneficial for both advection and diffusion processes. Experimental results show, that with lower effective stress or higher injection pressures, huff-n-puff recovery can be improved. We propose to study hysteresis of crack permeability in shales in the future to evaluate how the coupled crack-matrix compressibility of shale samples impacts EOR performance.

IV. Nano-matrix Tortuosity and Mutual Diffusivity Measurements

Motivation and Literature Reviews

Many modelling and theoretical studies have shown that diffusion can be a significant transport mechanism in low-permeability porous media. Understanding the process in tight rocks allows engineers to better predict reservoir performance during both primary production and enhanced recovery. Direct measurement of effective diffusivity in tight rocks is difficult, due to small pore volumes and the lack of techniques to directly monitor the process. Conventional diffusion measurements generally require periodic fluid sampling, which induces a pressure transient and a volume change which change the mass transfer mechanism. We introduced a novel technique to measure tortuosity in nanoporous media by simultaneously monitoring methane versus nitrogen concentrations at high pressure using transmission Infrared Spectroscopy (IR). Also, to complete the estimation of effective diffusion, the bulk fluid diffusion coefficient needs to be measured. In this study, we demonstrate the use of Nuclear Magnetic Resonance (NMR) 1-D imaging to capture the dynamic change of Hydrogen Index (HI) across the interface between two bulk fluids. The experiment was conducted between a Meramec crude oil sample (API =42) and methane; fluid samples were pressurized within an NMR transparent Daedalus™ ZrO_2 pressure cell which can operate at pressures up to 10,000psi. The results provide an oil swelling factor and the concentration profile as a function of both time and distance. These data were fitted with Maxwell-Stefan equation to precisely back calculate the diffusion coefficient between oil and gas samples at high pressure. Accurate estimation of tortuosity and fluid diffusion is critical for the gas injection strategy in a shale formation. Greater tortuosity and smaller fluid diffusion rates lead to longer injection and production times for desirable economic recovery.

1. Mutual Oil-Gas Diffusivity

Recent studies, including simulation (Li et al., 2018), experimentation (Li et al., 2019 and Dang et al., 2019), and production modelling (Cronin et al., 2018), suggest that matrix diffusion is a major mass transport mechanism, along with advection. Advection of flow in porous media is governed by fluid properties (such as viscosity, density, and compressibility) and matrix permeability. Diffusion is governed by fluid diffusivity (either free diffusivity or multi-component diffusivity) and porous media tortuosity. The Sherwood number, Sh, commonly cited in surface science and catalyst studies, represents the ratio of the convective mass rate (include both advective rate and diffusive rate) to the rate of diffusive mass transport (Coutelieris et al., 2002). Within high porosity media, such as conventional rocks, $Sh >> 2$, the impact of advection overpowers the role of diffusion. While in tight rocks, with matrix permeability on the order of nanodarcy, the impact of diffusion is not negligible (Karger et al., 2012) (Appendix B).

With the development of unconventional shale gas and oil, the need to reevaluate these transport mechanisms, especially in nanoporous media, becomes essential. This applies equally for primary production and EOR processes. The understanding of light gas molecule behavior when diffusing into rock matrix filled with reservoir fluids is important in optimizing the efficiency of gas injection.

Along with matrix tortuosity, bulk fluid diffusivity also controls effective diffusion. The molecular diffusivity in the gas phase can be computed with Sigmund's (1976) empirical correlation. In terms of experimentation, this parameter can be estimated via several methods, including monitoring pressure profile while the oil phase contacts the gas phase inside a closed cell (Guo et al., 2009). The drawback of this technique is that pressure is not maintained constant

throughout the measurement. Another approach is monitoring the oil phase swelling while injecting gases at a constant pressure (Jamialahmadi et al., 2016). The swelling data is acquired by tracking the change in elevation of oil-gas interface. However, with the pressure above first contact minimum miscibility pressure (MMP), the interface becomes so vague as to defy precise monitoring. In this study, we propose a new method using NMR 1-D gradient to monitor the dynamic change between oil-gas interface, from which bulk fluid diffusivity can be determined.

1-D Gradient NMR Measurement

a) Experimental Setup and Fluid Samples

For pressurization experiments, we used a Daedalus® cell, made of NMR transparent ZrO_2; the cell can be operated up to 10,000 psi internal pressure. The oil phase was injected into the pressure cell via a downstream port, while the gas phase would be later injected into the cell through the upstream port. The cell was positioned inside the NMR spectrometer, in which the oil-gas interface would be aligned in the middle of the gradient scanning window. The cell inlet was connected to a syringe pump system, which compressed gas from supply cylinders and injected gas into the test cell at a test pressure. The pressure was maintained constant throughout the diffusion process. **Figure 70** illustrates major components of the experimental setup.

NMR gradient profiles were acquired using Oxford 2 MHz GeoSpec™ spectrometers, and Green Imaging LithoMetrix™ software. The magnet temperature was set at 35°C throughout the experiments. The gradient scanning window was set at 7 cm, using double half k-space (DHK) sequence. A new scan was repeated every 1 hour. Dynamic change of hydrogen index (HI) profiles across the oil-gas interface during the diffusion process, allows us to extract bulk diffusion parameters. In this study, the fluid samples included a dead oil from the Meramec formation

(API=42), and the injection gas is methane. **Figure 71** represents a HI profile at the beginning of a 7-days experiment with methane injection pressure of 6000 psi, which is above minimum miscibility pressure (MMP = 4400 psi).

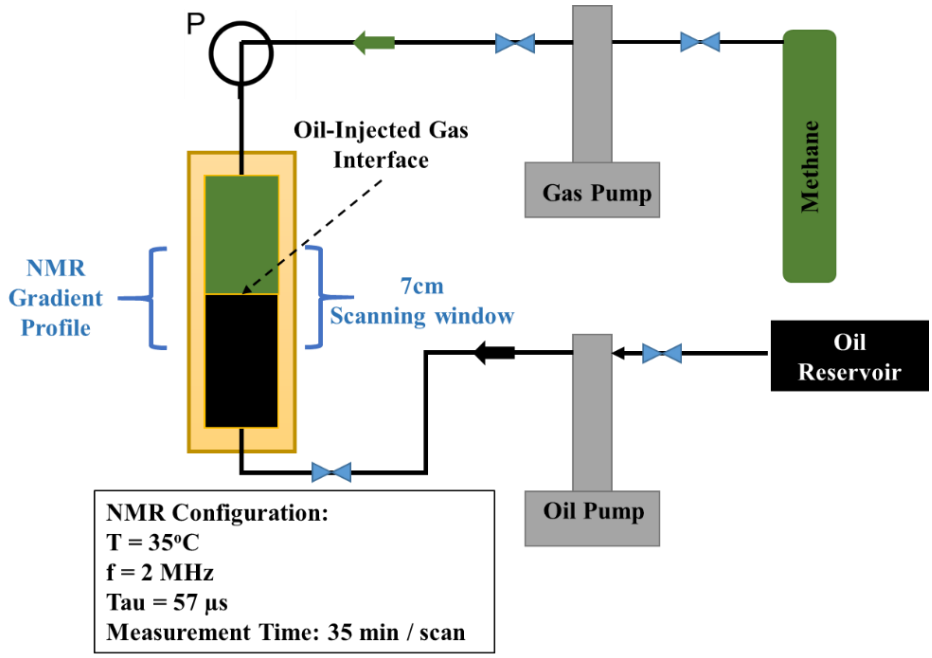

Figure 70. Experimental configuration, including NMR transparent ZrO_2 pressure cell, placed within 2 MHz NMR spectrometer. The spectrometer is fitted with a separate gradient coil. The oil phase was injected from a downstream port; the gas phase was injected through an upstream port, with the pressure controlled by a computer-controlled syringe pump system. The cell was positioned inside the spectrometer, in which the oil-gas interface was in the middle of the gradient window.

b) Experimental Results

With the contrast in HI between the gas and the oil phases, we can monitor the change in elevation of the interface (**Figure 71**). During the diffusion process, during which pressure is maintained constant, methane molecules would diffuse into the oil phase at certain rate. This phenomenon dynamically changes the HI profile of the oil phase as a function of time. **Figure 72** shows HI profile of the oil phase from the beginning of the experiment to its termination, 7 days

later. HI at any point within the oil phase decreases over time, but the reduction rate is different depending on relative position with respect to the oil-gas interface. **Figure 73** shows the effect of methane diffusion on HI trends at four different positions, note the marker colors correspond with the position, labeled in **Figure 72**.

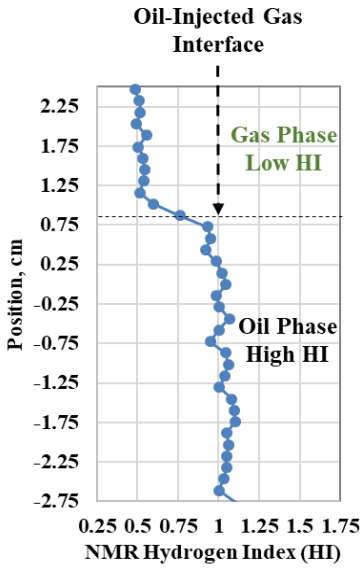

Figure 71. An HI profile across the oil-gas interface. The position values are based on the relative position of the test cell in the NMR scanning window. The contrast in HI between the gas (low value) and the oil (high value) phases, allows determination of the dynamic position of the oil-gas interface during the experiment.

As expected, at the positions closest to the interface, HI decreased at the fastest rate, and quickly approached a constant value, HI_{final}. Moving further away from the interface, HI decreased with gentler slope, but eventually reached the same HI_{final}. HI_{final} is the result of the mixing between original oil molecules and injection gas molecules (methane in this case) at a particular concentration. From the experimental results, this specific concentration can be regarded as the maximum concentration of methane that can diffuse into the oil body; this parameter is a function of pressure and temperature. Using each of these HI trends, the methane diffusion coefficient can

be calculated. However, with the fluctuation in the data due to variations in the NMR signal-to-noise, the integral of HI profile provides a more stable estimate of the diffusivity.

At a position and time, the HI value is the molar averaging between the HI value of the original oil and the HI value of methane at 6000 psi (**Equation 3**). With the known HI value of the original oil, i.e. 1, and known HI value of methane at 6000 psi which is 0.525 (both values can be extracted from the HI profile at the beginning, i.e. at t=0), relative methane concentration can be calculated, then plotted as a function of time. **Figure 74** shows the integral of HI profile (red) and calculated methane molar concentration in the oil phase (blue).

$$HI_{oil\_phase}(t) = (1 - \alpha)HI_{original\_oil} + \alpha HI_{methane@6000psi}$$

$$\alpha\,(t) = \frac{C_{methane}(t)}{C_{methane}(t)+C_{oil}(t)}$$

$$HI_{original\_oil} = 1$$

$$HI_{methane@6000psi} = 0.525$$

(3)

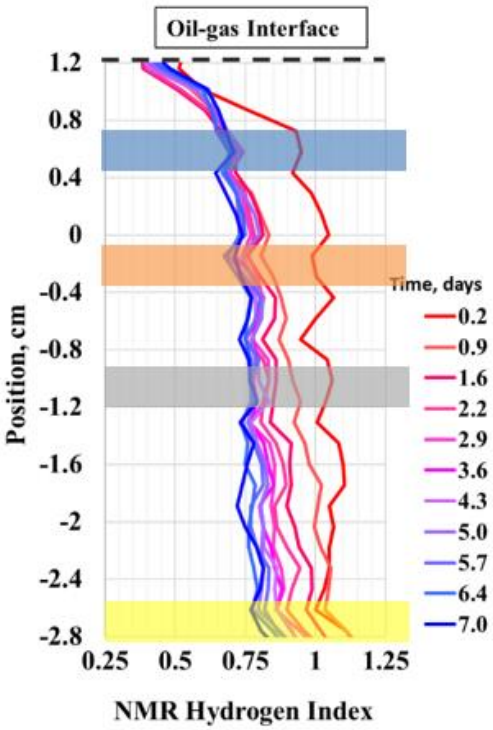

Figure 72. HI profile within the oil phase as a function of time. The decreasing HI value within the oil phase is due to the methane diffusion. HI temporal profiles at different positions (corresponding color labels for the positions of 0.6, -0.3, -1, -2.6 cm) within the oil phase are plotted in **Figure 73.**

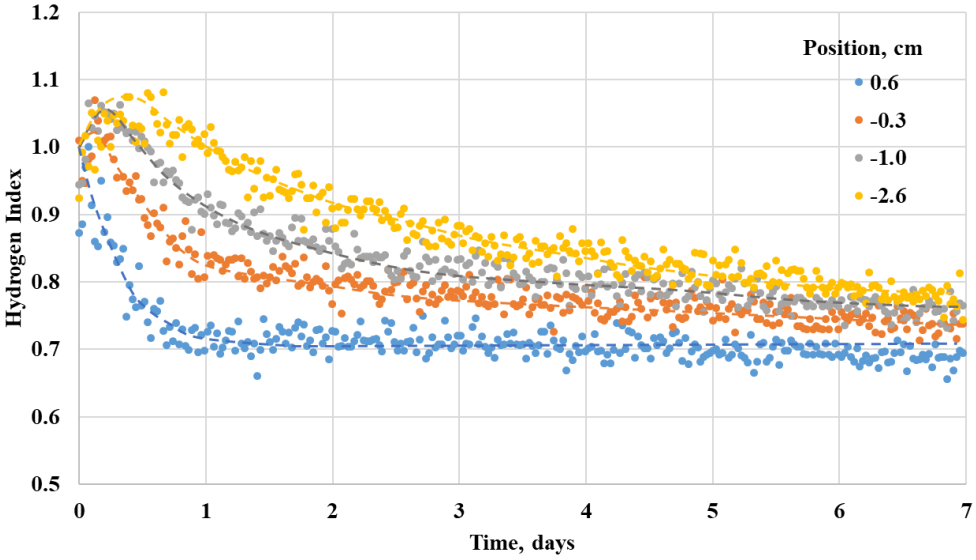

Figure 73. HI profiles at different positions within the oil phase. The marker colors correspond to highlighted depths in **Figure 72**. At the position closest to the oil-gas interface, HI decreases at a faster rate, eventually approaching a constant value, HI_{final}. HI_{final} corresponds to the maximum concentration of diffused methane into the oil phase. Dash lines represent HI profiles after smoothing.

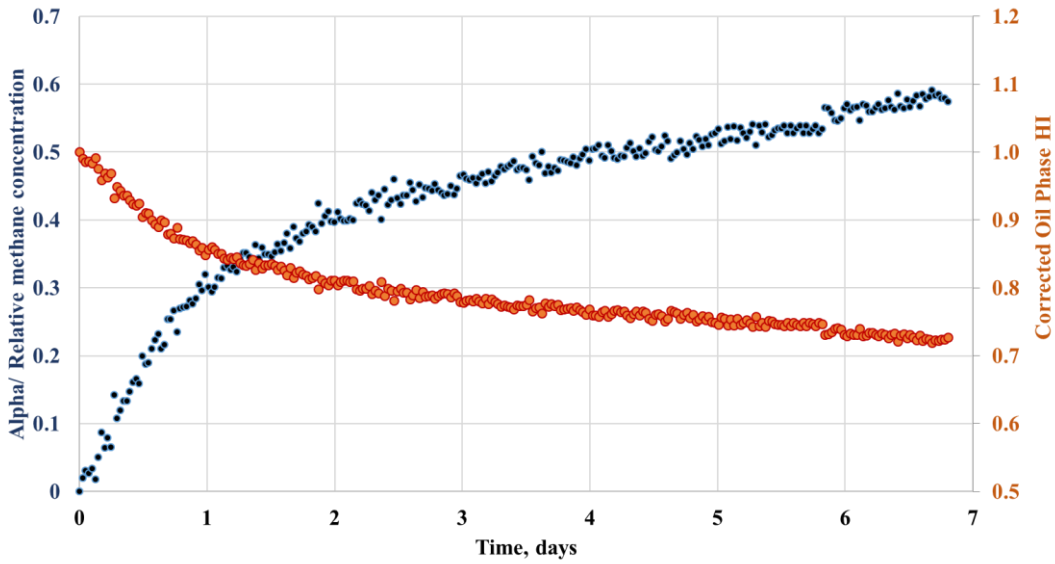

Figure 74. The integral of HI with respect to position (from x=0.3cm to x=-2.6cm), plotted as a function of time (red). Calculated relative methane concentration is also plotted (blue). The data are used to estimate the methane diffusion coefficient.

c) Discussions

Figure 73 show HI trends at different positions within the oil phase. The HI reduction rate varies with relative position to the interface; however, all approach a similar value of HI_{final}. In other words, for a specific reservoir fluid and injection gas, at a particular P-T condition, there is a maximum concentration of gas that can be introduced into the oil phase (Whitman, 1923). While modelling the dual diffusion of injection gases into reservoir fluids, this maximum concentration should be considered as a boundary condition; and now, we can estimate it from laboratory measurements.

Using Fick's second law (**Equation 4**), a diffusion coefficient can be estimated from the relative methane concentration profile. The equation should be used for infinite boundary condition; however, the experiment is a moving-boundary finite system; therefore, the middle-time data is used to extract diffusivity parameters. Note instead of using methane profile at a single position within the oil phase, we used the integral to reduce the impact of fluctuations in the data. C_s is methane concentration at the oil-gas interface. This is usually derived from the late-time diffusion data; however, with this study, C_s can be directly calculated from HI_{final}.

$$\frac{C(x,t)}{C_s} = 1 - \mathrm{erf}(z)$$
$$z = \frac{x}{2\sqrt{Dt}} \quad (4)$$

Figure 74 shows the fitting results for different diffusion coefficients using the relative methane concentration profile. The whole profile over 7 days can be fit with diffusion coefficients

ranging from 3.2×10^{-10} to 4.2×10^{-10} m^2/s; however, it is clear that the diffusion rate decreases as a function of time. This is considered as experimental artifact. While 1-D Fick's Law was solved for an infinite boundary condition, our test cell has limited volume. As soon as the first gas molecule travelling toward the oil phase approaches the end of the cell, the diffusion rate would be reduced.

By reviewing literature on diffusion measurements (Renner, 1986; Grogan et al., 1988 and Jamialahmadi et al., 2006), bulk diffusion rate can be varied over 2 orders of magnitude (10^{-10} – 10^{-8} m^2/s). Translating this to field EOR applications means to efficiently inject the same reservoir volume, the injection time can be also varied over 2 orders of magnitude.

2. Nano-porous Media Tortuosity

Hill and Lacy, (1934), Bertram and Lacy, (1935) and Reamer et al., (1956) have shown that the rate of dissolution of methane in a body of hydrocarbon liquid is controlled primarily by the rate of diffusion of the dissolved gas from the gas–liquid interface into the body of the liquid phase. On the other hand, the tortuous features of porous media also govern how fast gas can be injected into the matrix. Therefore, it is critical to understand the diffusion processes in any gas injection process in oil reservoirs.

Effective diffusion measurements in both dry and saturated porous media have been well established, although the availability of measurement data is limited (Chen, 1973 and Pandey et al., 1974). Many different methods utilizing secondary parameters, including pressure decay (Chen et al., 2018) or resistivity (Garrouch et al., 2001) are used to capture diffusional characteristics. However, the most direct technique to compute diffusion rate is the Wicke and Kallenbach, (1941) method, in which nitrogen is injected across one face of cylindrical porous media, and methane is

injected across the other. **Equation 5** developed by Evans et al., (1961) is used to back calculate diffusion rate by monitoring the change in fluid composition on both sides of the porous media:

$$D_e = \frac{N_n \alpha RTL}{PAln\left(\frac{1-\alpha Y_{nf}}{1-\alpha Y_{ni}}\right)} (5)$$

$$\alpha = 1 - \frac{N_m}{N_n}$$

in which D_e as effective diffusion coefficient; N_n and N_m are respectively molar diffusion rates of nitrogen and methane, mole/s; T is absolute temperature, ^oK; L is sample length, cm; R is gas constant; P is pore pressure, cm Hg; A is area of cross section, cm^2; Y_{nf} and Y_{ni} are respectively nitrogen mole fraction at final and initial points.

Most of diffusion rates computed or measured from previous methods for conventional rocks agree reasonably well. However, for unconventional tight rock like shales, there are drawbacks to each of these methods mainly due to the small storage and transmissibility factor. One common method of measurement is the monitoring of pressure decay while injecting gases to saturated sample; one of assumptions to validate this method is the instant pressure transit from the sample borders to the sample center. This is a very weak assumption for tight rocks. The Wicke and Kallenback (1941) method theoretically can be applied for tight rock; however, the practical difficulty of this technique lies on how fluid composition should be measured without flow interference. Small transmissibility characteristics of shales make conventional fluid sampling impossible. Moreover, the time-discrete fluid sampling makes it challenging to capture breakthrough time.

In this work, we introduce a new experimental set up to measure diffusion in tight rock like shales.

a) Experimental Approach and Method

Previous diffusion measurement data on sandstones Chen et al., (1977) suggested the diffusion factor (DF), the ratio of the diffusion coefficient across the porous media to the diffusion coefficient across open space, is an inverse function of sample tortuosity. The ultimate objective of the study is to estimate the effective diffusion coefficient of methane through a liquid saturated tight rock sample. We propose the experimental approach, in which effective diffusion coefficient of methane through liquid saturated porous matrix can be estimated from bulk methane-liquid diffusion coefficient and diffusion factor of the porous media.

Many previous studies have been carried out on bulk methane-liquid diffusion. Riazi et al., (1996) developed a method for determining diffusion coefficients of gases in liquids at constant volume and temperature using a PVT cell. Jamialahmadi et al., (2006) proposed an interesting approach using oil swelling factor as a function of time to estimate methane diffusion rate into different alkanes at high pressure and temperature.

By modifying to use the Wicke and Kallenbach (1941) method, we introduce novel approach to continuously monitor change in fluid composition on one face of cylindrical sample.

Infrared Spectroscopy (IR) has been applied extensively to characterize materials in different forms, including solid, liquid, and gas phases. In the oil and gas industry, this spectral analysis had been employed to measure mineralogy (see additional references above Ballard, 2007) and reservoir fluid composition (Livanos et al., 2016). Typically, all of these measurements were carried out under ambient or low-pressure conditions. For our objective, high pressure IR cells with transparent IR windows (Zinc Selenium for maximum 2500 psi and Sapphire for maximum 5000 psi) were installed in line with rock sample holder to analyze flow-through fluid signal.

Thermo-Scientific Nicolet 6700® FT-IR spectrometer (wavenumber ranges 600 – 4000cm^{-1}) was used to continuously analyze fluid signals. The schematic experimental set up is presented in **Figure 75**.

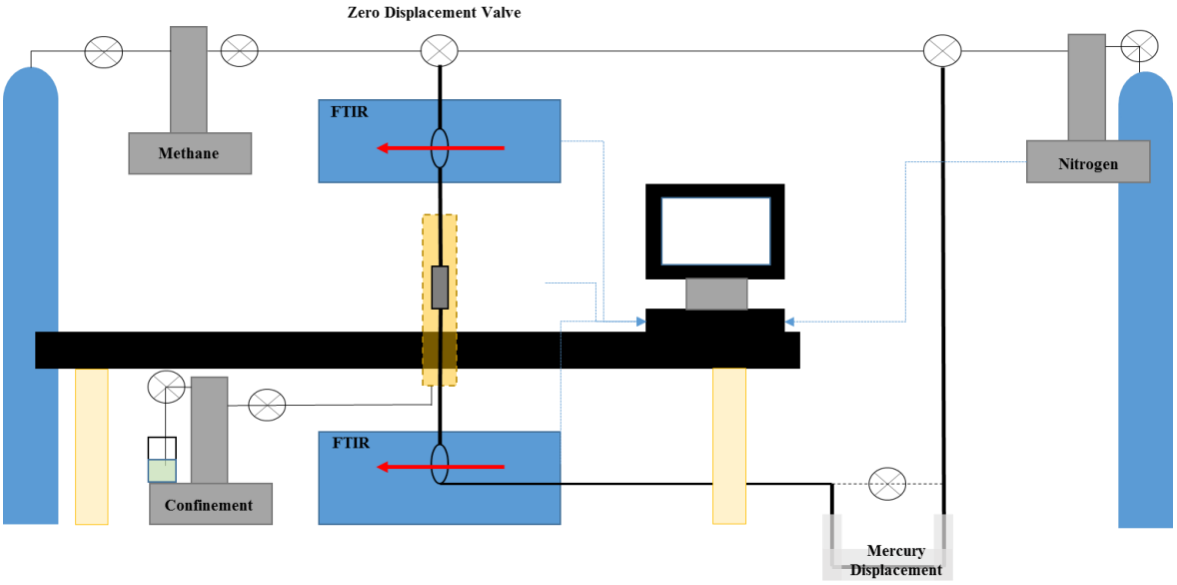

Figure 75. Experimental apparatus, in which porous media was vacuumed for 24hours, then filled with nitrogen for 24 hours, after which methane was allowed to diffuse through the porous media when the constant volume Vindum® valve was opened. A mercury displacement pump was used to keep the system under constant pore pressure throughout the diffusion process.

During experiments, methane diffused though rock sample saturated with nitrogen, constant pressure was maintained from both ends using a mercury displacement pump. The rock sample was confined with effective pressure of 3000 psi.

b) Fourier Transform – Infrared Spectroscopy (FTIR) Calibration

Throughout the diffusion process, the dynamic change of fluid composition is due to the exchange of methane and nitrogen molecules. The spectrometer captures IR absorbance intensity using an infrared source transmitted through the transparent IR windows: the absorbance is due to

the vibrational excitation of gas molecules between IR windows. As a symmetric diatomic molecule, nitrogen displays no IR absorbance in the observed bandwidth. On the other hand, methane absorbance spectrum can easily be captured with the main absorbance range of 2800-3100cm^{-1} (**Figure 51**, Nistchem Webbook)

Beer-Lambert Law (**Equation 1**) proposes a linear relationship between IR absorbance intensity and gas concentration. C_o, defined as IR absorptivity coefficient of a particular gas. This is a function of pressure and temperature. In this study, all experiments were conducted at room temperature. Therefore, for a single diffusion test at a certain pressure, methane concentration calibration needs to be provided.

Rubotherm Flexidose® Gas mixer was used to generate three different mixtures of methane and nitrogen. These three gas mixtures were used to calibrate IR absorptivity coefficients at different pressures. **Figure 76** presents the relationship between IR absorbance intensity versus pressure (pressure ranges from 100-500 psi) for different gas mixtures. **Figure 77** presents the relationship between IR absorbance intensity versus methane molar concentration at 500 psi. The slope of the linear correlation provides methane absorptivity coefficient at 500 psi. Repeating the same procedure, we obtain methane absorptivity coefficients at 200 psi and 300 psi. These coefficients were used to convert continuous IR absorbance spectra to a methane concentration profile during diffusion tests.

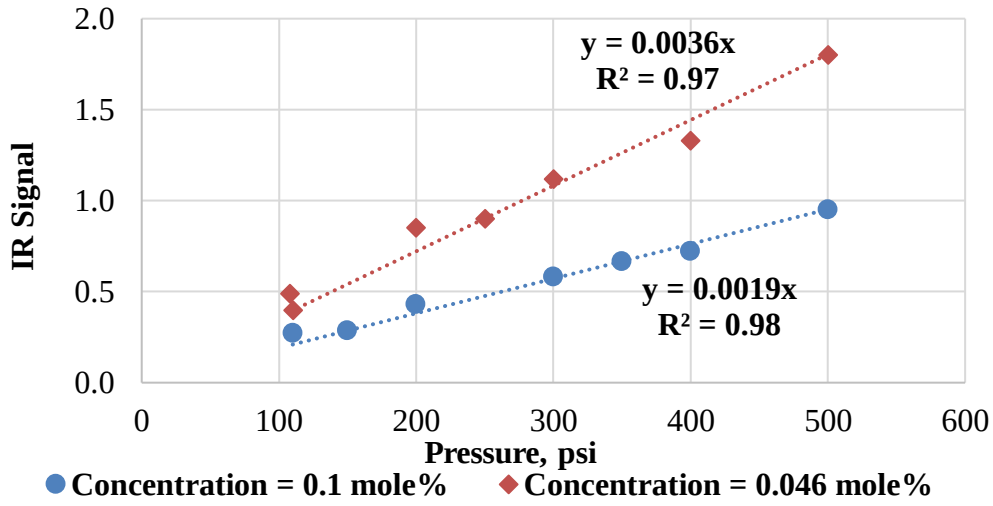

Figure 76. IR absorbance intensity of two methane-nitrogen mixtures at different pressures

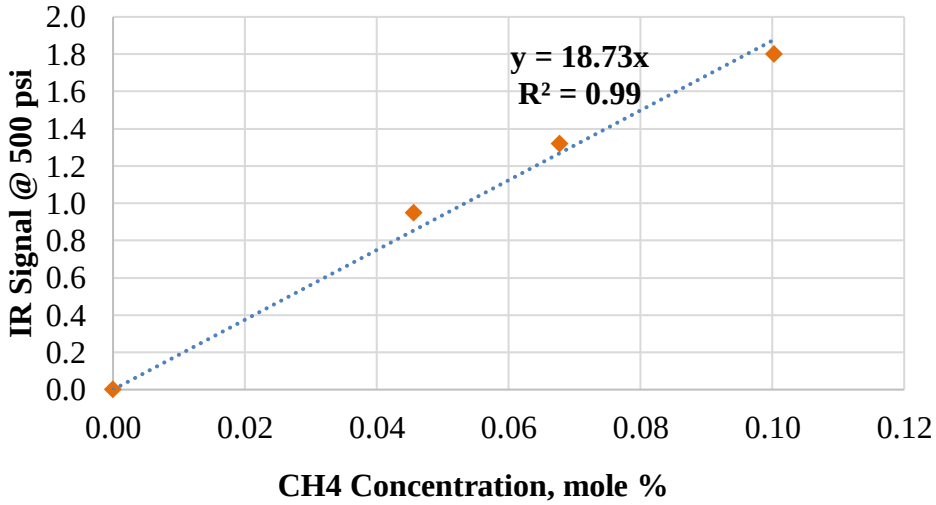

Figure 77. IR absorbance intensity of different methane-nitrogen mixtures at 500 psi, room temperature. The slope of linear correlation is considered the methane absorptivity, specifically at 500 psi, 18.73±1.15

c) Experimental Results and Discussion

A horizontal 1" core plug was selected for this study; the sample has a total crushed helium porosity of 3%; it was Soxhlet extracted with DCM: methanol (92:8 vol%) for 7 days and dried at 100°C under vacuum for 72 hours before each measurement. Different diffusion measurements were conducted at different pore pressures but at the same effective pressure with the same core

plug. **Figure 78** presents methane concentration profiles versus square root of time in minutes for methane-nitrogen diffusion through a shale sample and open space at a constant pressure of 500 psi. For bulk methane-nitrogen diffusion process, the breakthrough time is about 450 mins; whereas for the diffusion within a shale sample, the breakthrough time is about 3600 mins. The maximum molar concentration of methane at the end of each experiment (6400 minutes) is about 10%. With such small concentrations, conventional fluid sampling would not be able to provide a robust concentration profile for diffusion rate calculations. However, an IR spectrometer under stable background condition and filter denoising algorithm can detect methane signal down to the concentration of several ppm (Zhu et al., 2012.) Using **Equation 1**, effective diffusion coefficients of methane-nitrogen through open space and the shale sample are estimated as $3.25*10^{-8}$ and $0.4*10^{-8} m^2/s$, respectively. Applying these coefficients with second Fick's Law assuming 1-D model, we generated methane concentration profiles, which agree reasonably well with experimental data (**Figure 79**). The slight difference between fitted data and measured data can be due to the fact this is, in reality, a 3-D diffusion process. However, the assumption of 1-D diffusion is not a bad assumption, due to the fact horizontal permeability is much larger than vertical permeability in shale. The diffusion factor is about 0.125 for diffusion process at 500 psi. Diffusion factor data are presented in **Figure 80**, as a function of pressure. Calculated diffusion factors at different pressures are the same with 90% confidence. This supports the idea that the diffusion factor represents tortuous characteristic of porous media.

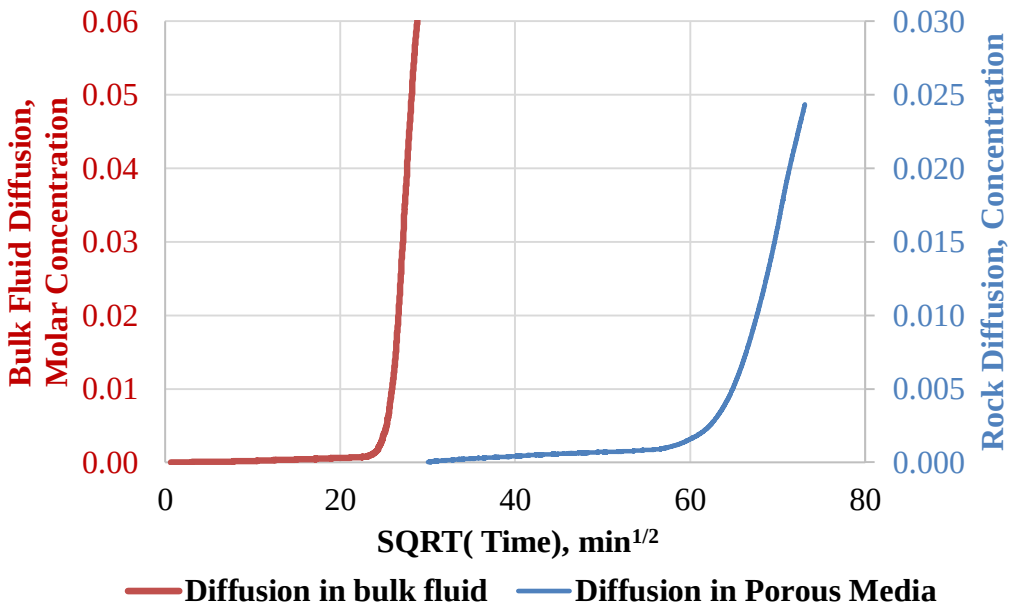

Figure 78. Methane concentration versus square root of diffusion time. The red curve is methane-nitrogen diffusion through open space. The blue curve is methane-nitrogen diffusion through a rock sample.

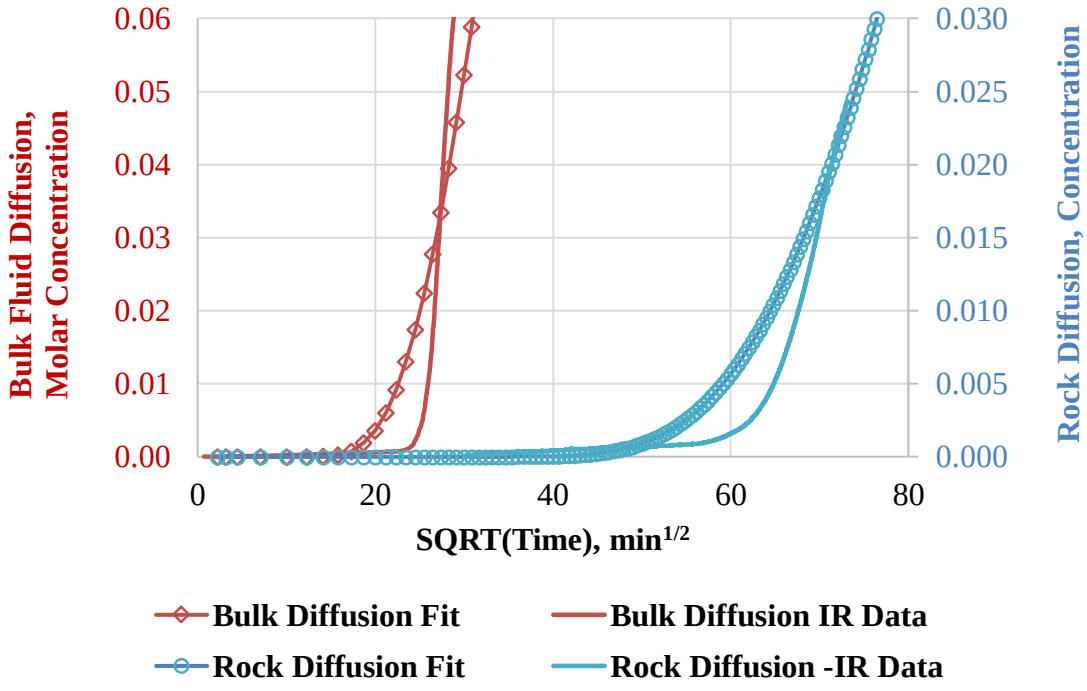

Figure 79. Methane-nitrogen diffusion through open space (red) and a rock sample (blue). Solid lines are experimental data, while open circles are the fit using 1 1-D Fick's second law with effective diffusion

coefficients are $3.25*10^{-8}$ and $0.4*10^{-8}m^2/s$, respectively for bulk fluid diffusion and porous media diffusion, a factor of 8 difference.

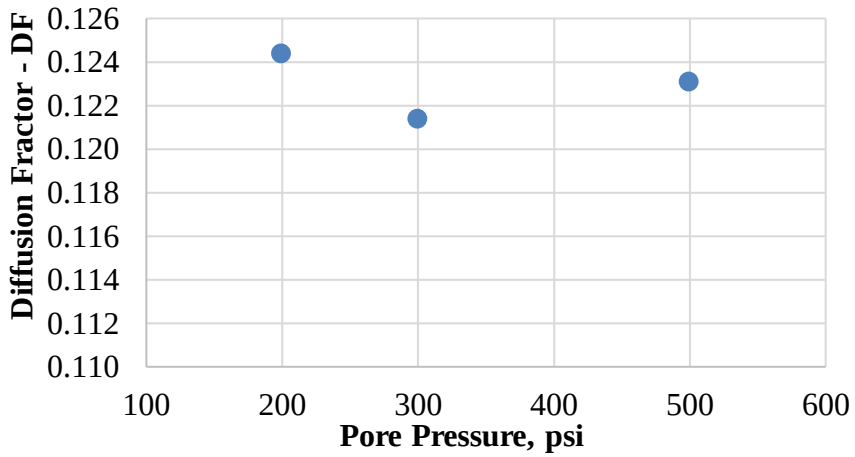

Figure 80. Diffusion factor or the ratio of effective diffusion coefficient through porous media to diffusion coefficient through open space, is effectively constant over the pore pressure range 100-500 psi.

Tortuosity for the shale sample is estimated as the inverse of the diffusion factor; this shale sample has porosity of 3%. The result is plotted combined with literature data, showing the negative exponential correlation between tortuosity and porosity (**Figure 81 a & b**) Note the data include measured tortuosity values for sand packs, unconsolidated sands, and tight sands.

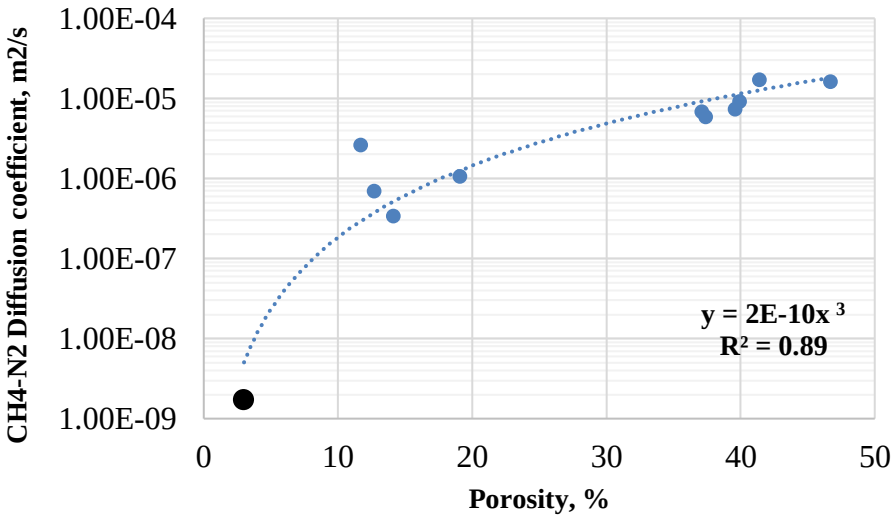

a)

b)

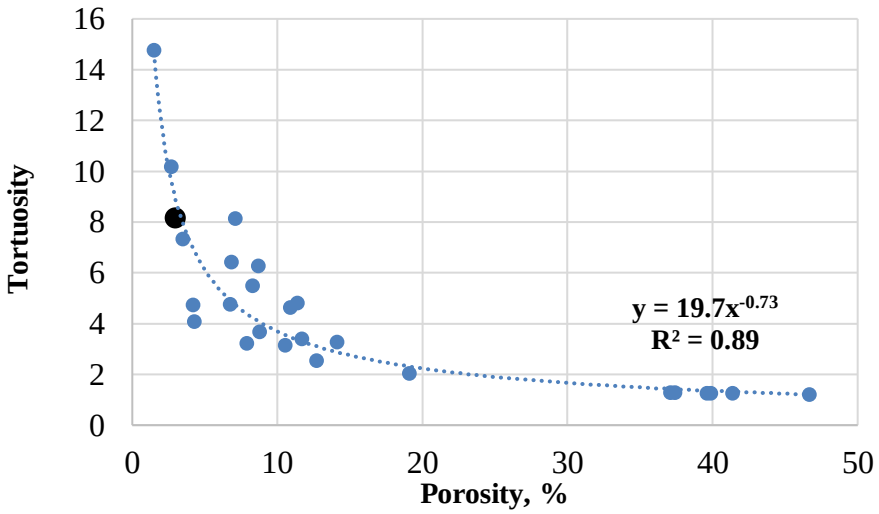

Figure 81. a) Effective methane-nitrogen diffusion coefficient from an Eagle Ford sample used in this study (black dot) (with porosity of 3%) plotted against literature data (blue dots) (Chen et al., 1977). b) Dimensionless tortuosity, or the inverse of diffusion factor – DF, from an Eagle Ford sample used in this study (with porosity of 3%) plotted against literature data (blue dots) (Chen et al., 1977).

Conclusions

Our studies focus on defining and estimating key parameters for gas diffusion in a very low permeability porous medium which allow engineers to model the EOR process in unconventional formations. The key parameters include porous matrix tortuosity and bulk fluid diffusivity. For example, in gas injection EOR, the combination of these two factors governs how fast injection gas molecules travel into the porous matrix and interact with the reservoir fluid; hence, injection and production strategy can be optimized. Common to the success of initial field experiments in the Eagle Ford shale is their initial soak times of 1 to 2 months. Assuming most of shale formations have porosities less than 5-7%, shale tortuosity factors above 5 and methane-oil diffusion ranges $1\text{-}2\times10^{-8}$ m^2/s, this means injected gas does not move more than 1-2ft into the formation after a

typical soaking period. Therefore, most of injected gas-reservoir fluid interaction happens near fracture/cracks surfaces.

However, direct measurements of diffusion coefficients in shales are not currently available. This is directly attributable to the lack of available techniques for their measurement. The small shale pore volumes make these measurements challenging. We introduce a novel approach to measure the diffusion coefficient of injected gas in shale samples. The effective diffusion between methane versus nitrogen were simultaneously measured with Infrared Spectroscopy (IR) methods which eliminate the need to physically sample fluids and hence eliminates the associated pressure transients. IR captured the change with time in methane/nitrogen concentration at the outlet of the sample. The difference in effective diffusion with and without the microporous media, provide a measure of sample tortuosity. In the end, a simulation model was established based on the experimental setup to back-calculate diffusion rate. The experimental results show that unlike most conventional reservoir rock with tortuosity factors oscillating around 2, tight rock samples can have a greater range of tortuosity from 4 to 16.

In parallel, a new method was developed to estimate fluid diffusion coefficient between methane and a crude oil sample which used NMR with a 1-D gradient. The technique directly captures the dynamic change of methane concentration within the oil body, reflected through the change in the HI value. This technique overcomes a major challenge of previous methods, i.e. it can directly measure HI_{final}, or molecular exchange rate at the oil-gas contact, which is defined as the boundary condition to fit diffusion rate.

Acknowledgement

This work was funded by the University of Oklahoma's Unconventional Shale Consortium and ENCNA. We thank the members of Integrated Core Characterization Center (IC3) for helping us during experimentation. Special thanks to Richard Newhart, Tom Smagala, John Mansoori, and Mark Tobey for their continuous supports, guidance and practical feedbacks.

References

1. Abrams, M.A., Gong, C., Garnier, C. and Sephenson, M. A., 2017. A new thermal extraction protocol to evaluate liquid rich unconventional oil in place and in-situ fluid chemistry. *Journal of Marine and Petroleum Geology* 88:659 -675
2. Adekunle, O., 2014. Experimental approach to investigate minimum miscibility pressures in the Bakken. Master Thesis. Colorado School of Mines.
3. Ajisafe, F. O., Solovyeva, I., Morales, A., Ejofodomi, E., and Porcu, M. M., 2017. Impact of well spacing and interference on production performance in unconventional reservoirs, Permian basin. Unconventional Resources Technology Conference. doi:10.15530/URTEC-2017-2690466
4. Altman, R. M., Fan, L., Sinha, S., Stukan, M., and Viswanathan, A., 2014. Understanding Mechanisms for Liquid Dropout from Horizontal Shale Gas Condensate Wells. *Society of Petroleum Engineers*. doi:10.2118/170983-MS
5. Anderson, D. M., Thompson, J. M., Cadwallader, S. D., Sebastian, H., Gil, I., and Lee, P., 2016. Maximizing Productive Stimulated Reservoir Volume in the Eagle Ford - An Infill Case Study. *Unconventional Resources Technology Conference*. doi:10.15530/URTEC-2016-2430961
6. Ballard, B.D., 2007. Quantitative mineralogy of reservoir rocks using Fourier transform infrared spectroscopy. Society of Petroleum Engineers. doi:10.2118/113023-STU
7. Bello, R. O., 2009. Rate transient analysis in shale gas reservoirs with transient linear behavior. Doctoral Dissertation. Texas A&M University
8. Bertram, E. A., and Lacy, W. N., 1935. Rates of solution of gases in oils. Ind. Eng. Chem. 28, 316–318.
9. Besov, A., Tinni, A., Sondergeld, C., Rai, C., Paul, W., Ebnother, D., and Smagala, T., 2017. Application of laboratory and field NMR to characterize the Tuscaloosa marine shale. Society of Petrophysicists and Well-Log Analysts.
10. Bhoumic, P., Sondergeld C. and Rai, C., 2018. Mapping hydraulic fracture in pyrophyllite using shear wave, ARMA 18-51.
11. Brace, W. F., Walsh, J. B., and Frangos, W. T., 1968. Permeability of granite under high pressure. Journal of geophysical research, 73, 6, 2225-2236
12. Brown, R. J. S., 1961. Proton relaxation in oils. Nature 198: 387-388. https://doi.org/10.1038/189387 a0
13. Bryan, J., Manalo, F., Wen, Y. et al., 2002. Advances in heavy oil and water property measurements using low field nuclear magnetic resonance. SPE International Thermal Operations and Heavy Oil Symposium and International Horizontal Well Technology Conference, Calgary, 4-7 November, SPE-78970-MS
14. Cao, R., Li, R., Girardi, A., Chowdhury, N., and Chen, C., 2017. Well interference and optimum well spacing for Wolfcamp development at Permian basin. *Unconventional Resources Technology Conference*. doi:10.15530/URTEC-2017-2691962
15. Chakravarty, A., Tinni, A., Rai, C. S., and Sondergeld, C. H., 2018. NMR considerations in shales at elevated temperature. Unconventional Resources Technology Conference. doi:10.15530/ URTEC-2018-2902883
16. Chen, D., Pan, Z., and Ye, Z., 2015. Dependence of gas shale fracture permeability on effective stress and reservoir pressure: Model match and insights. Fuel, 139, 383-392

17. Chen, L.L.Y., 1973. Binary Gas Diffusion of methane-nitrogen through porous media. Ph.D. Thesis, Univ. Mich.
18. Chen, L.L.Y., Katz, D.L., and Tek, M. R., 1977. Binary gas diffusion of methane-nitrogen through porous media. AIChE Journal, Vol. 23, No. 3, 336.
19. Chen, M., Kang, Y., Zhang, T., You, L., Li, X., Chen, Z., Wu, K., and Yang, B., 2018. Methane diffusion in shales with multiple pore sizes at supercritical conditions. *Chemical Engineering Journal*, No. 334, 1455-1465
20. Coates, G. R., Peveraro, R. C. A., Harwick. A. et al., 1991. The magnetic resonance imaging log characterized by comparison with petrophysical properties and laboratory core data. SPE ATCE, Dallas, 6-9 October. SPE-22723-MS.
21. Condon, S. M. and Dyman, T. S., 2006. Geologic Assessment of Undiscovered Conventional Oil and Gas Resources in the Upper Cretaceous Navarro and Taylor Groups, Western Gulf Province, Texas, U.S. in Chapter 2 of Petroleum Systems and Geologic Assessment of Undiscovered Oil and Gas, Navarro and Taylor Groups, Western Gulf Province, Texas: Geological Survey Digital Data Series DDS-69-H.
22. Coutelieris, F. A., Kainourgiakis, M. E., and Stubos, A. K., 2002. The effects of Peclet on the Sherwood number in high porosity granular media. Studies in Surface Science and Catalysis, Vol 144, p. 753-760
23. Craig, D. P., 2017. Determining Fracture Geometry in a Multifractured horizontal well using DFIT Interpretation, Intra-well Fracture-To-Fracture Interference, and Production History Matching. *Unconventional Resources Technology Conference*. doi:10.15530/URTEC-2017-2695331
24. Cronin, M., Emami-Meybodi, H., and Johns, R. T., 2018. Diffusion-dominated proxy model for solvent injection in ultra-tight oil reservoirs. Society of Petroleum Engineers. doi:10.2118/190305-MS
25. Curtis, T., and Montalbano, B. 2017. Completion design changes and the impact on US shale well productivity. The Oxford institute for energy studies, November issue
26. Damani, A., Sondergeld, C., and Rai, C., 2018. Experimental investigation of in situ and injection fluid effect on hydraulic fracture mechanism using acoustic emission in Tennessee sandstone. Journal of Petroleum Science and Engineering.
27. Dang, S. T., Sondergeld, C. H., and Rai, C. S., 2016. Reducing ambiguity in source rock analyses. Unconventional Resources Technology Conference. doi:10.15530/URTEC-2016-2461388
28. Dang, S. T., Sondergeld, C. H., and Rai, C. S., 2016. Understanding source rock maturation from generation and microstructure viewpoints. *Unconventional Resources Technology Conference*.
29. Dang, S. T., Sondergeld, C. H., and Rai, C. S., 2019. Interpretation of nuclear-magnetic-resonance response to hydrocarbons: application to miscible enhanced-oil-recovery experiments in shales. Society of Petroleum Engineers. doi:10.2118/191144-PA
30. Dang, S. T., Sondergeld, C. H., and Rai, C. S., 2019. Effects of temperature and gas pressurization on the interpretation of nuclear magnetic resonance (NMR) hydrocarbon measurements in organic rich shales. URTeC 2019
31. Dang, S. T., Sondergeld, C. H., Rai, C. S., Tinni, A, O., Drenzek, N., 2018. A first step in evaluating the role of diffusion **in** EOR in tight shale formations. SCA-2018

32. Dang, S., Gupta, I., Chakravarty, A., Bhoumick, P., Taneja, S., Sondergeld, C., and Rai, C., 2017. Recovering elastic properties from rock fragments. Society of Petrophysicists and Well-Log Analysts.
33. Das, I. and Zoback, M., 2011. Long period - long duration seismic events during hydraulic stimulation of a shale gas reservoir. The Leading Edge, July 2011 issue
34. Du, C., Zhang, X., Ma, Z., Kaufman, P., Melton, B., and Gowelly, S., 2011. Integrated shale gas reservoir modeling. AAPG Memoir. 96. 265-280. 10.1306/13301419M963487
35. EIA, U.S. Energy Information and Administration, https://www.eia.gov/dnav/pet/pet_crd_crpdn_adc_mbblpd_a.htm (accessed: September 29th, 2019)
36. Escobar, F. H., Zhao, Y. L., and Zhang, L. H., 2014. Interpretation of pressure test in hydraulically fractured wells in bi-zone gas reservoirs. *Ingenieria E Investigacion* 34, 2, 76-84
37. Evans R.B., Watson G.M., and Mason E.A., 1961. Gaseous diffusion in porous media at uniform pressure, *J. Chem. Phys*, 35, No. 6, 2076
38. Feng Q., Xia T., Wang, S., and Singh, H., 2017. Pressure transient behavior of horizontal well with time-dependent fracture conductivity in tight oil reservoirs. Geofluids, vol. 2017, Article ID 5279792, p 19. https://doi.org/10.1155/2017/5279792.
39. Fleury, M. and Brosse, E., 2017. Transport in tight rocks. AGU Hydrobiogeochemical Properties of Caprock, June.
40. Gale, J., Reed, R., and Holder, J., 2007. Nature fracture in the Barnett shale and their importance for hydraulic fracture treatments, *AAPG Bull*, 91, 4, 603–622
41. Gamadi, T. D., Sheng, J. J., and Soliman, M. Y., 2013. An experimental study of cyclic gas injection to improve shale oil recovery. *SPE ATCE*
42. Gamadi, T. D., Sheng, J. J., Soliman, M. Y., Menouar, H., Watson, M. C., and Emadibaladehi, H., 2014. An experimental study of cyclic CO2 injection to improve shale oil recovery. In: SPE IOR Symposium; 2014.
43. Garrouch, A.A., Liaqat, A., and Fuad, Q., 2001. Using diffusion and electrical measurement to assess tortuosity of porous media. *Ind. Eng. Chem. Res*, No. 40, 4363-4369
44. Gavrilenko, P., and Gueguen, Y., 1989. Pressure dependence of permeability: a model for cracked rocks. *Journal of Geophysics*, 98, 159-172
45. Golkari, A., and Riazi, M., 2016. Experimental investigation of miscibility conditions of dead and live asphaltenic crude oil – CO_2 systems. *Journal of Petroleum Exploration and Production Technology*, Vol 7, Issue 2, 597-609
46. Gonzalez, D. L., Ting, P. D., Hirasaki, G. J., and Chapman, W. G., 2005. Prediction of asphaltene instability under gas injection with the PC_SAFT equation of state. *Energy & Fuels*, 19, 1230-1234
47. Gou, P., Wang, Z., Shen, P., and Du, J., 2009. Molecular diffusion coefficients of the multicomponent gas-crude oil systems under high temperature and pressure. Ind. Eng. Chem. Res, 48, p. 9023-9027
48. Grogan, A. T., Pinczewski, V. W., Ruskauff, G. J., and Orr, F. M., 1988. Diffusion of CO_2 at reservoir conditions: models and measurements. Society of Petroleum Engineers. doi:10.2118/14897-PA
49. Gueguen, Y., and Dienes, J., 1989. Transport properties of rocks from statistics and percolation. Mathematical Geology, 21, 1

50. Harville, D. G. and D. L. Freeman, 1988. The benefits and application of rapid mineral analysis provided by Fourier transform infrared spectroscopy, SPE 18120.
51. Hawthorne, S. B., Gorecki, C. D., Sorensen, J. A., Steadman, E. N., Harju, J. A., Melzer, S., 2013. Hydrocarbon mobilization mechanisms from Upper, Middle, and Lower Bakken reservoir rocks exposed to CO2. *SPE Unconventional Resources Conference Canada*
52. Hawthorne, S. B., Miller, D. J., Jin, L., and Gorecki, C. D., 2016. Rapid and Simple Capillary-Rise/Vanishing Interfacial Tension Method to Determine Crude Oil Minimum Miscibility Pressure: Pure and Mixed CO2, Methane, and Ethane. *Energy & Fuel*, 30, 8, 6365-6372
53. Hentz, T. F., and Ruppel, S. C., 2011. Regional Stratigraphic and Rock Characteristics of Eagle Ford Shale in Its Play Area: Maverick Basin to East Texas Basi. *Search and Discovery, AAPG*
54. Herron, M. M., Matteson, A. and Gustavson, G., 1997, Dual-range FT-IR mineralogy and the analysis of sedimentary formations, SCA-9729.
55. Hill, E.S., and Lacy, W.N., 1934. Rate of solution of methane in quiescent liquid hydrocarbons. Ind. Eng. Chem. 26, 1324–1327.
56. Hirasaki, G. J., Lo, S. W., and Zhang, Y., 2003. NMR properties of petroleum reservoir fluids. Magnetic Resonance Imaging, Vol. 21, Issues 3-4, p. 269-277. https://doi.org/10.1016/S0730-725X(03)00135-8
57. Hoffman, T. B. and Evans, J. G., 2016. Improved oil recovery IOR pilot projects in the Bakken formation, SPE180270.
58. Hoffman, T. B., 2018. Huff-n-Puff gas injection pilot projects in the Eagle Ford, SPE189816.
59. Igisu, M., Ueno, Y., Shimojima, M., Nakashima, S., Awramik, S., Ohta, H., and Maruyama, S., 2009. Micro-FTIR spectroscopic signatures of bacterial lipid in Proterozoic microfossils. *Precambrian Research*, 173, 19-26
60. Indras, P., 2014. Applying decline curve analysis in the liquid-rich shales: Eagle Ford shale study. Master Thesis. Texas A&M University
61. Iversen, N., and Jorgensen, B. B., 1993. Diffusion coefficients of sulfate and methane in marine sediments: influence of porosity. *Geochimica et Cosmochimica Acta* 57, 571–578
62. Jaeger, J., Cook, N., and Zimmerman, R., 2007. Fundamentals of Rock Mechanics, 4th ed., Blackwell, Malden, Mass.
63. Jamialahmadi, M., Emadi, M. and, Muller-Steinhagen, H., 2006. Diffusion coefficients of methane in liquid hydrocarbons at high pressure and temperature. Journal of Petroleum Science and Engineering. Vol 52, 1-2, p. 47-60.
64. Jarvie, D. M., Hill, R. J., Ruble, T. E., and Pollastro R. M., 2007. Unconventional shale-gas systems: The Mississippian Barnett Shale of North-Central Texas as one model for thermogenic shale-gas assessment. *AAPG Bulletin*, 91, 475 – 499.
65. Kampfer, G., and Dawson, M., 2016. A novel approach to mapping hydraulic fractures using poromechanic principles. *American Rock Mechanics Association*. ARMA 2016-843
66. Karger, J., Ruthven, D. M., and Theodorou, D. N., 2012. Diffusion in nanoporous materials. John Wiley & Sons, p. 92-93

67. Kenyon, W. E., Day, P. I., Straley, C., and Willemsen, J. F. 1986. A three-part study of NMR longitudinal relaxation properties of water-saturated sandstones, SPE Formation evaluation, September, 622-636. SPE 15643
68. Kenyon, W. E., Kleinberg, B. R., Straley, C., Gubelin, G., and Morris, C. 1995. Nuclear magnetic resonance imaging-technology for the 21st century, Oil Field Review, Autumn, 19-33.
69. Kenyon, W. E., Takezaki, H., Straley, C., Sen, P. N., Herron, M., Matteson, A., and Petricola, M. J., 1995., A laboratory study of nuclear magnetic resonance relaxation and its relation to depositional texture and petrophysical properties - Carbonate Thamama group, Mubarraz field, Abu Dhabi, SPE 29886.
70. Kovscek, A. R., Tang, G. Q., and Vega, B., 2008. Experimental investigation of oil recovery from siliceous shale by CO2 injection. *SPE ATCE*
71. Leontaritis, K. J., and Mansoorimm A. G., 1988. Asphaltene deposition: a survey of filed experiences and research approaches. Journal of petroleum Science and Engineering, 1, 229-239
72. Li, l., Sheng, J. J., Su, Y. and, Zhan, S., 2018. Further Investigation of Effects of Injection Pressure and Imbibition Water on CO2 Huff-n-Puff Performance in Liquid-Rich Shale Reservoirs. *Energy & Fuel*, 32, 5789-5798
73. Li, L., Su, Y., and Sheng, J. J. 2018. Investigation of gas penetration depth during gas huff-n-puff EOR process in unconventional oil reservoirs. Society of Petroleum Engineers. doi:10.2118/189804-MS
74. Li, L., Su, Y., Sheng, J. J., Hao, Y., Wang, W., Lv, Y., Zhao, Q., Wang, H., 2019. Experimental and numerical study on CO_2 sweep volume during CO_2 huff-n-puff enhanced oil recovery process in shale oil reservoirs. Energy Fuels.10.1021/acs.energyfuels.9b0016
75. Li, L., Zhang, Y., and Sheng, J. J., 2017. Effect of the injection pressure on enhancing oil recovery in shale cores during the CO2 Huff-n-Puff process when it is above and below the minimum miscibility pressure. *Energy & Fuels*, 31, 3856-3867
76. Livanos, G., Zervakis, M., Pasadakis, N., Karelioti, M., and Giakos, G., 2016. Deconvolution of petroleum mixture using mid-FTIR analysis and non-negative matrix factorization. *Measurement Science and Technology*, No. 27
77. Maxwell, S. C., Cho, D., Pope, T. L., Jones, M., Cipolla, C. L., Mack, M. G., and Leonard, J. A., 2011. enhanced reservoir characterization using hydraulic fracture microseismicity. *Society of Petroleum Engineers*. doi:10.2118/140449-MS
78. Metwally, Y. M., and Sondergeld, C. H., 2011. Measuring low permeability of gas sands and shales using a pressure transmission technique. *International Journal of Rock Mechanics & Mining* Sciences 48, 1135-1144
79. Miller, J. J. S., and Jones, R. A., 1981. A laboratory study to determine physical characteristics of heavy oil after CO_2 saturation. *SPE/DOE Symposium on EOR*
80. Mittal, A., Rai, C. S., and Sondergeld, C. H., 2017. Laboratory investigation of proppant-pack conductivity: Eagle Ford and Vaca Muerta Shale. *Unconventional Resources Technology Conference*. doi:10.15530/URTEC-2017-2670951
81. Molenaar, M. M., Hill, D., Webster, P., Fidan, E., and Birch, B., 2012. First downhole application of distributed acoustic sensing for hydraulic-fracturing monitoring and diagnostics. *Society of Petroleum Engineers.* doi:10.2118/140561-PA
82. Negin, C., Ali, S., and Xie, Q., 2017. Most common surfactants employed in chemical enhanced oil recovery. *Journal of Petroleum*, 3, 197-211

83. Nistchem Webbook, https://webbook.nist.gov/cgi/cbook.cgi?ID=C74828&Units=SI&Type=IR-SPEC&Index=0#IR-SPEC
84. Nwabuoku, K. C., 2012. Study optimizes eagle ford completion. *The American Oil &Gas Reporter*
85. Odusina, E., Sondergeld, C. H., and Rai, C. S., 2012. An NMR study on shale wettability. Canadian Unconventional Resources Conferences, Calgary, 15-17 November. SPE-147371-MS.
86. Oil and Petroleum Products: Imports and Exports, https://www.eia.gov/energyexplained/index.php?page=oil_imports (accessed: May 29th, 2019)
87. Pandey, G. H., Katz. D. L., and Tek, M. R., 1974. Diffusion of fluids through porous media with implications in petroleum geology. *American Association of Petroleum Geologists Bulletin*, 58, No. 2, 291
88. Perkins, T. K., and Johnston, O. C., 1963. A review of diffusion and dispersion in porous media. *Society of Petroleum Engineers*. 480-PA SPE Journal Paper
89. Perkins, T. K., Johnston, O. C., and Hoffman, R. N., 1965. Mechanics of viscous fingering in miscible system. *Society of Petroleum Engineers*. 1229-PA SPE Journal Paper
90. Pruess, K., and Narasimhan, T. N., 1985. A practical method for modeling fluid and heat flow in fractured porous media. *SPE Journal* 5 (01), 14–26.
91. Qanbari, F., and Clarkson, C. R., 2016. Rate-Transient Analysis of Liquid-Rich Tight/Shale Reservoirs Using the Dynamic Drainage Area Concept: Examples from North American Reservoirs. *Society of Petroleum Engineers*. doi:10.2118/180230-MS
92. Raterman, K. T., Farrell, H. E., Mora, O. S., Janssen, A. L., Gomez, G. A., Busetti, S., and Warren, M., 2017. Sampling a Stimulated Rock Volume: An Eagle Ford Example. *Unconventional Resources Technology Conference*. doi:10.15530/URTEC-2017-2670034
93. Ratzlaff, C. W., C. H. Sondergeld, C. S. Rai, M.E. Curtis and Jernigen, J. D., 2019, SEM investigation of the fracture network (Stimulated Reservoir Volume) induced by hydraulic fracturing in Tennessee sandstone, ARMA 19-490.
94. Reamer, H. H., Opfell, J. B., and Sage, B. H., 1956. Diffusion coefficients in hydrocarbon systems: methane–decane–methane in liquid phase. Ind. Eng. Chem. 48, 275–282.
95. Renner, T. A., 1988. Measurement and correlation of diffusion coefficients for CO_2 and rich-gas applications. Society of Petroleum Engineers. doi:10.2118/15391-PA
96. Riazi, M.R., 1996. A new method for experimental measurement of diffusion coefficients in reservoir fluids. J. Pet. Sci. Eng. 14, 235–250
97. Roehner, R., Panja, P., Deo, M., 2016. Reducing gas flaring in oil production from shales. *Energy & Fuels* 30, 9, 7524-7531
98. Roussel, N. P., and Sharma, M. M., 2011. Strategies to minimize frac spacing and stimulate natural fractures in horizontal completions. Society of Petroleum Engineers. doi:10.2118/146104-MS
99. Rydzy, M. B, Patino, J., Elmetni, N., and Appel, M., 2016. Stressed permeability in shales: effects of matrix compressibility and fractures - a step towards measuring matrix permeability in fractured shale samples. *SCA Symposium*.
100. Rystad Energy, 2014, North American Shale Well Cube, https://www.rystadenergy.com/newsevents/news/press-releases/naswellcube-release/
101. Rystad Energy, 2014. Permian becoming largest US tight oil play. *Oil & Gas Financial Journal*.

102. Sarma, H. K., 2003. Can we ignore asphaltenes in a gas injection project for light oil? *SPE IOR Conference*
103. Sayegh, S. G., and Maini, B. B., 1984. Laboratory evaluation of the CO_2 huff-n-puff process for heavy oil reservoirs. *Journal of Canadian Petroleum Technology*.
104. Sayers, C., 1999. Stress-dependent seismic anisotropy of shales. *Geophysics*, 64, 93 –98.
105. Sayers, C., and Kachanov, M., 1995. Micro cracks-induced elastic wave anisotropy of brittle rocks, *Journal of Geophysical Research*, 100, 4149–4156.
106. Shen, Z., and Sheng, J. J., 2017. Investigation of asphaltene deposition mechanism during CO_2 huff-n-puff injection in Eagle Ford shale. *Petroleum Science and Technology*, 35, 20, 1960-1966
107. Sheng, J. J., 2015. Enhanced oil recovery in shale reservoirs by gas injection. *Journal of Natural Gas Science & Engineering* 22, 252–259
108. Sheng, J. J., and Chen K., 2014. Evaluation of the EOR potential of gas and water injection in shale oil reservoirs. *Journal of Unconventional Oil Gas Resources* 5, 1–9
109. Sigmund, P. M., 1976. Prediction of molecular diffusion at reservoir conditions, Part 1-measurement and prediction of binary dense gas diffusion coefficients. J. Can. Pet. Technol., 15 (2), pp. 48-57
110. Sinha, A., Dang, S., Sondergeld, C., and Rai, C., 2017. Impact of solvent extraction on surface area measurements in organic-rich shales using nitrogen adsorption. Unconventional Resources Technology Conference. doi:10.15530/URTEC-2017-2668849
111. Sondergeld, C. H. and Rai, C. S., 1993, A new concept in quantitative core characterization, The Leading Edge, 12, 7, 774-779
112. Song, C., and Yang, D., 2013. Performance evaluation of CO2 huff-n-puff processes in tight oil formations. *SPE Unconventional Resources Conference Canada*
113. Sonnenfeld, M. D., and Canter, L., 2016. How mobile is your total oil saturation? SARA analysis implications for bitumen viscosity and UV fluorescence in Niobrara marl and Bakken shale, supported by FIB_SEM observations of kerogen, bitumen and residual oil saturation within Niobrara marl and chalks. *AAPG Annual Convention & Exhibition*
114. Sorensen, j. A., and Hamling, J. A., 2016. Enhanced oil recovery: historical Bakken test data provide critical insights on EOR in tight oil plays. *The American Oil &Gas Reporter*
115. Straley, C. D., Rossini, C. D., Vinegar, H., Tutunjian, P., and Morriss, C., 1994. Core analysis by low field NMR, SCA-9404.
116. Sun, J., Zou, A., and Schechter, D., 2016. Experimental and numerical studies of CO2 EOR in unconventional liquid reservoirs with complex fracture networks. *SPE IOR Conference*
117. Ting, P. D., Hirasaki, G. J., and Chapman, W. G., 2007. Modeling of asphaltene phase behavior with SAFT equation of state. *Petroleum Science and Technology*, 21, 3, 647-661
118. Tinni, A., Sondergeld, C., and Rai, C., 2017. Pore connectivity between different wettability systems in organic-rich shales. *Society of Petroleum Engineers*. doi:10.2118/185948-PA
119. Tovar, F. D., Eide, O., Graue, A., and Schechter, D. S., 2014. Experimental investigation of enhanced recovery in unconventional liquid reservoirs using CO2: a look ahead to the future of unconventional EOR. *SPE Unconventional Resources Conference*
120. Tran, T., Sinurat, P. D., and Wattenbarger, B. A., 2011. Production characteristics of the Bakken shale oil. *Society of Petroleum Engineers*. doi:10.2118/145684-MSTeklu, T. W., Li, X.,

Zhou, Z., and Abass, H., 2018. Experimental investigation on permeability and porosity hysteresis of tight formations. SPE Low Perm Symposium.
121. USGS, 2013. Petroleum resource assessment of the Bakken and Three Forks formation.
122. Valori, A., and Nicot, B., 2019. A review of 60 years of NMR wettability. Society of Petrophysicists and Well-Log Analysts.
123. Walsh, J., 1965. The effect of cracks on the compressibility of rocks, *Journal of Geophysical Research*, 70, 381–389.
124. Walton, I., and McLennan, J., 2013. The role of natural fractures in shale gas production. *ISRM International Conference for Effective and Sustainable Hydraulic Fracturing*
125. Wan T., 2015. Investigation of EOR performance in shale oil reservoirs by cyclic gas injection. *Doctoral dissertation*. Texas Tech University
126. Wang, F. P., and Gale, J. F. W., 2009. Screening criteria for shale-gas systems. *GCAGS Transactions*, 59, 779 – 793.
127. Wang, H., and Sharma, M. M., 2018. Estimating un-propped fracture conductivity and compliance from diagnostic fracture injection tests. *Society of Petroleum Engineers*. doi:10.2118/189844-MS
128. Wang, L., Tian, Y., Yu, X., Wang, C., Yao, B., Wang, S., Winterfeld, P. H., Wang, X., Yang, Z., Wang, Y., Cui J., and Wu, Y. S., 2017. Advances in improved/enhanced oil recovery technologies for tight and shale reservoirs. *Fuel* 210, 425-445
129. Wei, C., Wang, L., Li, B., Xiong, L., Liu, S., Zheng, J., Hu, S., and Song, H., 2018. A study of nonlinear elasticity effects on permeability of stress sensitive shale rocks using an improved coupled flow and geomechanics model: A case study of the Longmaxi shale in china. *energies* 11, 329
130. Whitman, W. G., 1923. The two-film theory of absorption. Chem. Metall. Eng., 29, pp. 147-152
131. Wicke, E., and Kallenbach R., 1941. Die oberflachendiffusion von kohlendioxyd in aktiven kohlen. *Kolloid Zeitshrift*, 97, 135.
132. Yasuda, K., Mori, Y. H., and Ohmura, R., 2016. Interfacial tension measurements in water-methane system at temperatures from 278.15 K to 298.15 K and pressures up to 10 MPa. *Fluid Phase Equilibria*, 413, 170-175
133. Yu, W., Zhang, Y., Varavei, A., Sepehrnoori, K., and Zhang, T., 2018. Compositional simulation of CO_2 huff-n-puff in Eagle Ford tight oil reservoirs with CO_2 molecular diffusion, nanopore confinement and complex natural fractures. *SPE IOR Conference*
134. Zhang, M., and Ayala, L. F., 2015. Constant GOR as an Infinite Acting Effect in Reservoirs Producing Below (Dew/Bubble) Saturation Pressure. *Society of Petroleum Engineers*. doi:10.2118/175079-MS
135. Zhu, Z., Xu, Y., and Jiang, B., 2012. A one ppm NDIR methane gas sensor with single frequency filter denoising algorithm. *Sensor*, 12, 12729-12740
136. Wash, J.B., 1981, Effect of pore pressure and confining pressure on fracture permeability: International Journal of Rock Mechanics and Mining Sciences, v. 18, p. 429-435.

Appendix A

To quantitatively explain the importance of processes or parameters that I propose to study, some reasonable reservoir descriptions are presented as below, including the results of laboratory measurements, field studies, and literature reviews for Eagle Ford formation.

i. Rock properties:

- Porosity: 5%
- Matrix tortuosity: from 2-10
- Matrix permeability: nanodarcy scale
- Pore size distribution: 20 – 75nm
- Formation thickness: 100ft
- Reservoir containment factor: 0.75 (25% injected gases loss)

ii. Reservoir fluid and PVT:

- Oil compressibility: $5.5* 10^{-6}$ psi^{-1}
- Produced fluid composition: C_1-C_{17}
- Reservoir temperature: 130^oC
- Primary fracture/proppant pack pressure after primary depletion: 2000 psi
- Reservoir pressure during gas injection: 8000 psi

iii. Injection gas:

- Composition: 100% Methane- C_1
- Standard condition: 25^oC – 15psi
- Surface injection rate: 3MMscf/day
- 1^{st} cycle injection time: 6months

- Oil-methane diffusion coefficient (dodecane-methane): $2*10^{-8}$ m^2/s (Jamialahmadi et al., 2006)
- Oil swelling factor: adjusted by oil-gas diffusion coefficients with initial gas molar concentration

iv. Completion design:

- Frac-stage: 15-25
- Stage spacing: 200-300ft
- Lateral length: 3000 – 5000ft
- Average hydraulic fracture spacing: 2-4ft
- HF spacing distribution (Raterman et al., 2017)
- Secondary fracture zone (away from primary fracture): 10ft (Zhang et al., 2010)
- Fracture half-length / fracture height: 2-3
- Proppant mass/ stage: 400,000lbs
- Proppant pack porosity (after 10 days): 16-30 p.u (Mittal et al., 2017)
- Proppant pack permeability: millidarcy scale

Appendix B

Relative contribution of molecular diffusion, Knudsen flow, and Poiseuille flow in straight cylindrical pore. At nano-pore scale, viscous flow become less important than molecular diffusion in mass transfer. (Karger et al., 2012)

p (atm)	D_m ($cm^2 s^{-1}$)	r (cm)	D_K ($cm^2 s^{-1}$)	D ($cm^2 s^{-1}$)[a)]	D_{vis} ($cm^2 s^{-1}$)	D_{total} ($cm^2 s^{-1}$)	$\frac{D_{vis}}{D_{total}}$
		10^{-6}	0.03	0.027	0.0007	0.027	0.026
1.0	0.2	10^{-5}	0.3	0.121	0.07	0.19	0.37
		10^{-4}	3.0	0.19	7.0	7.2	0.97
		10^{-6}	0.03	0.012	0.007	0.019	0.37
10	0.02	10^{-5}	0.3	0.019	0.7	0.719	0.97
		10^{-4}	3.0	0.020	70	70	1.0

Appendix C

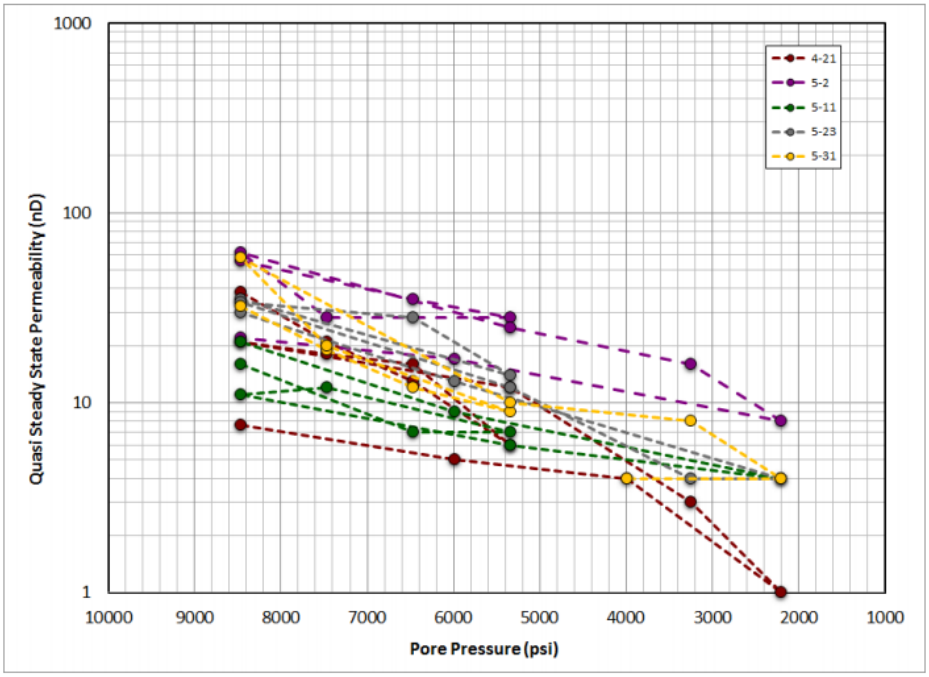

Summary of permeability measurements as a function of the pore pressure for EF-1 sample. The sample is highly stress sensitive, but with moderate hysteresis. Note the confinement stress was 11950 psi. (Data were provided by ENCANA)